

Velocity Distribution Functions of Heavy Ions in the Solar Wind at 1 AU

Dissertation
zur Erlangung des Doktorgrades
der Mathematisch-Naturwissenschaftlichen-Fakultät
der Christian-Albrechts-Universität
zu Kiel

vorgelegt von
Dipl.-Phys. Lars Berger

Kiel im Oktober 2008

Referent/in : _____

Korreferent/in : _____

Tag der mündlichen Prüfung : _____

Zum Druck genehmigt : _____

Der Dekan

Zusammenfassung

Das Studium der Geschwindigkeitsverteilungen von Sonnenwind Ionen erlaubt es auf die Entstehung und Entwicklung des Sonnenwindes zurück zu schließen. Es ist somit möglich durch in situ Beobachtungen die physikalischen Prozesse in der solaren Korona und der inneren Heliosphäre zu studieren. Die schweren Ionen im Sonnenwind die aufgrund ihrer geringen Häufigkeiten schwer zu messen sind wurden hierbei lange Zeit vernachlässigt. Bislang gibt es nur eindimensionale Beobachtungen von ihren Geschwindigkeitsverteilungen.

Im Rahmen dieser Arbeit wurden die dreidimensionalen Geschwindigkeitsverteilungen von schweren Ionen im Sonnenwind untersucht. Die Untersuchungen wurden mit Daten vom Solar Wind Ion Composition Spectrometer auf dem Advanced Composition Explorer durchgeführt. Ein neues verbessertes Verfahren zur Datenanalyse wurde entwickelt. Das Verfahren ist besonders geeignet für die Analyse kleiner Zählraten und erlaubt es somit hohe Zeitauflösungen zu verwenden. Anhand der bekannten dreidimensionalen Geschwindigkeitsverteilungen von Protonen und Alphateilchen wurde ein Modell für die dreidimensionalen Verteilungen von schweren Ionen entwickelt. Zudem wurde ein virtueller Detektor implementiert der es erlaubt die 1D Beobachtungen mit dem 3D Modell zu vergleichen. Unsere Untersuchungen haben gezeigt, daß mit Hilfe des Modells Eigenschaften der Verteilungen die mit der Annahme einer thermischen Verteilung im Widerspruch stehen reproduziert werden können. Darüber hinaus wurde der Einfluss von Welle-Teilchen Wechselwirkung auf die beobachteten Temperaturen der Ionen untersucht.

Abstract

From the study of the velocity distributions of solar wind ions we can draw conclusions about the formation and the development of the solar wind. Thus, it is possible to study the physical processes in the solar corona and the inner heliosphere by *in situ* measurements. Because their low abundance complicates their measurements heavy solar wind ions have been long neglected. Up to now observations of their velocity distributions have been solely 1D.

In this thesis the 3D velocity distributions of heavy solar wind ions have been investigated. For our studies we have used data from the Solar Wind Ion Composition Spectrometer on-board the Advanced Composition Explorer. A new improved analysis technique has been developed. The new technique is adapted to analyse small count rates and thus, allows the use of high time resolutions. Based on the known 3D velocity distributions of protons and alpha particles a model for the 3D distributions of heavy ions has been developed. Furthermore, a virtual detector was implemented, that allows a comparison of the 1D observations and the 3D model. From our investigations we found that the model is capable to explain non-thermal features of the observations. In addition the influence of wave-particle interaction on the observed ion temperatures have been analysed.

Contents

1	Introduction	1
2	ACE	4
2.1	The ACE mission	4
2.2	Instrumentation	4
3	SWICS	6
3.1	Principle of operation	6
3.2	Instrumental Response Functions / Efficiency Model	8
3.3	Data Analysis	13
3.3.1	Box-rates	13
3.3.2	Spill-rates	14
3.3.3	Probabilistic Rates	16
3.4	Solar wind properties	17
4	Maximum Likelihood Analysis technique	22
4.1	Disadvantages of the standard analysis technique	22
4.2	Improved Analysis technique	23
4.3	Maximum Likelihood Fitting	26
4.4	Advanced Probabilistic Rates	27
4.5	Comparison with others	28
4.6	Data Products	36
5	Velocity Distribution Functions	38
5.1	3D Velocity Distribution Functions	38
5.2	Virtual Detector	44
6	Differential Streaming and Temperature	51
6.1	Interpretation of Observations	51

6.2	Data	55
6.3	Comparison of Virtual and Measured Spectra	56
6.4	Observed Differential Streaming	58
6.5	Statistical Analysis of Differential Streaming and Temperature	63
6.6	Wave particle interaction / Turbulent heating	66
7	Summary and Conclusions	72
7.1	Outlook	73

1 Introduction

Though the Sun is far from being a peculiar star according to the theory of stellar evolution, it naturally holds an outstanding rank among all other stars. No other star is as accessible for detailed studies as the Sun. For instance, high-resolution remote-sensing images of the solar corona have revolutionized our understanding of the solar and stellar flares, long-term measurements of solar oscillations have allowed us to understand the interior structure of the Sun to high accuracy. The Sun is also the only star of which we can obtain nearly pristine samples of its atmosphere. The extension of the corona into the heliosphere - the solar wind - is the only stellar wind that can be studied *in situ*. Obviously, the same holds true for the entire structure of the heliosphere, it is the only accessible astrosphere.

Almost all information we can obtain about other stars is carried by the electromagnetic radiation that reaches us here at Earth. But there is another kind of radiation that is emitted by stars that can be observed only by *in situ* measurements. It is a particle radiation that is constantly streaming away from the Sun, due to its solar origin it is called the solar wind. Beside the solar wind there are different particle populations that for the greater part have their origin in the heliosphere. Figure 1 illustrates the large scales of intensity, and energy respectively that are covered by the different populations. From the large range of energies the question for the acceleration processes they have undergone arises. Since the beginning of space flight rapid proceedings in theory have been made by the increasing quality and quantity of observation. The properties of the solar wind have been investigated to a high degree and surprising results like the formation of shocks at discontinuities in the plasma that can accelerate particles very efficiently, have been found. In spite of all progress, there is up to now no closed theory that can explain the development of the solar wind in the solar corona. Recent theories indicate that this topic is closely bound to the question of coronal heating and thus to the theory of stellar atmospheres altogether. The most promising candidate among the discussed acceleration processes is wave-particle interaction. An extensive overview of this topic is given in *Hollweg* [2006].

1 Introduction

Though we said that the solar wind has been intensively investigated, this mainly holds true for protons and alpha particles that make up the major part. All other ions that altogether make up only a few percent of the solar wind were long neglected, also because their low abundance complicates their measurement.

In this thesis, we investigate the kinetic properties of heavy solar wind ions at 1 Astronomical Unit (AU) under quiet time conditions. The properties of the emerging solar wind can help us figure out the importance of wave particle interaction in respect to Coulomb collisions. Because the solar wind may well be a source population for observed suprathermal particles (s. Quiet Time Background in figure 1) the knowledge of its kinetic properties is also a prerequisite for the investigation of suprathermal particles and the corresponding acceleration processes.

In the following the structure of this thesis is briefly outlined. For our studies we use mainly data from the Solar Wind Ion Composition Spectrometer that is on-board the Advanced Composition Explorer. The scientific aims of the mission and the on-board instrumentation of the Advanced Composition Explorer are briefly described in chapter 2. Because the understanding of the instrumental properties is critical for the understanding of how the data from the Solar Wind Ion Composition Spectrometer has to be analysed the principle of operation and state of the art data analysis are described in chapter 3. Due to some disadvantages of the existing analysis technique when dealing with low count rates, we have developed a new analysis technique that is adapted to low count-rate situations. In chapter 4 our new technique is described, both methods are compared and some data products from the new technique are presented. The observed velocity distributions are 1D projections of the underlying 3D distributions. Because we are interested in the kinetic state of the heavy ions, we have designed a model for the 3D distributions and a virtual detector that simulates the behaviour of the real instrument. Taking both together virtual spectra can be calculated and compared with observation. The model and the detector are presented in chapter 5. From the virtual spectra predictions for several features of the observations can be made. We used the observed differential streaming of heavy ions with respect to protons together with the observed temperatures to demonstrate the significance of the model. Additionally the effect of wave-particle interaction is investigated. These studies are presented in chapter 6. Finally our results are discussed and an outlook for further studies is given in chapter 7.

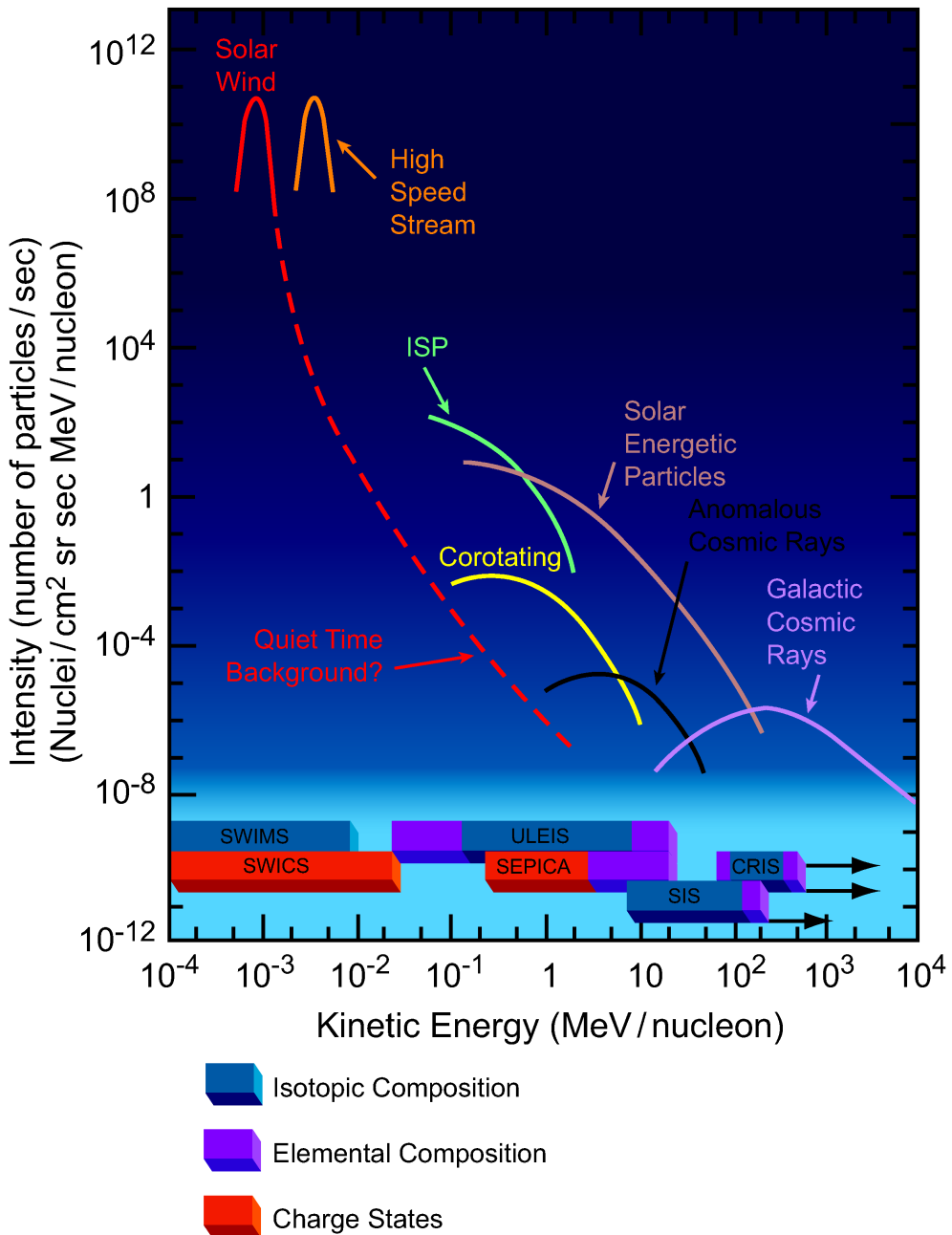


Figure 1.1: A schematic view of the spectra of energetic oxygen nuclei is shown. The energy ranges and the capabilities of the different instruments on-board ACE can be seen at the bottom of the plot. From www.srl.caltech.edu/ACE/ASC/DATA/ACEbrochure/ACEbrochure-2nd-ed8.pdf

2 ACE

2.1 The ACE mission

The Advanced Composition Explorer (ACE) is a NASA mission that was launched August 1997. The spacecraft is orbiting L1 where measurements are undisturbed by Earth's magnetosphere. The scientific goals addressed by ACE are

1. The elemental and isotopic composition of matter
2. Origin of the elements and subsequent evolutionary processing
3. Formation of the solar corona and acceleration of the solar wind
4. Particle acceleration and transport in nature

Originally designed for at least two years, the duration of the mission has been extended several times. At this time, the end of the mission will be determined by the amount of propulsion which will last until about 2022. Thus, we have the unique opportunity to cover more than two solar cycles with the same set of instruments. A detailed overview of the mission is given in *Stone et al.* [1998a].

2.2 Instrumentation

The instruments on-board are

1. The Cosmic Ray Isotope Spectrometer (CRIS, *Klarmann et al.* [1995])
2. The Solar Isotope Spectrometer (SIS, *Stone et al.* [1998b])
3. The Ultra Low Energy Isotope Spectrometer (ULEIS, *Mason et al.* [1998])
4. The Solar Energetic Particle Ionic Charge Analyser (SEPICA, *Möbius et al.* [1998])
5. The Solar Wind Mass Spectrometer (SWIMS, *Gloeckler et al.* [1998])
6. The Solar Wind Ion Composition Spectrometer (SWICS, *Gloeckler et al.* [1998])

2.2 Instrumentation

7. The Electron, Proton and Alpha Monitor (EPAM, *Gold et al.* [1998])
8. The Solar Wind Electron Proton Alpha Monitor (SWEPAM, *McComas et al.* [1998])
9. The Magnetometer (MAG, *Smith et al.* [1998])

3 SWICS

The Solar Wind Ion Composition Spectrometer (SWICS) is a linear time-of-flight mass spectrometer with electrostatic deflection. The model that is mounted on ACE is the slightly modified flight spare of the Ulysses SWICS instrument that was launched in 1990. As the name implies SWICS was designed to measure the composition of the solar wind. It can measure mass, charge, and energy of ions. In principle all ion species from H through Fe with typical charge states are covered. The energies range from $< 1\text{keV}$ up to about 1MeV depending on the individual ions. In section 3.1, a brief overview of the principle of operation is given. A detailed description of the instrument can be found in *Gloeckler et al.* [1998]. State-of-the-art data analysis is described in section 3.3. Finally the path from instrumental count rates to physical values is outlined in section 3.4.

3.1 Principle of operation

SWICS measures the mass, m_{ion} , charge, q_{ion} , and energy, ϵ_{ion} , of entering ions using a combination of electrostatic deflection, a linear Time of Flight (ToF), and an energy measurement. The schematic trajectories of particles through the instrument and the measurements are shown in figure 3.1. After the particle has passed the collimator it enters the electrostatic analyser. It can only pass if its initial kinetic energy per charge equals the selected E/q value. The analyser is stepped through 60 logarithmical steps from $\approx 100\text{kV}$ down to $\approx 0.5\text{kV}$ every 12 minutes. Afterwards the ion is accelerated by a potential drop of $\approx -24\text{kV}$. Then it penetrates through a thin $\approx 11\text{nm}$ carbon foil, where secondary electrons are emitted. The electrons trigger the start signal of the ToF measurement. Behind the foil, the particle drifts more or less force free, and finally hits a Solid State Detector (SSD). Again secondary electrons are emitted, this time triggering the stop signal of the ToF measurement. The SSD measures the total energy. Thus, for each particle we have three measurements,

1. Energy per Charge

3.1 Principle of operation

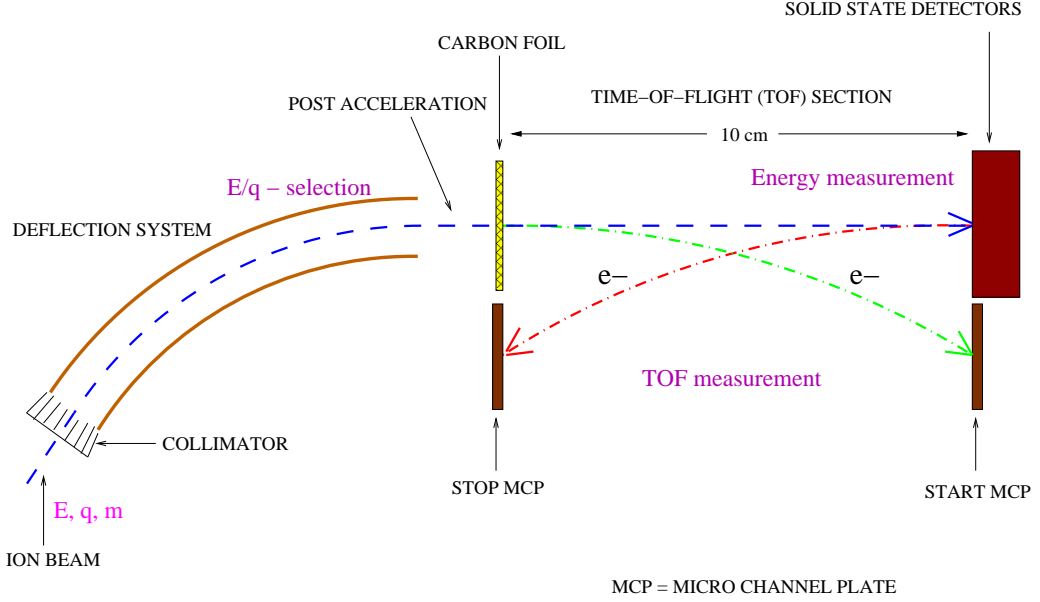


Figure 3.1: Schematic view of SWICS.

$$\frac{E}{q} \in [100, \dots, 0.5] \text{ kV} \quad (3.1)$$

2. Time of Flight given by

$$\tau = \frac{d}{\sqrt{2(V_a + E/q) q_{ion}/m_{ion}}} \quad (3.2)$$

3. Total Energy given by

$$\epsilon = q_{ion} (V_a + E/q) \quad (3.3)$$

With the post acceleration voltage, V_a , and the length of the time of flight section, d , in which the particle drifts force free, we can identify the ion species and derive its initial kinetic energy ϵ_{ion} .

1.

$$q_{ion} = \frac{\epsilon}{V_a + \frac{E}{q}} \quad (3.4)$$

2.

$$m_{ion} = \frac{2\epsilon\tau^2}{d^2} \quad (3.5)$$

3 SWICS

3.

$$\epsilon_{ion} = \frac{E}{q} q_{ion} \quad (3.6)$$

Equation 3.6 can be understood as a filter for the particles initial velocity, given by

$$v_{0_{ion}} = \sqrt{2 \frac{E}{q} \frac{q_{ion}}{m_{ion}}}. \quad (3.7)$$

So, as the deflection voltage is stepped through we would obtain the velocity distribution of the measured ions. From these distributions, physical values like absolute density and flux, temperature, solar wind speed and suprathermal flux can be derived.

3.2 Instrumental Response Functions / Efficiency Model

For any kind of data analysis it is essential to know how the instrument responds to entering particles. Let us first consider the “ideal” instrument. The most detailed data delivered by SWICS are the Pulse Height Analysis (PHA) data. For each deflection step we get a set of PHA words each consisting of an energy- and a ToF-channel (E_{CH}, t_{CH}) which are translated back to ϵ and τ via

$$\epsilon = E_{CH} \frac{610.78}{255}, [\text{keV}] \quad (3.8)$$

$$\tau = T_{ch} \frac{200}{1023}, [\text{ns}] \quad (3.9)$$

with some information loss due to discretisation. If we take equations 3.8,3.9 together with 3.4 and 3.5 we get

$$E_{CH} = \left[\frac{q_{ion}}{\alpha} \right], \text{ with } \alpha = \frac{610.78}{255} \frac{1}{(V_a + E/q)} \quad (3.10)$$

and

$$T_{CH} = \left[\sqrt{\frac{m_{ion}}{q_{ion}}} \beta \right], \text{ with } \beta = \frac{1023}{200} \frac{d}{\sqrt{2(V_a + E/q)}}, \quad (3.11)$$

where $\left[\right]$ denotes Gaussian brackets. This tells us that, for a given E/q -step, counts of different ion species (m_{ion}, q_{ion}) would sum up at different places in the plane spanned by energy and ToF (E_{CH}, T_{CH}). To get the count rate for any one ion, one only has to sum up the counts at the positions following from equations 3.10 and 3.11.

Unfortunately, life is not so simple. In the “real” instrument there are several effects that

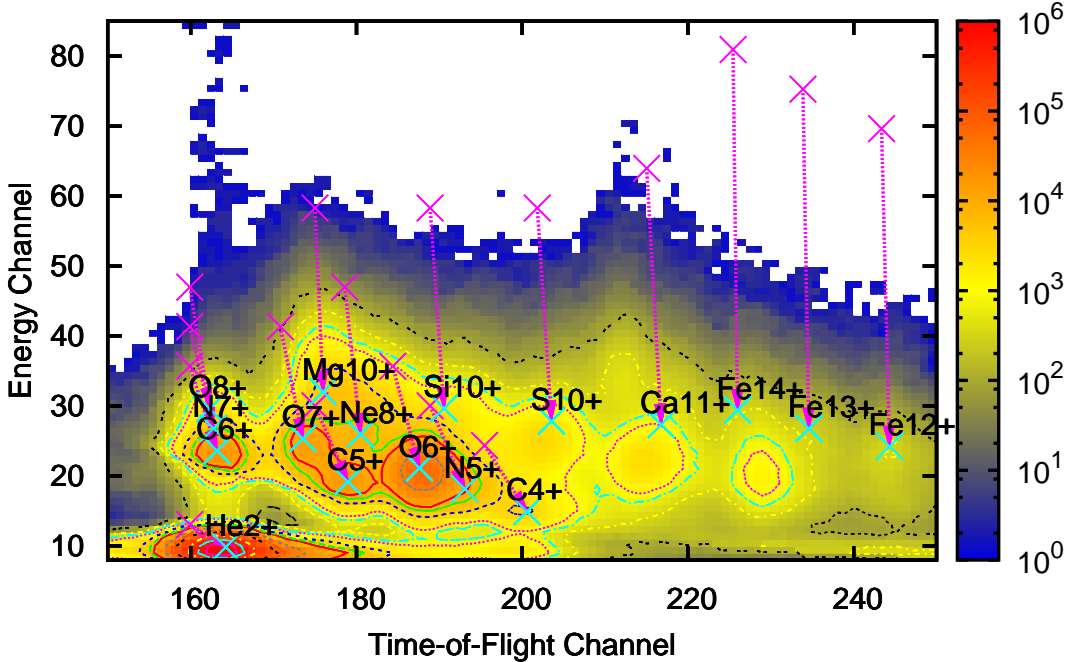


Figure 3.2: Example of long-term data of E/q -step 40. The magenta crosses mark the positions for several ion species one would get from equations 3.10 and 3.11. The positions marked by the light blue crosses shows what we get from our analysis. Count rates are colour-coded the ISO-contour lines are logarithmically spaced ($10^2, 3.3 \cdot 10^2, 6.6 \cdot 10^2, 10^3 \dots 10^6$).

tend to move and blur the positions, an example is given in figure 3.2. The most important effects for this work are the uncertainty of the electrostatic analyser, the energy loss and the scatter in the carbon foil and the pulse height defect of the Solid State Detector (SSD), their influence is listed in table 3.1.

To determine the Instrumental Response Functions (IRFs) of ACE/SWICS we have analysed into long-term flight data. We found that the Analogue Digital Converters (ADCs) for ToF and energy have a non linearity, an example is given in figure 3.3. To get rid of this effect we decided to do a two to one binning in both energy and ToF. Channel zero, containing the double coincidences¹, was left unchanged. The calibration for the binned data is

$$E_{CHb} = \epsilon \frac{127.5}{610.78} + 0.25 \quad (3.12)$$

¹double coincidence means start and stop signal for ToF but no energy measurement has been triggered

effect	shift ToF pos	shift E pos	blur ToF pos	blur E pos
$\frac{\Delta E/q}{E/q} = \pm 3\%$	-	-	+	+
Carbon foil	+	+	+	+
Pulse height defect	-	+	-	+

Table 3.1: As an example three quantities that influence the IRFs, together with the kind of their influence, are listed

$$T_{CHb} = \tau \frac{511.5}{200} + 0.25 \quad (3.13)$$

for the energy and ToF calibration. Figure 3.4 shows an example of the binned data. Using a combination of a Levenberg Marquardt fit and an advanced Efficiency Model (EM) that is used as a Forward Model (FM) and that has been developed by *Köten* [2008], the IRFs have been determined, for the binned data. For the shape of the peaks a two-dimensional asymmetric Gaussian has been used

$$G(\tau, \epsilon) = Ae^{-\frac{(\tau - \tau_0)^2}{2(\sigma_{\pm}^{\tau})^2} - \frac{(\epsilon - \epsilon_0)^2}{2(\sigma_{\pm}^{\epsilon})^2}}. \quad (3.14)$$

With the peak-position, (τ_0, ϵ_0) , the four widths, $\sigma_{+}^{\tau}, \sigma_{-}^{\tau}, \sigma_{+}^{\epsilon}, \sigma_{-}^{\epsilon}$, and the peak height, A , we have seven free parameters per ion. The indices $+, -$ of the sigmas denote that either is used depending on the sign of $\tau - \tau_0$, and $\epsilon - \epsilon_0$ respectively. Since most of the distributions overlap with neighbouring ones, as many ions as possible have to be fitted simultaneously. Fitting with such a big number of free parameters is extremely sensitive to the goodness of the starting values. Iterative starting values for the peak positions have been calculated using the EM, then the fitting was done. The results were used to correct the parameters of the EM. In a final step the adjusted EM was used to calculate the positions and a last fit to determine the widths was carried out. For several ions with small total overlap the results were satisfying and showed slight asymmetries. On the one hand, the asymmetries displayed no significant trend, on the other hand the mean widths in ToF and energy were proportional to τ_0 and ϵ_0 respectively, given by

$$\sigma^{\tau} = \max(\tau_0 \cdot .02, 1.5) \quad (3.15)$$

$$\sigma^{\epsilon} = \max(\epsilon_0 \cdot .10, 1.5). \quad (3.16)$$

In order to treat every ion the same way, the asymmetric Gaussians were discarded and symmetric Gaussians with $\sigma_{+}^{\tau} = \sigma_{-}^{\tau}$, and $\sigma_{+}^{\epsilon} = \sigma_{-}^{\epsilon}$ were used from now on. The widths for

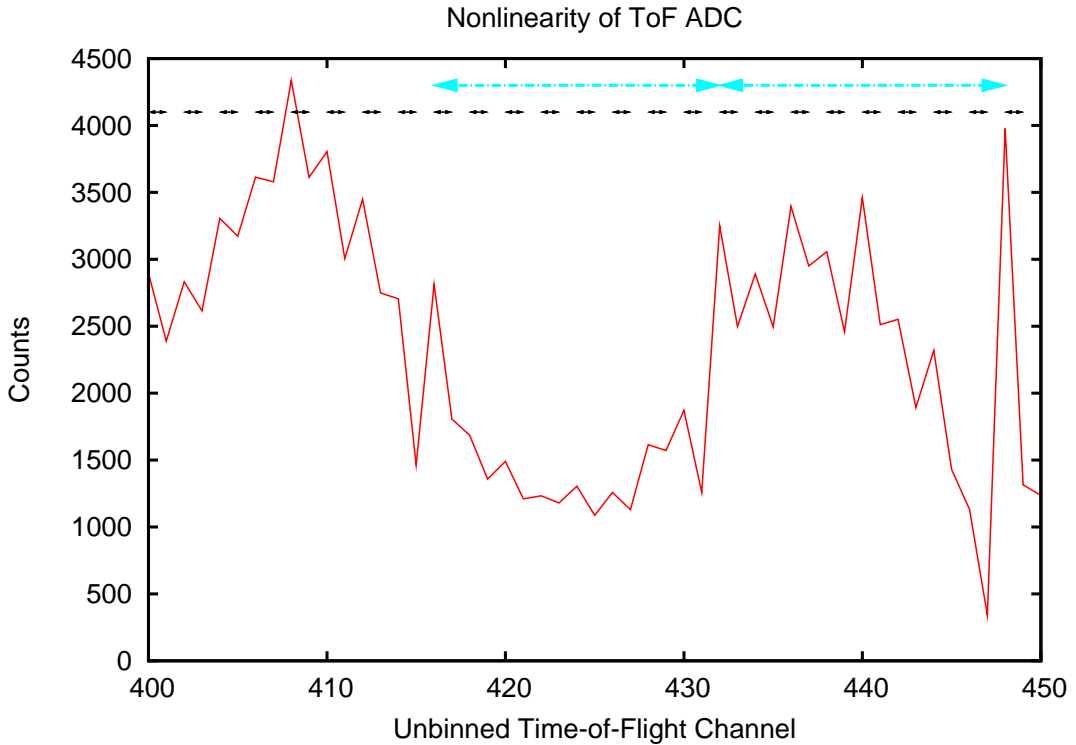


Figure 3.3: A cut through an unbinned long-term data E-T matrix along the ToF axis is shown. The peaks belonging to different ion species can easily be seen. But obviously there is a pattern coming from a nonlinearity of the ADC. The pattern caused by the lowest bit is marked by the small black arrows. It seems that there are patterns caused by higher bits. The dashed light blue arrows indicate a possible pattern caused by the 5th bit (16 channels).

all ions were calculated using equations 3.15 and 3.16. Together with the positions from the EM, we now have a tool to calculate the IRF for any one ion (including isotopes as well) as shown in figure 3.5. Because the positions for different elements lie on hyperbolas in the E-T plane (s. figure 3.6), even the high E/q steps, which are of special interest in the search for suprathermal particles, are covered. To check for instrumental drifts we used this procedure for summed data of the years 2001, 2002, 2003, and 2004 and found no significant differences. In addition, the influence of the aspect angle, which is the angle between the spacecraft's spin axis and the line earth-sun has been analysed. Other than with Ulysses/SWICS, where the aspect angle oscillates much stronger than is the case with ACE/SWICS, no significant aspect angle dependency of the IRFs has been found. If we compare our results with the predictions of a FM by Simon Hefti (s. Figure 3.7) we find our model to be much more realistic. Especially the heavy elements seem to be

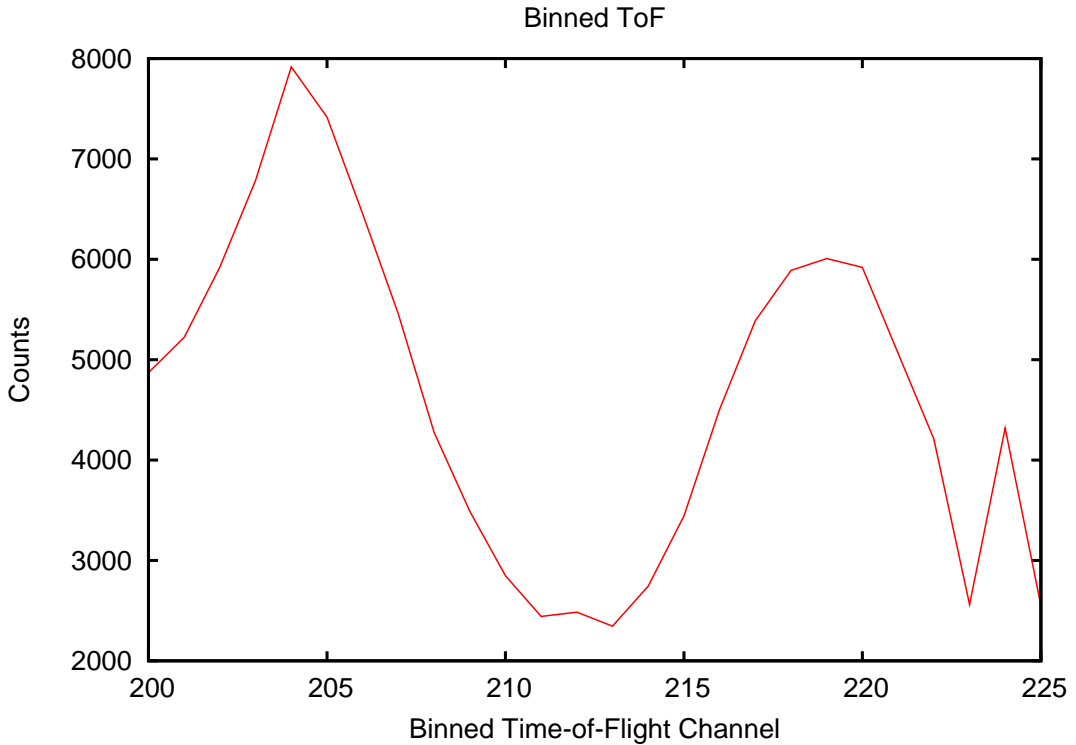


Figure 3.4: The same cut as in the previous figure is shown, but this time the data has been binned, according to the black arrows. The pattern caused by the nonlinearity is gone.

strongly improved. The ToF position depends on the velocity, while for a certain velocity the energy is proportional to the nuclear mass. The pulse height defect, $\eta_{SSD}(E(m), m, q)$, of the SSD depends on energy, nuclear mass and charge. Therefore, all ions of an element must lie on a smooth curve, as is the case in both models. But in our model the sequences do not intersect and their spacing depends on m and q . In the Hefti model, the sequences show some strange and irregular behaviour. Between carbon and nitrogen there is a large gap, while nitrogen and oxygen are hardly separated from each other. Silicon and sulfur are separated by a large gap while the spacing between sulfur and iron is extremely small compared to their difference in mass and charge. There is hardly any space for all elements in between, compare the calcium sequence from our model. Finally, the strangest behaviour is shown by magnesium, starting at high energies close to oxygen, intersecting neon and silicon to lower energies.

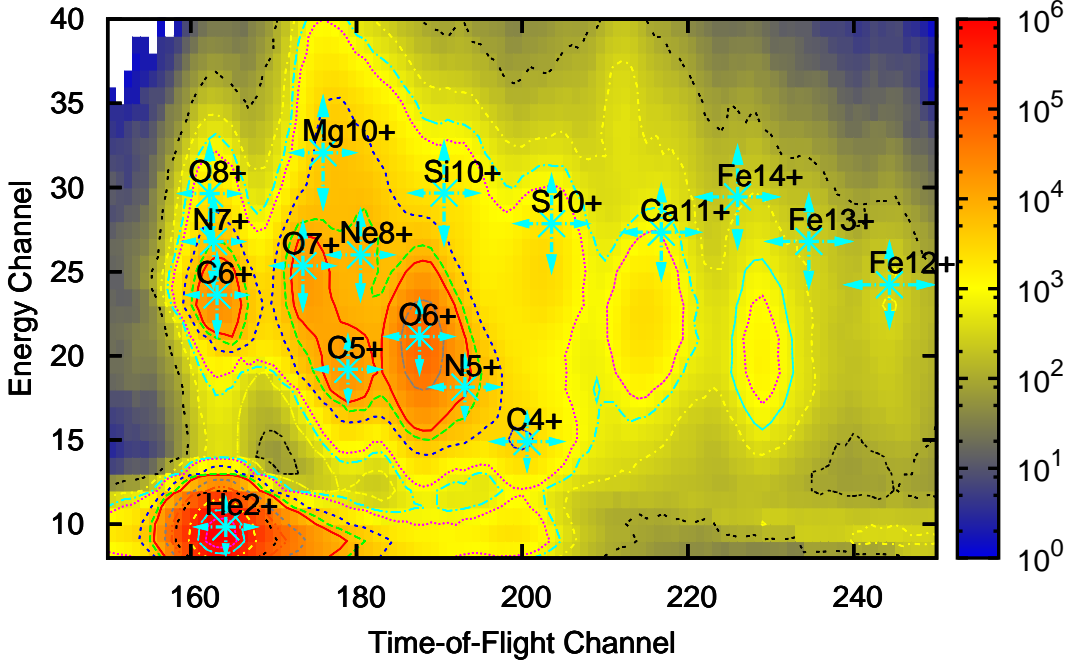


Figure 3.5: An example of long-term data for E/q -step 40 together with the peak position (light blue crosses) and the σs (light blue arrows) of some IRFs is shown. Count rates are colour-coded the ISO-contour lines are logarithmically spaced ($10^2, 3.3 \cdot 10^2, 6.6 \cdot 10^2, 10^3 \dots 10^6$).

3.3 Data Analysis

von Steiger et al. [2000] developed an analysis technique for Ulysses/SWICS. Because of the strong similarities between the two instruments it is also used for ACE/SWICS by the group of T. Zurbuchen in Michigan. In this section the main ideas of this technique are described in some detail to point out the differences between it and our new improved maximum-likelihood technique which is described in chapter 4.

3.3.1 Box-rates

Assuming that the IRFs are well known, we can put boxes around the peak positions in the E-T matrices and sum up all counts that lie inside. If the IRFs were disjoint, data analysis would be already done. Figure 3.8 shows long-term data of E/q step 7. Both helium peaks are isolated so that a box-rate would be fully sufficient for data analysis. But as demonstrated as an example for O^{6+} and N^{5+} , for the majority of ions, the box-rates cannot be taken as count rates without further processing.

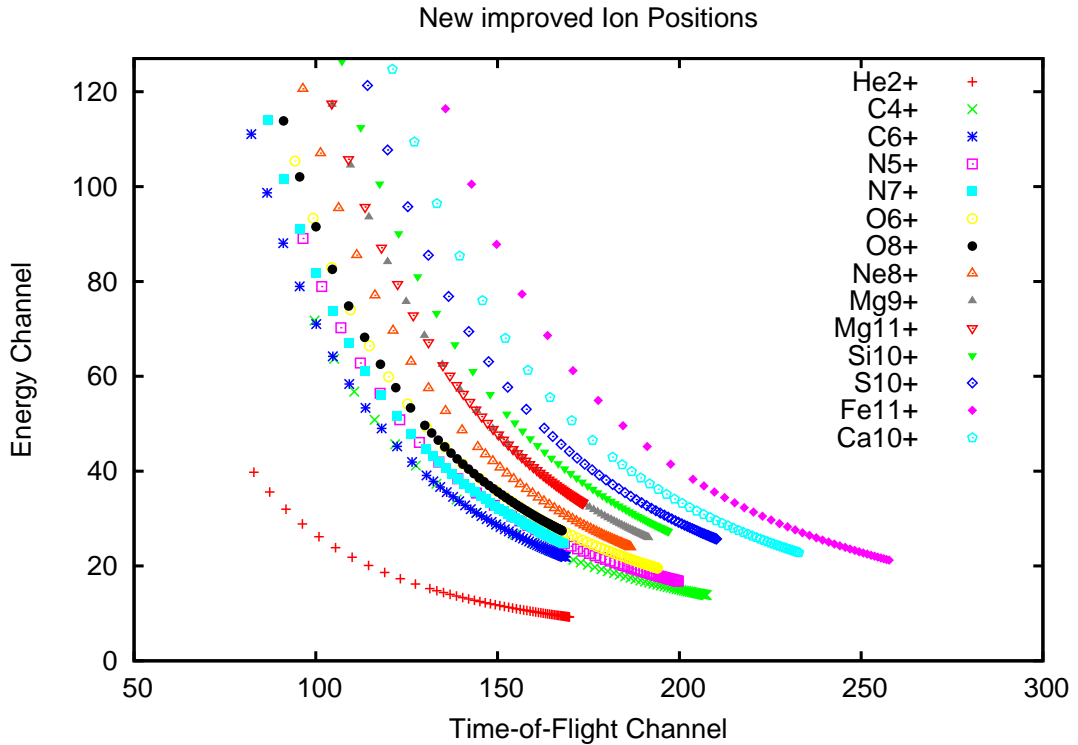


Figure 3.6: The ion positions from the FM by *Kötén* [2008] are shown. For every ion, the positions of all E/q steps are plotted. The elements lie on hyperbolas that are well separated from each other.

3.3.2 Spill-rates

As shown in chapter 3.2 the IRFs in most cases have strong overlap with neighbouring ions and the IRFs for the i th ion in the s th E/q step has the form of a two dimensional Gaussian, given by

$$G_{si}(\tau, \epsilon) = \frac{1}{2\pi\sqrt{\sigma_{si}^{\tau}\sigma_{si}^{\epsilon}}} e^{-\frac{(\tau - \tau_{si}^0)^2}{2(\sigma_{si}^{\tau})^2} - \frac{(\epsilon - \epsilon_{si}^0)^2}{2(\sigma_{si}^{\epsilon})^2}} \quad (3.17)$$

In this case, the box-rates (\vec{B}) are polluted by counts of surrounding ions. If the box around ion i has the widths $\sigma_{si}^{\tau}, \sigma_{si}^{\epsilon}$ (see dotted magenta boxes in fig. 3.8), the spillover of ion j to box i is

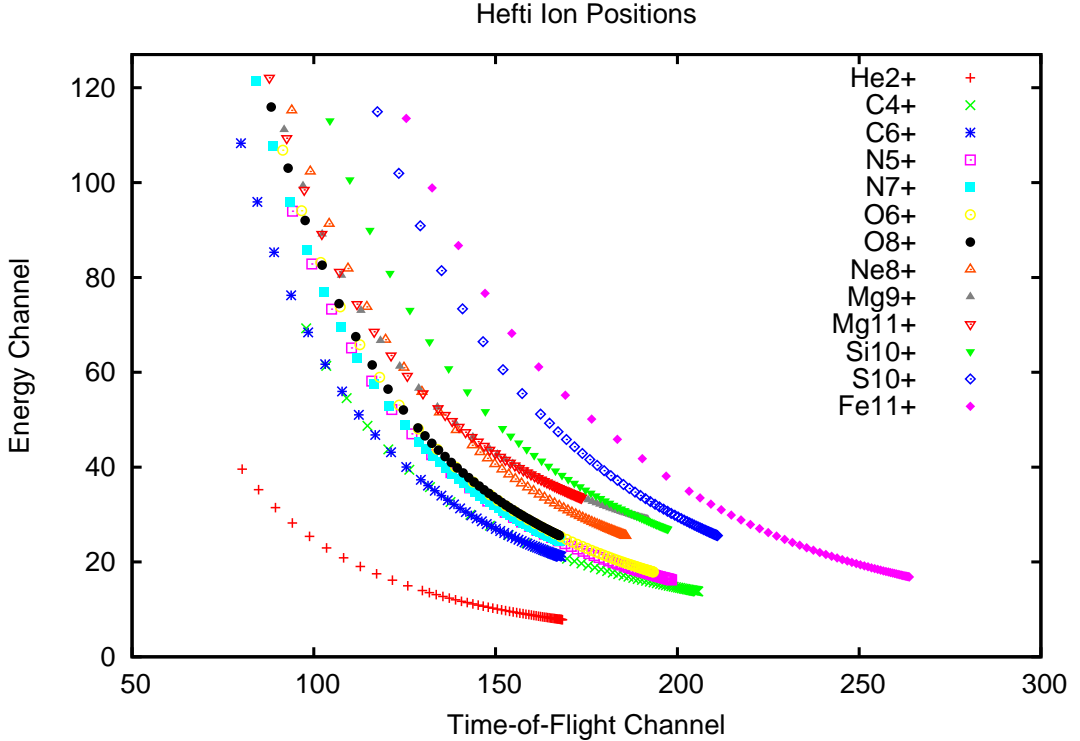


Figure 3.7: The ion positions from the FM by Hefti are shown. As in Figure 3.6 all E/q steps are plotted. The separation of the elemental sequences is not as clear as from the Köten model. E.g. the Nitrogen sequence nearly falls on top of the Oxygen sequence, separated by a large gap from the Carbon sequence.

$$\begin{aligned}
 S_{sij} &= \int_{\tau_0^{si}-\sigma_\tau^{si}}^{\tau_0^{si}+\sigma_\tau^{si}} \int_{\epsilon_0^{si}-\sigma_\epsilon^{si}}^{\epsilon_0^{si}+\sigma_\epsilon^{si}} G_{sj} d\epsilon d\tau \\
 &= \frac{1}{4} \operatorname{erf} \left(\frac{\tau_0^{si} + \sigma_\tau^{si} - \tau_0^{sj}}{\sqrt{2}\sigma_\tau^{sj}}, \frac{\tau_0^{si} - \sigma_\tau^{si} - \tau_0^{sj}}{\sqrt{2}\sigma_\tau^{sj}} \right) \operatorname{erf} \left(\frac{\epsilon_0^{si} + \sigma_\epsilon^{si} - \epsilon_0^{sj}}{\sqrt{2}\sigma_\epsilon^{sj}}, \frac{\tau_0^{si} - \sigma_\tau^{si} - \tau_0^{sj}}{\sqrt{2}\sigma_\tau^{sj}} \right),
 \end{aligned} \tag{3.18}$$

with

$$\operatorname{erf}(x, y) = \operatorname{erf}(x) - \operatorname{erf}(y). \tag{3.19}$$

The spillover can be written as a matrix \hat{S} , which is essentially

$$\vec{B} = \hat{S} \times \vec{N} \tag{3.20}$$

where \vec{N} is the vector of the true ion rates which we obtain by inverting \hat{S}

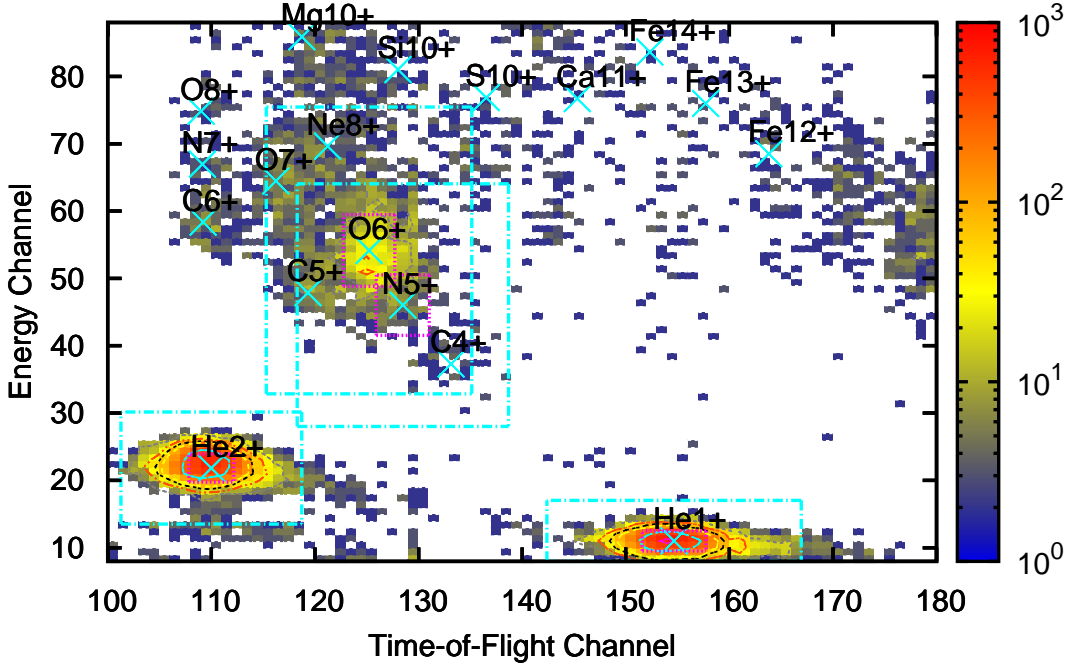


Figure 3.8: Long-term data of E/q step 7 is plotted. Count rates are colour-coded. ISO-contour lines are spaced as in Fig. 3.2, starting with 10^1 . The positions of several ions are marked (light blue crosses). 1 sigma boxes (dotted magenta lines) and 4 sigma boxes (dash dotted light blue lines) of He^{2+} , He^{1+} , O^{6+} and N^{5+} are shown

$$\vec{N} = \hat{S}^{-1} \times \vec{B}. \quad (3.21)$$

The inversion of \hat{S} is done by Singular Value Decomposition (*Press et al. [1992]*). Unfortunately \vec{N} is not positive definite. Negative counts are not a physical solution, so these ions have to be removed from \vec{B} and \hat{S} , and equation 3.21 has to be applied again until \vec{N} is positive definite.

3.3.3 Probabilistic Rates

To include the counts outside the boxes, the so called probabilistic rates are introduced. With the spill-rates, N_{spill}^{si} , as a good guess, the IRFs according to equation 3.17 can be used to calculate the actual ion distributions, $D_{si}(\tau, \epsilon)$,

$$D_{si}(\tau, \epsilon) = N_{spill}^{si} G_{si}(\tau, \epsilon). \quad (3.22)$$

With these distributions we can derive the probabilities

$$P_{si}(\tau, \epsilon) = \frac{D_{si}(\tau, \epsilon)}{\sum_{j=1}^{n_{ion}} D_{sj}(\tau, \epsilon)} \quad (3.23)$$

that a given event belongs to ion species i . Finally a dice roll for each event decides to which species it belongs resulting in the probabilistic rates \vec{N}_{prob}^s . The advantage over the spill-rates is that all counts are taken into account and in addition they incorporate the shape of the IRFs properly.

3.4 Solar wind properties

From data analysis we know the count rates of each ion species i that have been measured in E/q step s . But several assumptions and considerations are needed to transform these rates into the physical values that describe the kinetic state of the solar wind plasma, namely the distribution in phase space $\rho_i(x, y, z, v_x, v_y, v_z)$. In the following, the path from count rates to physical quantities is outlined.

First we have to consider what SWICS actually measures. The basic assumption that the distribution is constant and independent of position, for the time and spatial scale of the measurement has to be made. Figure 3.9 demonstrates that the velocity phase space is scanned along the v_x -axis, while the deflection voltage is stepped through. In the planes of constant v_x^{si} the instrument integrates over v_y and v_z as illustrated in Figure 3.10. Thus, we find

$$N_{si} \propto \rho_{si}(v_x^{si}) \quad (3.24)$$

with the 1D velocity phase space density given by

$$\rho_{si}(v_x^{si}) = \iint_{v_-(v_x^{si})}^{v_+(v_x^{si})} \rho_{si}(v_x^{si}, v_y, v_z) dv_y dv_z. \quad (3.25)$$

The limits of the integration result from the solid angle of the collimator, it defines a cone in velocity space (s. Fig. 3.9). From figure 3.10 we see that only a fraction of the above integral is measured. This fraction is called duty cycle. At this point we have to make an assumption about $\rho_i(x, y, z, v_x, v_y, v_z)$. By default a thermal distribution is assumed and the duty cycle, $D(\alpha, \beta)$, can be calculated (s. figures 3.9, 3.10, and 3.11). It depends on the instrumental Aspect Angle α and the Mach Angle β of the distribution. Equation 3.24 becomes

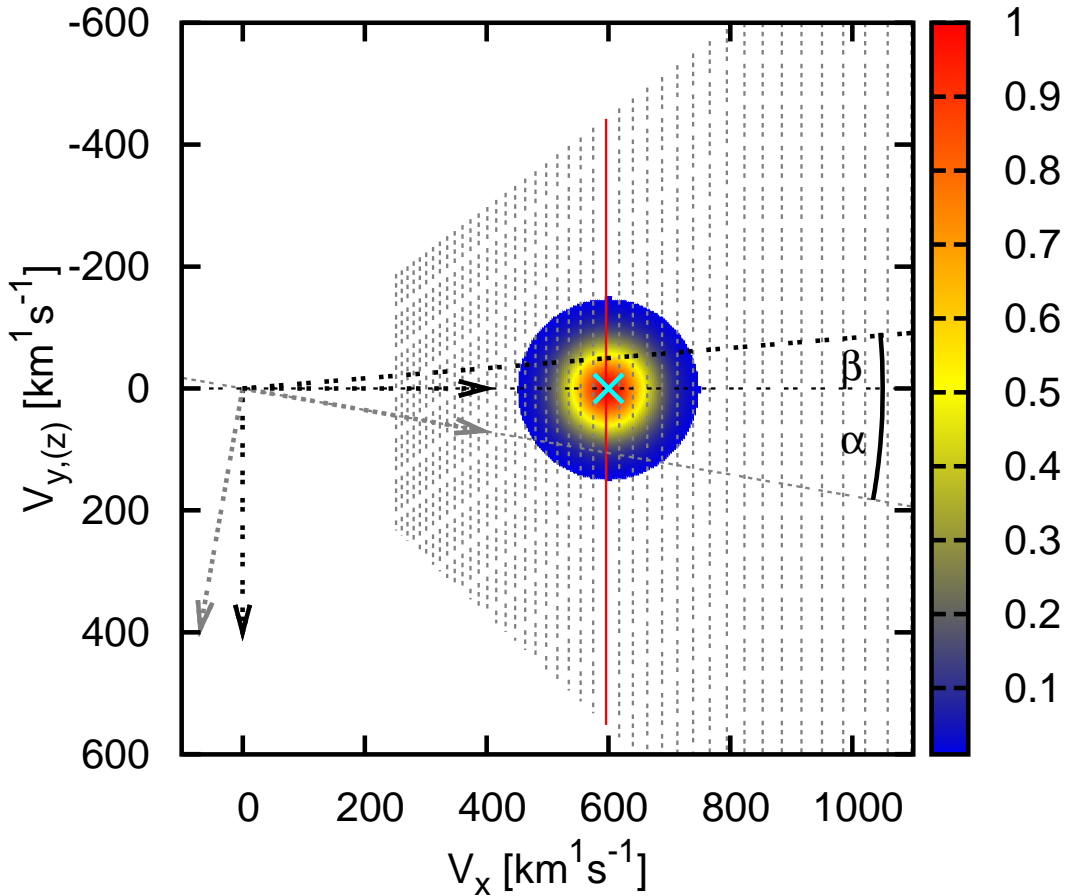


Figure 3.9: A 2D cut through a 3D thermal velocity distribution in velocity phase space is shown. Phase space density is colour-coded, solar wind speed $v_{sw} = 600\text{km}^1\text{s}^{-1}$, and thermal velocity $v_{th} = 50\text{km}^1\text{s}^{-1}$. The Sun-Earth line defines the X-axis. The Y-axis is chosen so that the spin axis of the spacecraft lies in the X-Y plane (dashed black arrows). The Z-axis (not shown) would complete the left handed triad. Spacecraft coordinates are rotated by the Aspect Angle $\alpha = 10^\circ$ (dashed grey arrows). The Mach Angle $\beta = \arctan \frac{v_{th}}{v_{sw}} = 4.8^\circ$. The acceptance of the electrostatic analyser for all $\frac{E}{q}$ -steps in the plotted range is shown by vertical dashed grey lines. Due to the geometry of the collimator, these lines would be segments of a circle (3D : spherical segments), but in the range of the distribution they are approximated as vertical lines (3D : planes). In Fig. 3.10 the Y-Z plane marked by the red vertical line is plotted to demonstrate how the dutycycle is calculated.

$$N_{si} \propto D(\alpha, \beta) \rho_{si}(v_x^{si}). \quad (3.26)$$

Furthermore, ions are only measured with the instrumental efficiency η_{si} . And the uncertainty of the electrostatic analyser $\Delta E/q = \pm 3\%$ corresponds to an integration over v_x

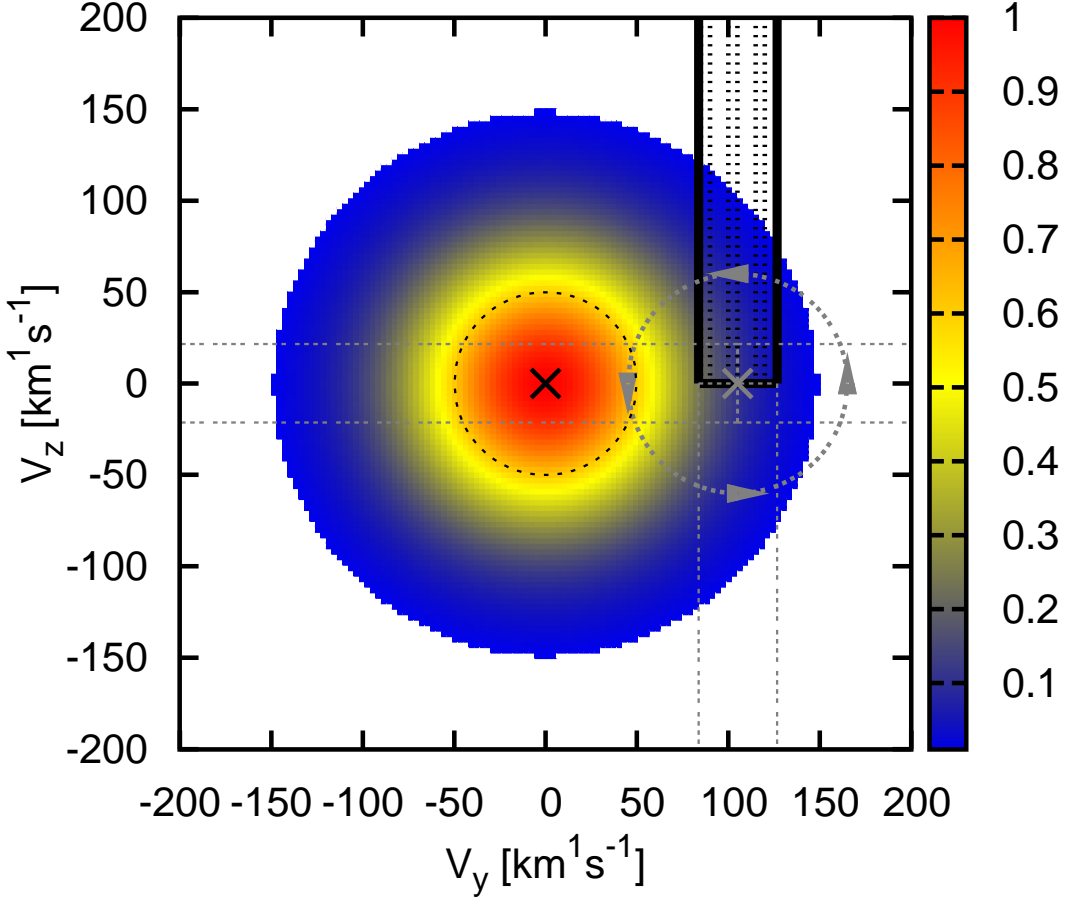


Figure 3.10: The Y-Z plane marked by the solid red line in Fig. 3.9 is shown. Phase space density is colour-coded, $v_x = 596\text{km}\text{s}^{-1}$, and thermal velocity $v_{th} = 50\text{km}\text{s}^{-1}$. The intersection of the X-axis is marked by the black cross in the centre of the distribution. The grey cross marks the intersection of the spacecraft's rotation axis and thus the tracing point of the collimator. The dashed black line shows the intersection of the Mach cone. To calculate the duty cycle, the mean percentage of the distribution that is covered by the collimator has to be calculated. Acceptance of the entrance system is indicated by the dashed area defined by the solid black lines. The rotation (dashed gray circle) of the collimator is indicated by the dashed gray lines. Obviously the duty cycle depends on the opening angle of the Mach Cone β and the instrumental Aspect Angle α (s. Fig. 3.11)

that can be approximated by a factor Δv_{si} . So we get

$$N_{si} \propto \eta_{si} \Delta v_{si} D(\alpha, \beta) \rho_{si}(v_x^{si}). \quad (3.27)$$

The last thing that has to be considered is the spatial volume of the measurement. It is given by

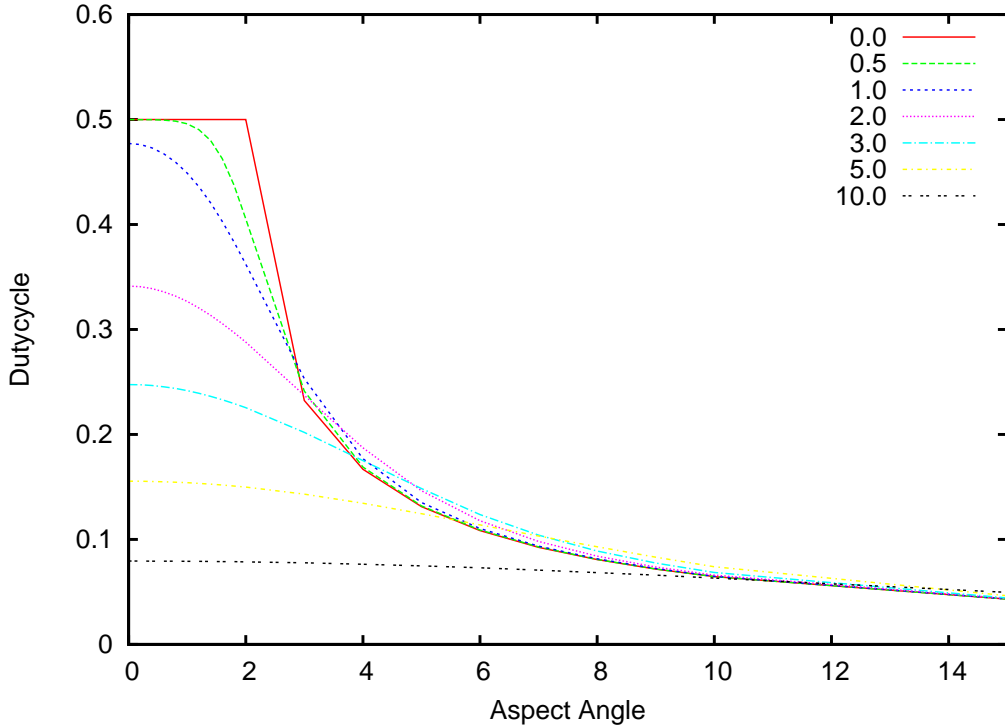


Figure 3.11: The duty cycle depending on the Aspect Angle is shown. Different colours and line-styles mark the corresponding Mach Angles.

$$V_{si} = v_{si}\tau g \quad (3.28)$$

where τ is the time of the measurement, typically 12s for a single spacecraft revolution and $g = 0.0225\text{cm}^2$ the active area of SWICS also called geometry factor. Finally, we get

$$N_{si} = v_{si}\tau g \eta_{si} \Delta v_{si} D(\alpha, \beta) \rho_{si}(v_x^{si}), \quad (3.29)$$

and

$$\rho_{si}(v_x^{si}) = \frac{N_{si}}{v_{si}\tau g \eta_{si} \Delta v_{si} D(\alpha, \beta)} \quad (3.30)$$

respectively. At this point, it should be emphasised that $D(\alpha, \beta)$ is the only parameter in equation 3.30 that is not defined by instrumental properties and hence introduces the greatest uncertainty to $\rho_{si}(v_x^{si})$. This topic is further discussed in section 5.2.

Once the velocity distribution is known, its moments can be calculated. They have a

physical meaning and are commonly used to describe the solar wind state. The absolute density is given by the zero order moment

$$n = \int_{-\infty}^{\infty} \rho(v_x) (v_x)^0 dv_x. \quad (3.31)$$

Solar wind speed, which is the velocity of the centre of mass, is the ratio of first and zero order moment

$$v_{sw} = \frac{\int_{-\infty}^{\infty} \rho(v_x) (v_x)^1 dv_x}{n}. \quad (3.32)$$

Mean kinetic energy in the solar wind frame of reference is given by the second order moment divided by the zero order moment and the mass m

$$\bar{E} = \frac{m}{2} \frac{\int_{-\infty}^{\infty} \rho(v_x) (v_x - v_{sw})^2 dv_x}{n}. \quad (3.33)$$

In the case of a thermal distribution, as is assumed for the standard duty cycle calculation, the velocity distribution is a one dimensional Maxwell-Boltzmann distribution, which has the form

$$F(v) = n \sqrt{\left(\frac{m}{2\pi k_B T}\right)} e^{-\left(\frac{m(v - v_{sw})^2}{2k_B T}\right)}. \quad (3.34)$$

From this, we can derive the temperature, T ,

$$\frac{k_B T}{m} = \frac{\int_{-\infty}^{\infty} f(v) (v - v_{sw})^2 dv}{n}. \quad (3.35)$$

Taking equations 3.33 and 3.37 together, we get the relation between mean energy and temperature

$$\bar{E} = \frac{k_B}{2} T. \quad (3.36)$$

Equation 3.33 can be written as

$$T = \frac{m}{k_b} \frac{\int_{-\infty}^{\infty} \rho(v_x) (v_x - v_{sw})^2 dv_x}{n}. \quad (3.37)$$

In general n, v_{sw} , and T are used to describe the kinetic state of solar wind ions.

4 Maximum Likelihood Analysis technique

In the previous chapter, the established analysis technique for SWICS data was described. Since it has major disadvantages dealing with low statistics (s. section 4.1), we have developed a new improved technique (s. section 4.2) that is statistically unbiased for small count rates (s. section 4.3). Furthermore, the concept of probabilistic rates has been improved (s. section 4.4). Our results are classified in the range of precursors (s. section 4.5) and some data products are presented (s. section 4.6).

4.1 Disadvantages of the standard analysis technique

If we search for rare ions, the analysis technique described in section 3.3 produces unsatisfactory results. Equations 3.20, and 3.21 respectively, become meaningful only if the rates are high enough that Gaussian-statistics can be assumed. This can be illustrated by a simple example. Let us assume two neighbouring ions whose spillover matrix is given by

$$\hat{S} = \begin{pmatrix} 0.47 & 0.1 \\ 0.1 & 0.47 \end{pmatrix}, \quad (4.1)$$

and the box-rate vector is

$$\vec{B} = \begin{pmatrix} 2 \\ 0 \end{pmatrix}. \quad (4.2)$$

From equation 3.20 we get

$$\begin{aligned} 2 &= 0.47n_1 + 0.1n_2, \\ 0 &= 0.1n_1 + 0.47n_2. \end{aligned} \quad (4.3)$$

Solving this set of equations gives

$$\begin{aligned} n_1 &= 4.46, \\ n_2 &= -0.95. \end{aligned} \quad (4.4)$$

This result is unphysical. If we exclude the second ion and assume it to be not present, we get

$$\begin{aligned} n_1 &= 4.26, \\ n_2 &= 0.00. \end{aligned} \tag{4.5}$$

In other words the result will be unphysical or rare ions have to be excluded. Generally it is essential that though \hat{S} is positive definite, \hat{S}^{-1} doesn't have to be. Ions with negative results have to be excluded and the method has to be applied until \hat{S}^{-1} is also positive definite. This procedure introduces a statistical bias for small count rates.

Additionally, only counts that fall into the boxes are taken into account. It is obvious that the widths of the boxes have to be chosen very carefully. If the widths are chosen too big, too many ions contribute, if they are too small, only a small fraction of the total counts are used. Normally the widths are set to $\sigma_\tau, \sigma_\epsilon$. This means that a fraction of ≈ 0.47 of the distribution is expected to be in the corresponding box. The other way around, in more than 50% of all cases a single count of an isolated ion won't be included in the corresponding box-rate. Returning to our simple example above, one can say that it is not unlikely that $b_2 = 0$ if $n_2 = 1$. Even if the probabilistic rates finally include all counts, they are of no use for ions that have been already found to be not present by the inversion method.

4.2 Improved Analysis technique

In the previous section, the need for an analysis technique that is statistically unbiased when dealing with small count rates has been pointed out. The idea of our technique is to determine the ion distributions in the E-T matrices directly using a maximum likelihood fit.

For the fitting, a standard Levenberg-Marquardt algorithm *Press et al.* [1992] has been modified to allow 2D fitting. As a first step, the fit has been used to determine the Instrumental Response Functions as described in section 3.2. Due to the good statistics in the long-term data, a standard χ^2 Maximum Likelihood Estimator (MLE) was taken. For typical time resolutions (12 minutes, 1 hour, 1 day), the situation is completely different. Figure 4.1 shows a typical E-T matrix of one hour data. Obviously, the count rates at the majority of points (T_{CH}, E_{CH}) are governed by Poissonian, not by Gaussian statistics. Therefore, a MLE based on Poissonian statistics instead of a standard χ^2 estimator has to be used (s. section 4.3). Since the IRFs are now known (s. section

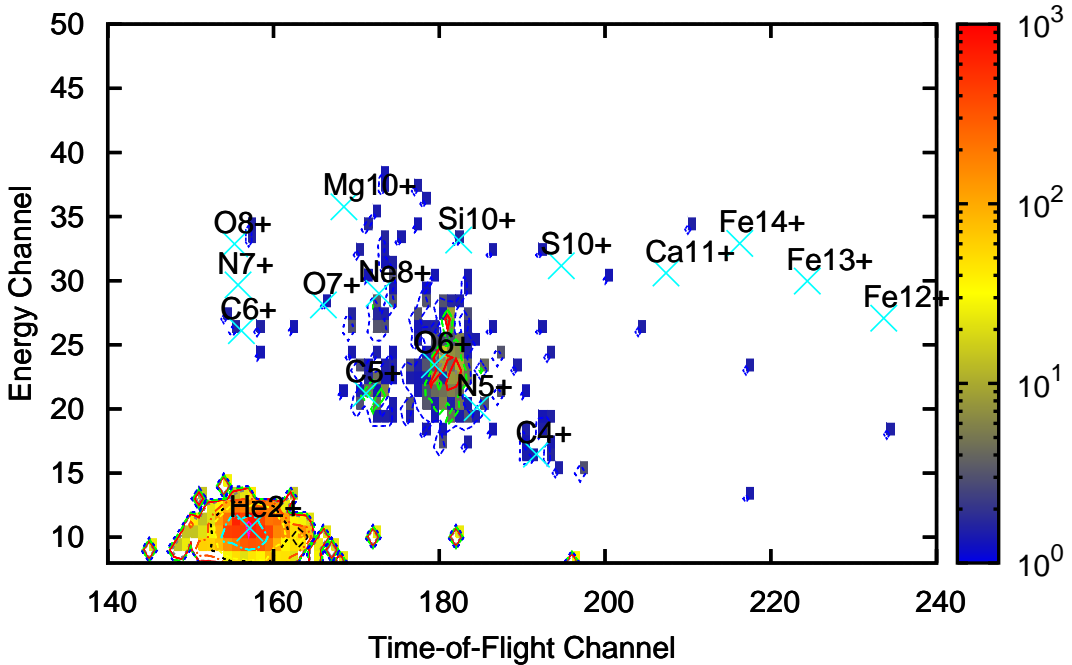


Figure 4.1: An example 1h data E-T matrix of E/q step 40, together with the position (light blue crosses) of some ions is shown. ISO-contour lines are spaced as in Fig. 3.5, but starting at 10^0 . The count rates at most of the points are very low and thus governed by Poissonian and not by Gaussian statistics.

3.2) and normalised to unity, the number of free parameters per ion is reduced to one. This free parameter is the volume of the distribution function, or, in other words, the count rate of the ion. However, one has to keep in mind that, due to the strong overlap of the IRFs, the ions can't be fitted separately. Additionally, counts from ions that are not included in the analysis will falsify the results. Thus, we have to fit as many ions as possible, and if possible simultaneously.

Although the computing time scales at least with the square of the number of the free parameters, we have chosen a list of about 80 ions for our standard analysis. Starting values are calculated based on the 1σ box-rates (s. section 3.3.1). In the case of empty boxes, starting values are set to 0.15. This assures that rare ions can be properly adjusted by the fit. The instrumental response functions are calculated out to 3σ , so that basically all counts are taken into account.

It is in the nature of the fit that the sum of the results does not equal the total number of counts. In order to make fitting not even more complicated, the total number of counts is not taken as an additional constraint. Instead, the results are taken to calculate the

4.2 Improved Analysis technique

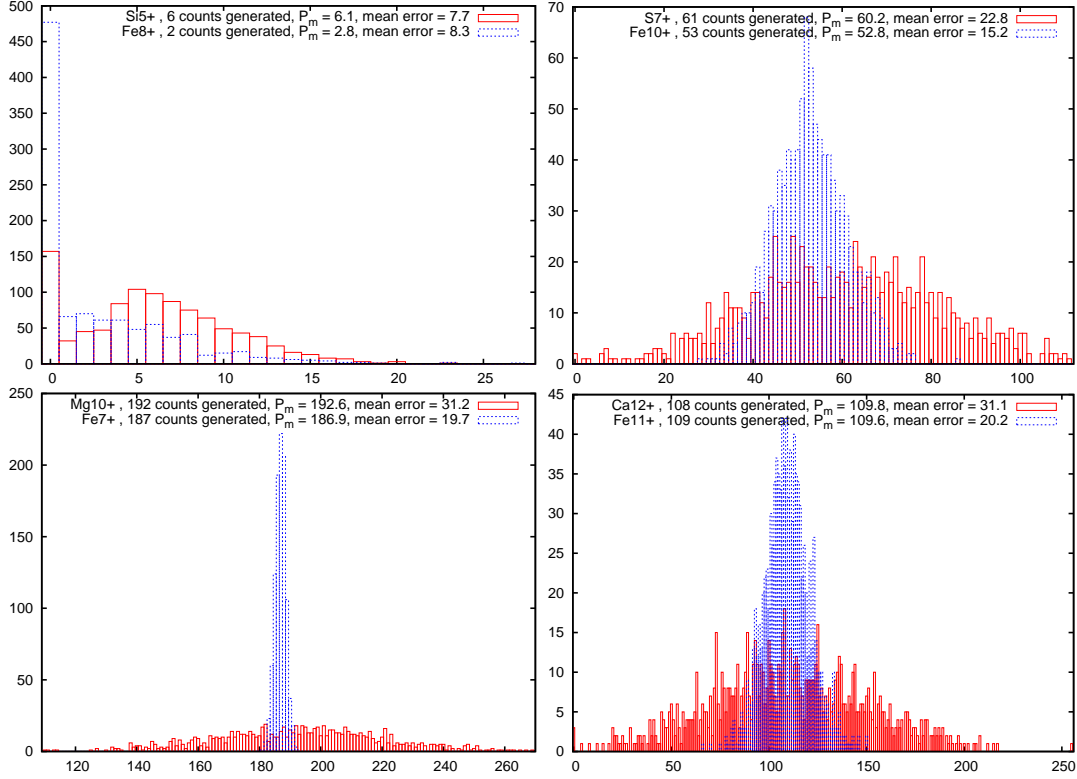


Figure 4.2: One thousand sets of artificial data with randomly chosen but fixed numbers of counts for each ion species, that is by default in our analysis, have been generated and our analysis has been applied. The four plots show the histograms of the results for several ion species. The number of results (Y-axis) is plotted against the resulting probabilistic rates (X-axis). For each ion species the number of generated counts, the mean result (P_m) and the mean error is given. It can be seen that the histograms of two ions with almost similar number of counts may strongly differ from each other. The surrounding peaks have a considerable influence on the results. The mean result in all cases is in very good agreement with the number of generated counts. The mean error from our analysis represents the error of the mean result from the histograms in varying quality.

probabilistic rates according to section 4.4. This serves, in addition to the standardisation to the actual number of counts, as a stabilisation of the results in the cases where the fit got stuck or produces runaways. In spite of the great number of parameters, the probabilistic rates are stable and reliable as demonstrated in Figure 4.2. Even the errors we get from the fitting seem to be in overall good shape.

4.3 Maximum Likelihood Fitting

The core of a maximum likelihood fit is the MLE. Generally spoken, it has to be a computable quantity that depends on the model parameters, and provides a measure how likely the measurements correspond to our model. The most common MLE is the χ^2 . If we have N data points (x_i, y_i) with normally distributed errors around the “true” model with the standard deviation, σ_i , and a model with M adjustable parameters, $y(x; a_1 \cdots a_M)$, the probability that a single measurement belongs to the model is given by

$$P_i(\vec{a}) = \frac{1}{\sqrt{2\pi}\sigma_i} e^{-\frac{(y_i - y(x_i; \vec{a}))^2}{2\sigma_i^2}} \Delta y. \quad (4.6)$$

Some fixed Δy is needed if y_i are continuous values. Taking all points into account we get the probability

$$P(\vec{a}) = \prod_{i=1}^N P_{i\vec{a}} \quad (4.7)$$

that the measurements come from our model. Thus maximising $P(\vec{a})$ will give us the most likely set of parameters. For computational reasons it is easier to minimise

$$-\ln(P(\vec{a})) = \sum_{i=1}^N \frac{(y_i - y(x_i; \vec{a}))^2}{2\sigma_i^2} - \sum_{i=1}^N \frac{1}{\sqrt{2\pi}\sigma_i} - N\ln(\Delta y), \quad (4.8)$$

which is equivalent to maximising equation 4.7. Since $\sigma_i, N, \Delta y$ are all constant, we have to minimise

$$\chi^2 = \sum_{i=1}^N \frac{(y_i - y(x_i; \vec{a}))^2}{2\sigma_i^2}. \quad (4.9)$$

As said above, the χ^2 is commonly used for fitting purposes. But as showed above it is based on the assumption of Gaussian statistics. In our case, Poissonian statistics have to be used , thus, equation 4.6 becomes

$$P_i^P(\vec{a}) = \frac{y(x_i; \vec{a})^{y_i}}{y_i!} e^{-y(x_i; \vec{a})} \Delta y \quad (4.10)$$

and consequently, equation 4.8 will become

$$-\ln(P_P(\vec{a})) = \sum_{i=1}^N [(y(x_i; \vec{a}) - y_i \ln(y(x_i; \vec{a})))] + \sum_{i=1}^N \ln(y_i!) - N\ln(\Delta y). \quad (4.11)$$

Again the last two terms are constant, so that we finally get our MLE

$$E_P(\vec{a}) = \sum_{i=1}^N [(y(x_i; \vec{a}) - y_i \ln(y(x_i; \vec{a}))]. \quad (4.12)$$

In order to use a Levenberg-Marquardt algorithm to minimise $E_P(\vec{a})$ we have checked if it has a quadratic form around its minimum, which can be written as

$$E_P(\vec{a}) \approx \gamma - \vec{d} \cdot \vec{a} + \frac{1}{2} \vec{a} \cdot \hat{D} \cdot \vec{a} \quad (4.13)$$

with, up to a constant factor, \vec{d} equal to the gradient and \hat{D} equal to the Hessian matrix of $E_P(\vec{a})$. The terms with the second derivatives in $\frac{d\chi^2}{da_i da_j}$ are dismissed as they are small enough. The algorithm then switches between the inverse Hessian and the steepest descend method applying a factor λ , that is adjusted during the fit, to the diagonal elements of \hat{D} .

4.4 Advanced Probabilistic Rates

We have taken up the concept of the probabilistic rates (s. section 3.3.3) to determine our final count rates. Analogously, the distributions are calculated using the results of our fit. Equation 3.23 gives the probabilities $P_{si}(\tau, \epsilon)$ for E/q step s at each position in the E-T matrix C_s that a count belongs to ion species i . At this point we need to emphasise that we have already all informations we can get. We simply have to distribute each bin according to these probabilities

$$N_{si}^P = \sum_{Tch} \sum_{Ech} P_{si}(\tau, \epsilon) \cdot C_s(\tau, \epsilon) \quad (4.14)$$

No additional dice roll is needed. On the contrary, any kind of dice roll introduces a new moment of uncertainty. If the dice is rolled infinitely often and, which is always important to remember if random numbers are used, the dice is ideal, the mean result will equal the one we already had by knowing the probabilities. Therefore, a single dice roll will falsify our results that are already the most likely ones under all assumptions we have made. One has to keep in mind that we have to discard the idea that we can clearly decide that a single count belongs to a certain ion species. Imagine a single count that lies in the range of two neighbouring IRFs. Certainly the particle that was counted either belonged to species one or to species two. But it is essential that under the given conditions we can not decide the real nature of the particle. The best thing we can do, is

4 Maximum Likelihood Analysis technique

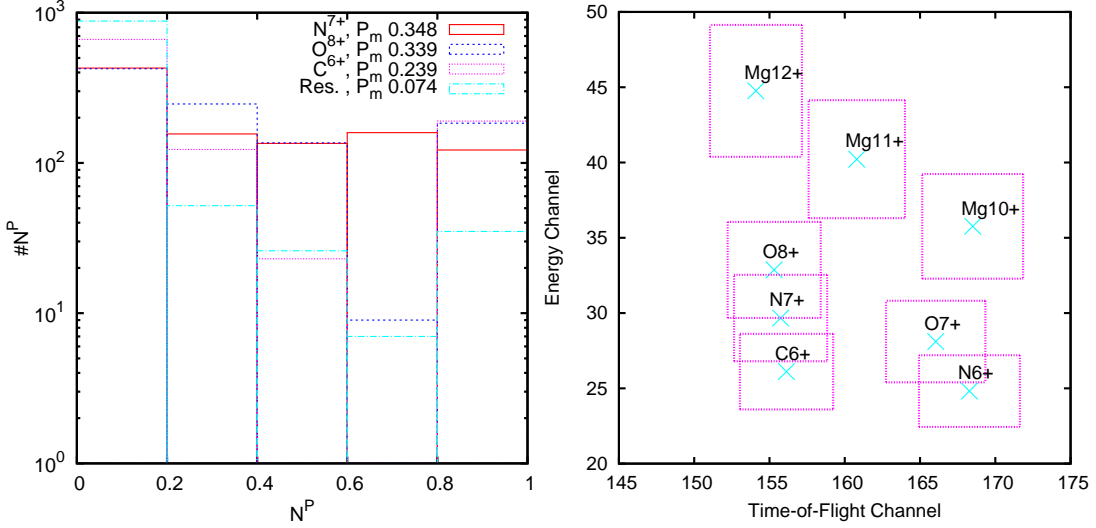


Figure 4.3: Left panel : One thousand sets of artificial data with a single count N^{7+} in E/q step 30 have been generated and analysed. A histogram of the probabilistic rates of all surrounding ions and their mean result is shown. The results of $N^{6+}, O^{7+}, Mg^{10+}, Mg^{11+}$ and Mg^{12+} are summarised (Res.).

Right panel : The positions of the surrounding ions together with their 1σ -boxes are shown.

to make a statistical estimate about the probability for the one or the other alternative. To illustrate this fact, we have generated 1000 sets of artificial data. Based on the IRF of N^{7+} , for each set a single count is generated and our analysis is applied to the virtual data. The left panel of figure 4.3 illustrates how this single count, which we know to be N^{7+} , is assigned by our method. It can be seen that the assignment in most cases, is not unique. The right panel shows the position of the ions in the vicinity of N^{7+} . C^{6+} , N^{7+} , and O^{8+} are very poorly separated, thus it seems reasonable that their mean results lie close together. It has to be mentioned that the poor separation of these three ions, due to their equal ratio of $\frac{m}{q}$ and their similar masses, is an extreme case. Therefore, the above can be taken as a worst case scenario for our analysis.

4.5 Comparison with others

Here, we compare our analysis method with the standard analysis method described in section 3.3. To test the goodness of our maximum likelihood analysis technique and of the re-determined instrumental response functions we have checked against results from the “official” axlv2 data processor from the University of Michigan (personal communica-

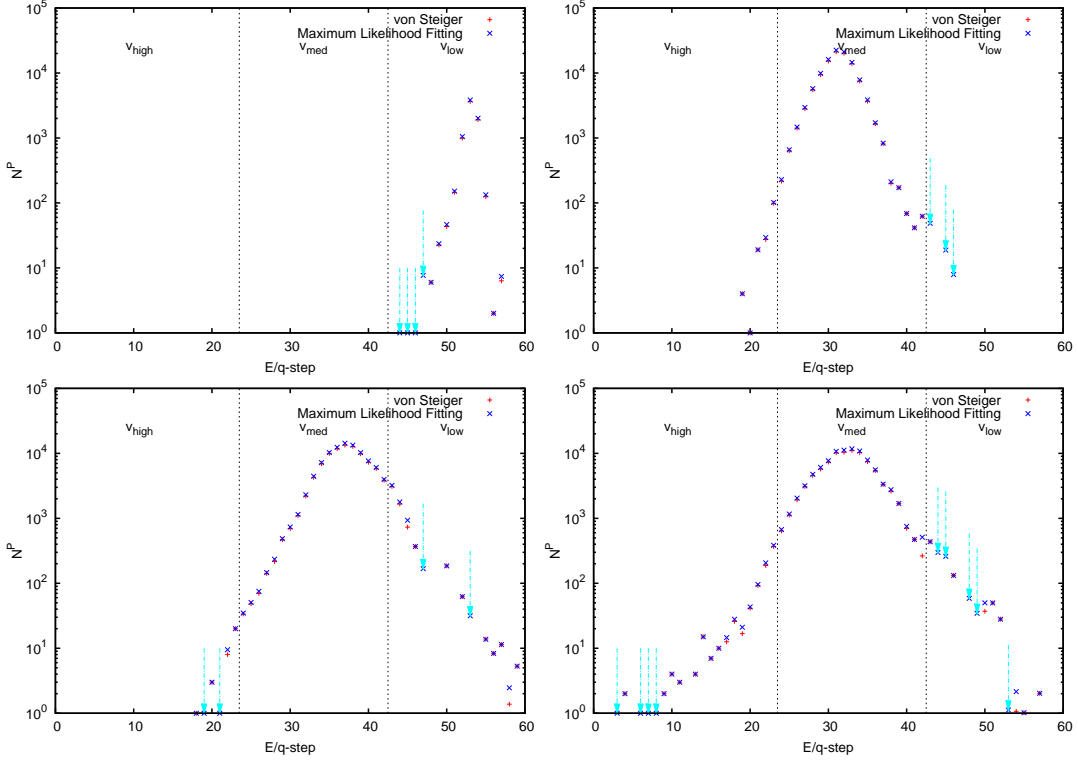


Figure 4.4: The velocity distribution of He^{2+} probabilistic rates from an example of one hour data is shown. The results from our maximum likelihood analysis technique are compared to the analysis after v. Steiger. Both are in overall good agreement. While the discrepancy in the core of the distribution is mainly due to our re-determined and improved IRFs, in the tail additionally our improved technique is more capable of analysing low count statistics. Three velocity ranges $v_{low} < 450 \text{ km s}^{-1}$, $450 \text{ km s}^{-1} < v_{med} < 900 \text{ km s}^{-1}$, and $900 \text{ km s}^{-1} < v_{high}$ are separated by the vertical dotted black lines. The two upper plots show examples of undisturbed slow (left, DoY 26.44), and fast (right, DoY 4.06) solar wind. The two lower plots show examples of CIRs (left, DoY 15.52; right, DoY 29.77). All examples are from year 2007. The light blue arrows mark points where only our method has a non zero result.

tion). The axlv2 data processor uses the standard analysis technique described in section 3.3. Departing from it, the probabilistic rates are calculated using a single dice-roll not for each single count but for each position in the E-T matrices as a whole. From now on we will refer to MLF for our maximum likelihood analysis method and to SVD for the standard analysis. January in 2007 has been analysed in 1 hour resolution. Level zero data in both cases have been translated into the E-T matrices by the axlv2 data processor. For our analysis the matrices have additionally been binned as described in section 3.2.

4 Maximum Likelihood Analysis technique

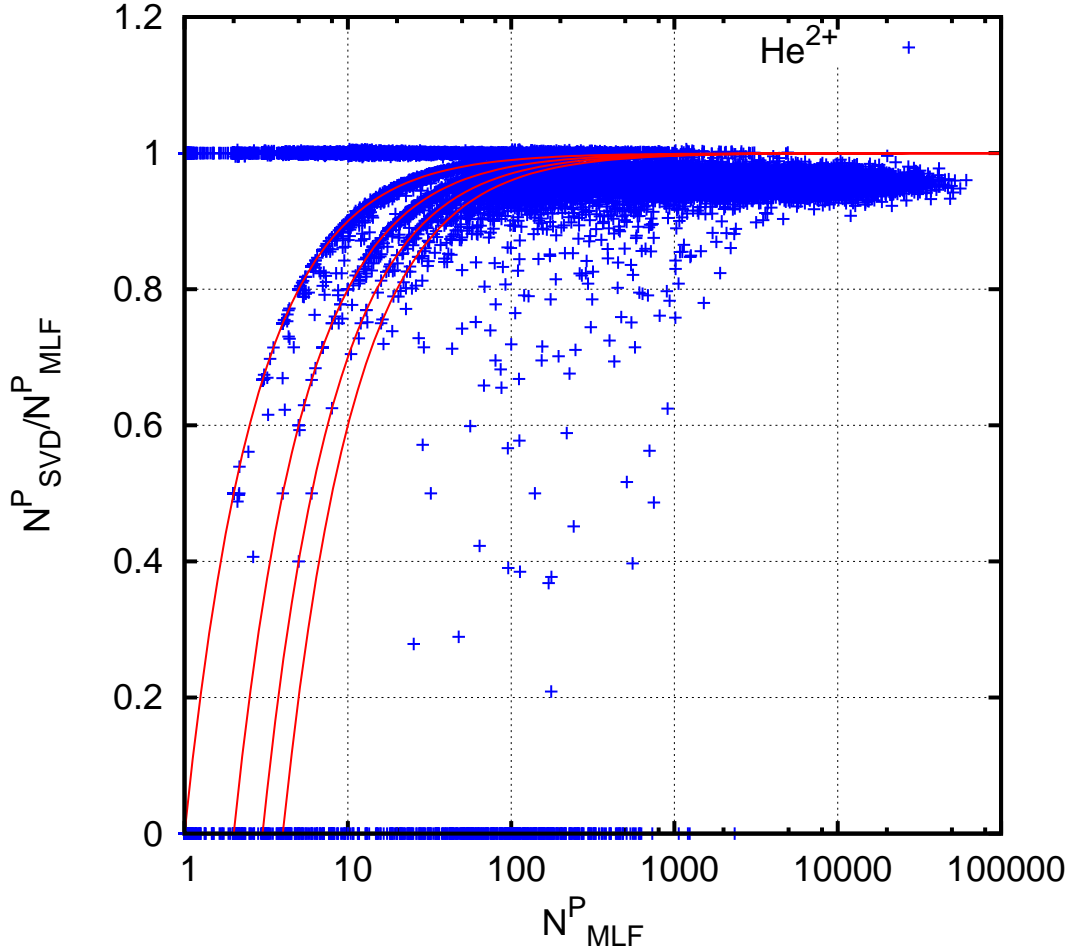


Figure 4.5: The He^{2+} ratio of the probabilistic rates from the v. Steiger method N_{SVD}^P to the ones from our maximum likelihood fit N_{MLF}^P is plotted against our rates. The red lines from left to right show expected curves for the cases that 1,2,3, and 4 bins have not been properly assigned in the N_{SVD}^P .

Due to its high abundance in the solar wind and its well isolated position, the results of He^{2+} should look very similar. Thus, it is a good example to point out the differences of the two methods. Figure 4.4 shows 4 sample one-hour spectra. The cores of the distributions are in good agreement, while MLF count rates are slightly but systematically increased. Additionally, there are several cases in the flanks where MLF has counts while SVD has none. They are marked by arrows. Mainly low count rates are affected, but there are also examples up to some hundred counts. Figure 4.5 illustrates that the above features are ubiquitous. The ratio of SVD to MLF results is plotted against MLF results. Up to about one thousand counts there are two sequences with ratio ≈ 1 , and

Velocity	N	N_{MLF}	N_{SVD}	N_{ALL}	S	S_{MLF}	S_{SVD}	S_{ALL}	S_{RES}
all	15537	0.112	0.001	0.887	1449	0.568	0.000	0.413	0.019
low	5916	0.114	0.000	0.886	190	0.532	0.000	0.437	0.032
med	8400	0.078	0.002	0.920	776	0.545	0.000	0.436	0.019
high	1221	0.328	0.000	0.672	483	0.619	0.000	0.366	0.014

Table 4.1: He^{2+} detection efficiency of the SVD- and the MLF-method are compared. First column is the velocity range (all=whole range, low= $v_{low} < 450 \text{km s}^{-1}$, med= $450 \text{km s}^{-1} < v_{med} < 900 \text{km s}^{-1}$ and high= $900 \text{km s}^{-1} < v_{high}$). N is the total number of points where any method has non zero result. The N_i are the fractions of N where either only one (MLF,SVD) or both (ALL) methods have non zero results. S is the number of points where any method has found exactly one count. The S_i are the corresponding fractions. Additionally S_{RES} summarises the cases where either method found a single count and the other found more.

ratio 0. In between the ratio is arranged along curves. These curves emerge from two mechanisms. At first the dice-roll that is used to get the probabilistic rates can create them. It produces discrete values, while our method produces continuous results. The red lines show curves for the cases that 1,2,3, and 4 bins have been assigned to other ions. The two sequences at 1 and 0 give the cases where all, and no bins have been assigned to He^{2+} respectively. Secondly the same effect might be explained by differences in the used instrumental response functions. Counts that lie in the range of the MLF function don't have to be in the range of the SVD and vice versa. Thus, similar to the effect that single bins are assigned to another ion by the dice-roll, they might contribute to only one method. With this in mind we can interpret figure 4.5. In principle both methods are in good agreement. The shape of the distribution can be explained by the above considerations. Now we try to interpret the fact that the ratio does not exceed 1 and tends towards 0.95. To understand this, one has to consider the following facts. He^{2+} lies mostly isolated and there is nearly no background in the data. Thus, all assigned counts should actually be He^{2+} . Additionally He^{2+} is shifted towards adjacent heavy ions in the SVD IRFs, according to the MLF IRFs. Taking the above together it is very unlikely that MLF results are increased due to pollution from neighbouring ions and that what we see is really He^{2+} . On the other hand it is very likely that SVD misses counts due to the shifted IRFs or by wrong assignment via dice-roll. That is why it is reasonable to expect ratios between 0 and 1. The higher the count rates get the more likely it is that the ratio tends to a certain fraction. This comes from the fact that the two different IRFs each cover a certain fraction of the real instrumental response. For high count rates i.e., good

4 Maximum Likelihood Analysis technique

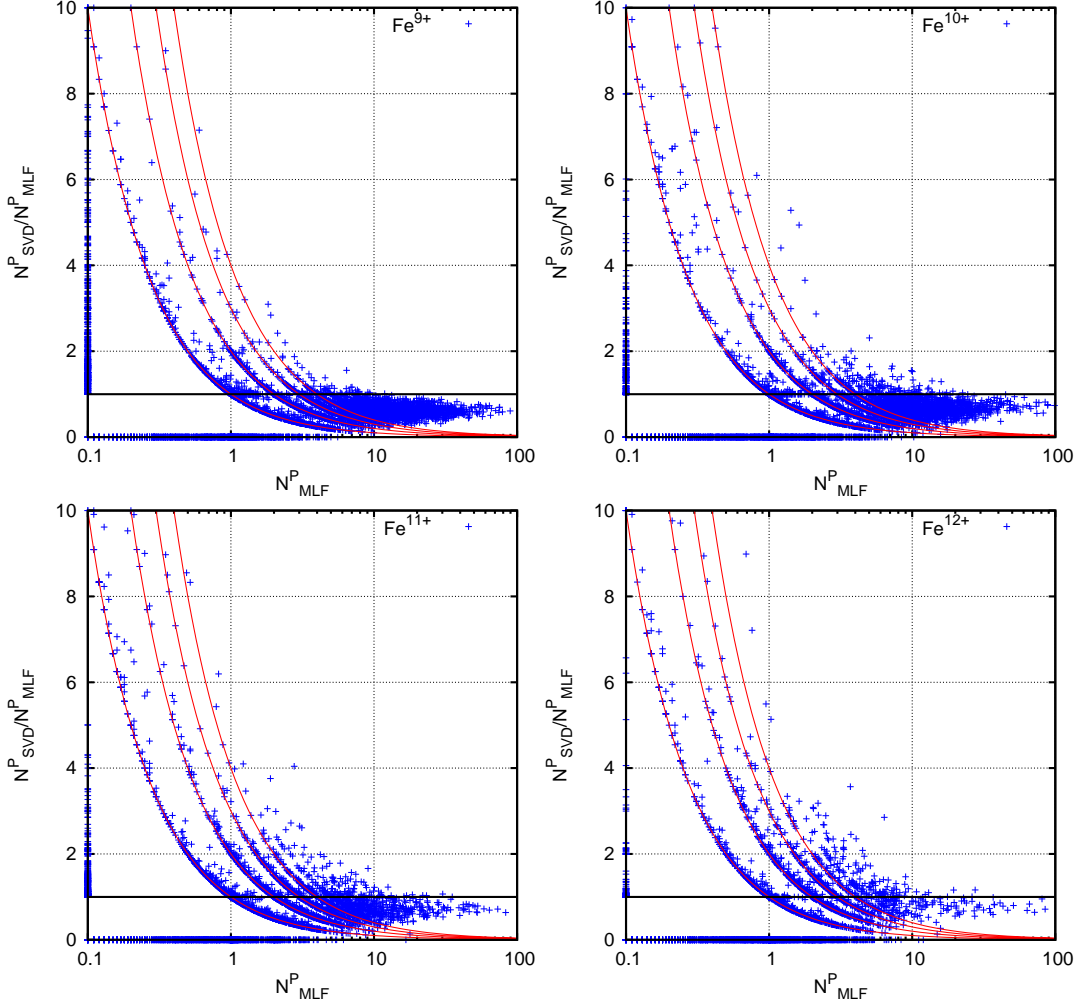


Figure 4.6: The ratio of the probabilistic rates from the v. Steiger method N^P_{SVD} to the ones from our maximum likelihood fit N^P_{MLF} is plotted against our rates. Fe^{9+} , Fe^{10+} , Fe^{11+} , and Fe^{12+} (from upper left to lower right) are shown. The red lines from left to right show expected curves for the cases that 1,2,3, and 4 bins have not been properly assigned in the N^P_{SVD} .

statistics, the ratio of the results should converge towards the ratio of the coverages. Lastly we have compared the detection efficiencies. The total number of table 4.1 summarises the results. The number of cases in which any method has a non zero result is compared to the cases where either only one method or both produced non zero results. To put the focus on low count rates the same is done for the cases where a single count has been found by either method. The quantities are given for the whole ensemble v_{all} and for three velocity ranges $v_{low} < 450\text{km s}^{-1}$, $450\text{km s}^{-1} < v_{med} < 900\text{km s}^{-1}$, and $900\text{km s}^{-1} < v_{high}$ respectively. It can be seen that our method under all conditions is

Velocity	N	N_{MLF}	N_{SVD}	N_{ALL}	S	S_{MLF}	S_{SVD}	S_{ALL}	S_{RES}
Fe ⁹⁺ all	6327	0.177	0.099	0.723	1999	0.378	0.042	0.237	0.343
Fe ⁹⁺ low	3027	0.206	0.198	0.595	995	0.413	0.064	0.214	0.309
Fe ⁹⁺ med	3297	0.150	0.009	0.841	1001	0.344	0.019	0.259	0.379
Fe ⁹⁺ high	3	0.333	0.000	0.666	3	0.333	0.000	0.666	0.000
Fe ¹⁰⁺ all	5802	0.242	0.050	0.707	2037	0.439	0.047	0.171	0.344
Fe ¹⁰⁺ low	2612	0.281	0.087	0.632	965	0.494	0.046	0.147	0.313
Fe ¹⁰⁺ med	3189	0.210	0.021	0.769	1071	0.388	0.048	0.192	0.372
Fe ¹⁰⁺ high	1	1.000	0.000	0.000	1	1.000	0.000	0.000	0.000
Fe ¹¹⁺ all	4993	0.263	0.112	0.625	2273	0.420	0.098	0.161	0.321
Fe ¹¹⁺ low	2254	0.265	0.146	0.589	937	0.464	0.106	0.156	0.274
Fe ¹¹⁺ med	2738	0.261	0.083	0.656	1335	0.389	0.093	0.164	0.354
Fe ¹¹⁺ high	1	1.000	0.000	0.000	1	1.000	0.000	0.000	0.000
Fe ¹²⁺ all	3687	0.456	0.042	0.502	1873	0.574	0.039	0.134	0.253
Fe ¹²⁺ low	1477	0.432	0.020	0.548	679	0.605	0.009	0.144	0.242
Fe ¹²⁺ med	2210	0.472	0.056	0.472	1194	0.557	0.056	0.128	0.259
Fe ¹²⁺ high	0	0.000	0.000	0.000	0	0.000	0.000	0.000	0.000

Table 4.2: Fe detection efficiency of the SVD- and the MLF-method are compared. Arrangement of the columns is the same as in Table 4.1. In the first column additionally the ion name is given. In contrast to Helium the single count values include all cases $0 < N^P \leq 1$ not only $N^P = 1$.

more efficient in detecting He²⁺. In the range of solar wind velocities where the count rates tend to be high (v_{low}, v_{med}) the overall efficiency of the SVD-method in respect to the MLF-method is 0.887. That means that in about 10% of all cases the SVD-method is not able to find He²⁺ while we do. At higher solar wind velocities (v_{high}), where the count rates tend to be very low, this efficiency goes down to 0.672. For the special yet important case of single count detection it even drops down to 0.413. It has to be mentioned that a loss of about 10% of the points doesn't translate into a 10% loss of counts. If the IRFs are shifted towards each other then the points that get lost are in the slope of the distribution, thus, the loss of counts must be lower than the loss of points, as can be seen in figure 4.5.

While He²⁺ has the lowest energies, Fe has the highest energies. Therefore, we have made the same comparisons, as for He²⁺, for Fe. Figure 4.6 shows the ratios of the results for Fe⁹⁺, Fe¹⁰⁺, Fe¹¹⁺, and Fe¹²⁺. There are some differences to figure 4.5. To understand the distribution, some things have to be considered. Indeed Fe has the highest energies of all observed ions, but in contrast to He²⁺ there is overlap with lighter ions and with

4 Maximum Likelihood Analysis technique

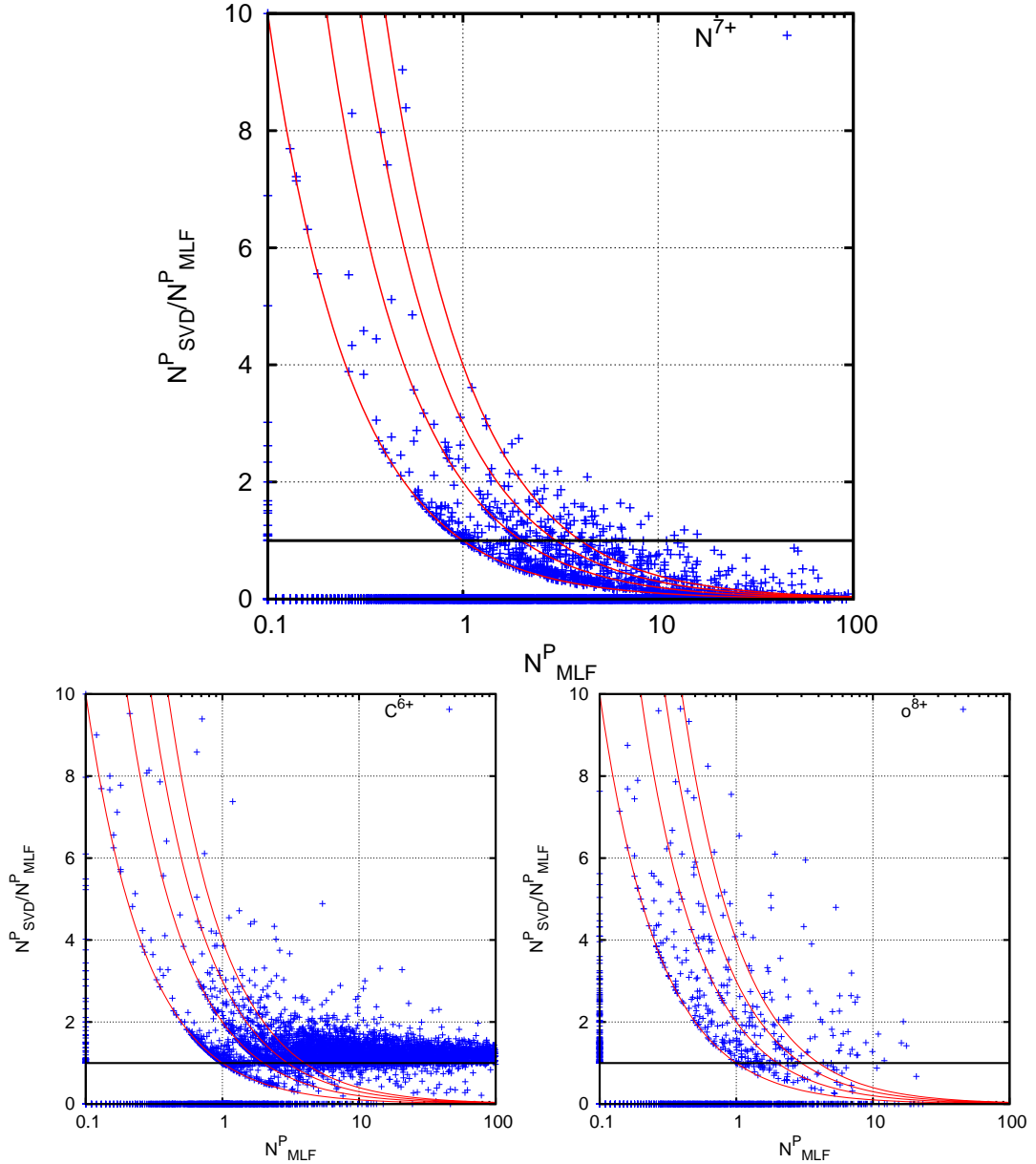


Figure 4.7: The ratio of the probabilistic rates from the v. Steiger method N^P_{SVD} to the ones from our maximum likelihood fit N^P_{MLF} is plotted against our rates. The red lines from left to right show expected curves for the cases that 1,2,3, and 4 bins have not been properly assigned in the N^P_{SVD} .

neighbouring Fe states of charge. Consequently our continuous probabilistic rates can get smaller than one, while the SVD-rates are discrete. The sequences marked by the red lines in contrast to figure 4.5 are given by cases where 1,2,3, and 4 counts have been found by

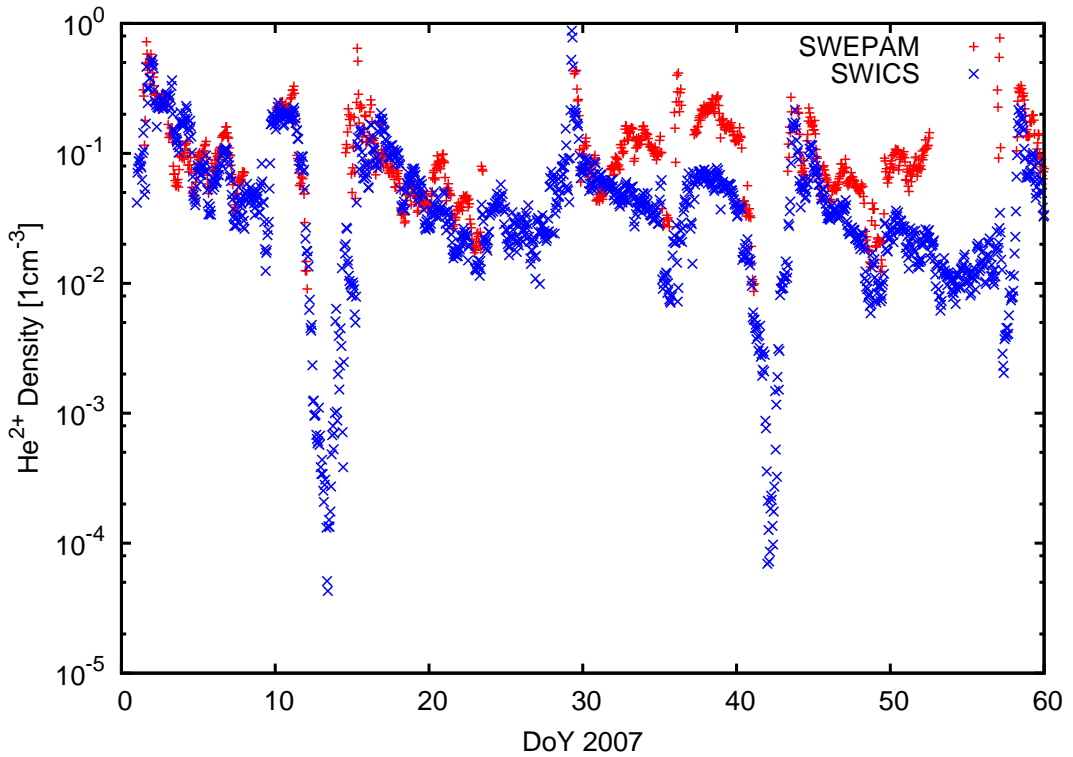


Figure 4.8: A comparison between the absolute He^{2+} densities from our analysis and from SWEPM is shown. The agreement between both varies and seems to be systematically worse in the second half. The time frames in which SWEPM has more or less large gaps in the data, are fully covered by our SWICS data.

the SVD-method. Due to the logarithmic scaling of the X-axis the points for $N_{MLF}^P = 0$ are plotted at $N_{MLF}^P = 0.1$. Again the SVD positions are shifted but in the opposite direction. They lie closer to lighter ions, namely calcium that is not even included in the SVD-analysis. We don't expect to see ions beyond Fe, and expect Ca to have lesser abundance than Fe. Thus, as for He^{2+} , the ratio should tend to a given fraction, that is determined by the coverages of the IRFs. This trend is observed for all shown Fe charge-states and, as before, this fraction is smaller than one. Hence, we conclude that our IRFs for Fe are again in better agreement with the real instrumental response. The sequence along the Y-axis and the points with ratios greater than one are very likely polluted by calcium that has been miss-assigned by the SVD-method. If we compare the detection efficiencies (s. table 4.2), the picture is also not clear as for He^{2+} . Under all conditions, significant fractions are detected by either method. We can state that N_{MLF} is always greater than N_{SVD} and that N_{ALL} decreases with higher charge-states. The fact that

4 Maximum Likelihood Analysis technique

N_{ALL} is significantly decreased compared to He^{2+} while N_{MLF} and N_{SVD} are increased, together with the conclusion that our IRFs are in better agreement with the instrument, supports the thesis that the SVD-rates are polluted by other ions, most likely calcium. The values for single counts also confirm this theory.

In section 3.2 we have pointed out that all ions have been treated consistently for the calculation of the IRFs. If we argue that our IRFs are better for He^{2+} and the Fe sequence, it is very likely that they are also better for ions in between. It has also been stated that some ions in the SVD-model show strange behaviour. Because contamination by other ion species will be strong for intermediate ions the distributions can't be interpreted as easily as for He^{2+} and Fe.

Finally we have compared the results of C^{6+} , N^{7+} and O^{8+} . This triad is to some extent separated from other ions, while the difficulty in separating them from each other has already been discussed in section 4.4. Figure 4.7 shows the ratio of the two methods. The SVD-method finds more C^{6+} while N^{7+} is depleted. For O^{8+} it seems that the results are hardly correlated. If we again compare the positions, we find that C_{SVD}^{6+} is slightly shifted towards N_{MLF}^{7+} , while N_{SVD}^{7+} and O_{SVD}^{8+} both lie closely together due to a shift of O_{SVD}^{8+} towards N_{MLF}^{7+} . Thus it seems reasonable that C_{SVD}^{6+} is increased due to contamination by N^{7+} while N_{SVD}^{7+} is depleted. It seems that O_{SVD}^{8+} strongly confuses O^{8+} and N^{7+} .

Summarising all comparisons between the SVD- and the MLF-method we state that our instrumental response functions seem to be in much better agreement with the actual instrumental response. Overall, our MLF-method seems to be significantly better in low count rate situations.

As a last check we compare the He^{2+} densities that are derived from our probabilistic rates (s. 3.4) with results from SWEPAM. Figure 4.8 shows the results from both instruments for the first 60 days of year 2007. In the first 30 days they agree very well. Two large gaps in the SWEPAM data are covered by our results. From day 30 up to day 60 our densities are systematically decreased. Nevertheless, larger gaps in the SWEPAM data are covered. Both time frames cover all kind of solar wind as well as CIRs, thus, we can hardly think of any mechanism that could falsify our results to the observed deviations in the second and not in the first timeframe.

4.6 Data Products

In section 3.4 the path from count rate spectra to physical values is described. We have used our maximum likelihood analysis technique described in this chapter to calculate

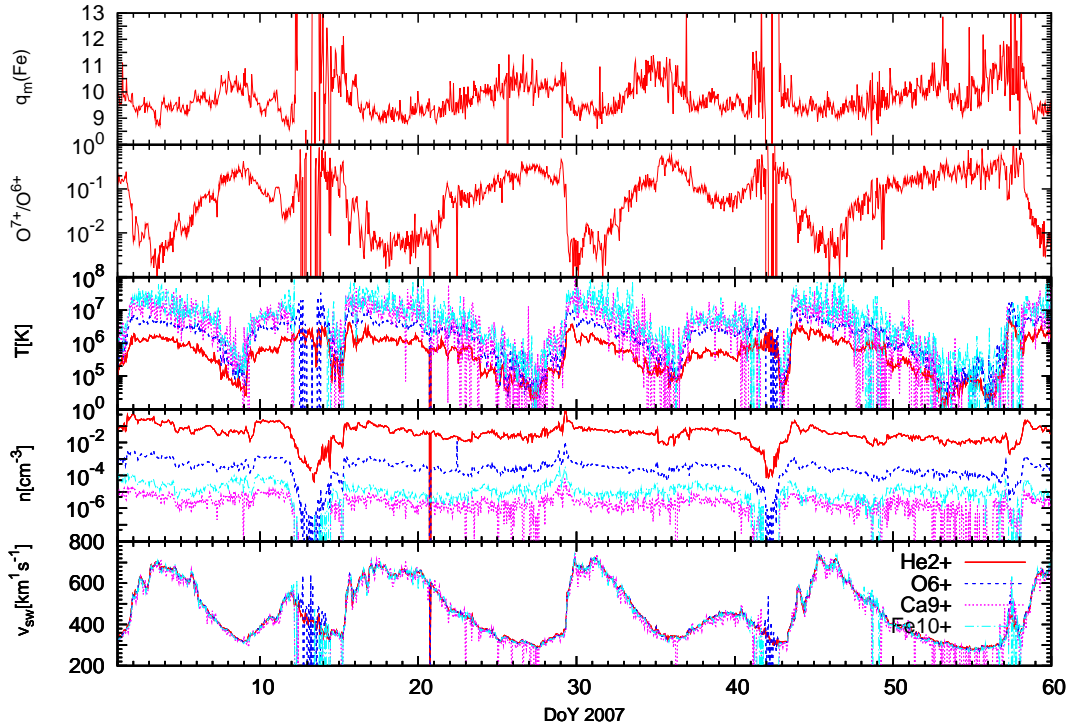


Figure 4.9: An example of one hour data products for the first 60 days of year 2007 are shown. The three panels from bottom show solar wind speed, absolute density, and temperature of He^{2+} , O^{6+} , Ca^{9+} and Fe^{10+} . The upper two panels show the ratio $\text{O}^{7+}/\text{O}^{6+}$, and the mean iron charge-state respectively

solar wind parameters for a great variety of ions. So far, results in one hour resolution from year 2001 up to 2007 are available. In figure 4.9 some sample data products are shown.

5 Velocity Distribution Functions

It is common to characterise solar wind ions by their features bulk speed, density and temperature. They can be derived from the VDFs (s. section 3.4). With the usage of these quantities the assumption of a thermalised VDF is implicit. It is shaped by coulomb collisions and it can be described by a Maxwell-Boltzmann distribution. Observations have shown that the 3D VDFs of protons and alpha particles are to some extent highly non-thermal *Marsch et al.* [1982b], which is especially distinct in the fast solar wind.

Figure 5.1 shows two examples of 1D VDFs of He^{2+} measured by SWICS. For comparison fitted one dimensional thermal distributions are shown. Both distributions clearly deviate from the fits. Because the fit is largely determined by the core the core is well represented by the fits. However, the flanks are not well reproduced. Close to the centre on either side a tail arises. Up to higher velocities these tails suddenly flatten at a certain point. The actual shape varies strongly in time, but these features are ubiquitous in the observations. The flat tails that extend the solar wind to higher energies are called suprathermal tails. Their study is of great interest because of the underlying acceleration processes. This topic is briefly addressed in section 7.1. However, the focus of this work is on the velocity distributions of heavy ions in the solar wind. To explain the features of the observed velocity distributions we have set up a model for the VDFs (s. section 5.1) and a virtual detector (s. section 5.2) to address two main questions:

1. What is our best knowledge of solar wind VDFs?
2. Which part of the velocity distributions does SWICS measure?

5.1 3D Velocity Distribution Functions

The velocity phase space has three dimensions. In section 3.4 we have outlined that SWICS measures one dimensional cuts through this space, integrating over the other two dimensions. In the case of a symmetric distribution, a lot of simplifications can be made and we are able to calculate the 3D distribution from the 1D measurements. But are the

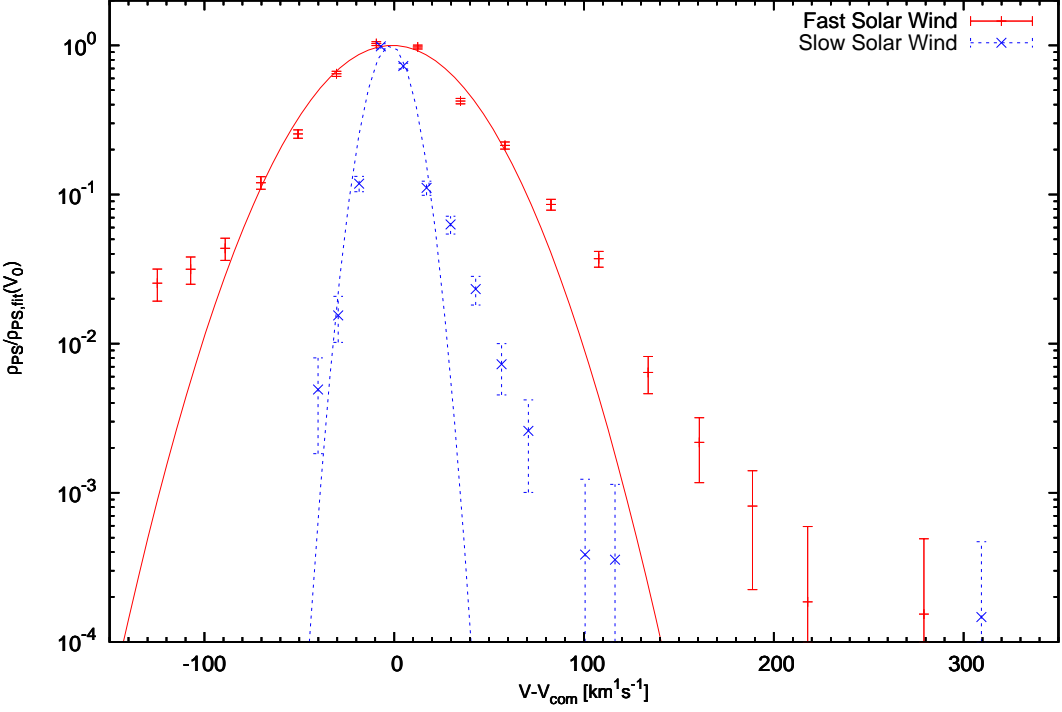


Figure 5.1: Two examples of VDFs of He^{2+} in 12 minutes resolution are plotted. Fast solar wind data (red) is from Day of Year (DoY) 5.6, slow solar wind (blue) from DoY 8.48. The solid red and the dashed blue lines are corresponding fitted thermal distributions. On the X-axis is the velocity in respect to the centre of mass. The Y-axis gives the ratio of the phase space density ρ_{PS} and maximum of the fit $\rho_{PS,FIT}(V_0)$

distributions really fully symmetric? The answer is no.

From Helios observations, we know what the 3D VDFs of protons and to some extent of helium look like. In Figures 5.2 and 5.3 examples from Marsch *et al.* [1982a, b] of these observations are shown. Some general features are :

1. Double peak structure - Core and Beam that are aligned with the magnetic field
2. Temperature anisotropy in respect to the magnetic field $\frac{T_\perp}{T_\parallel} \neq 1$, where T_\parallel and T_\perp equals the temperature parallel and perpendicular to the magnetic field.
3. Differential streaming - $v_{\text{He}^{2+}} > v_{\text{H}^{1+}}$

The formation of these features is still a topic of discussion. The most promising candidate to explain this features is wave particle interaction. Heuer and Marsch [2007] found that cyclotron resonant absorption of Alfvén waves leading to diffusion plateaus in velocity phase space could explain the heating of proton cores. In Figure 5.4, which is taken

5 Velocity Distribution Functions

MARSCH ET AL.: SOLAR WIND PROTONS

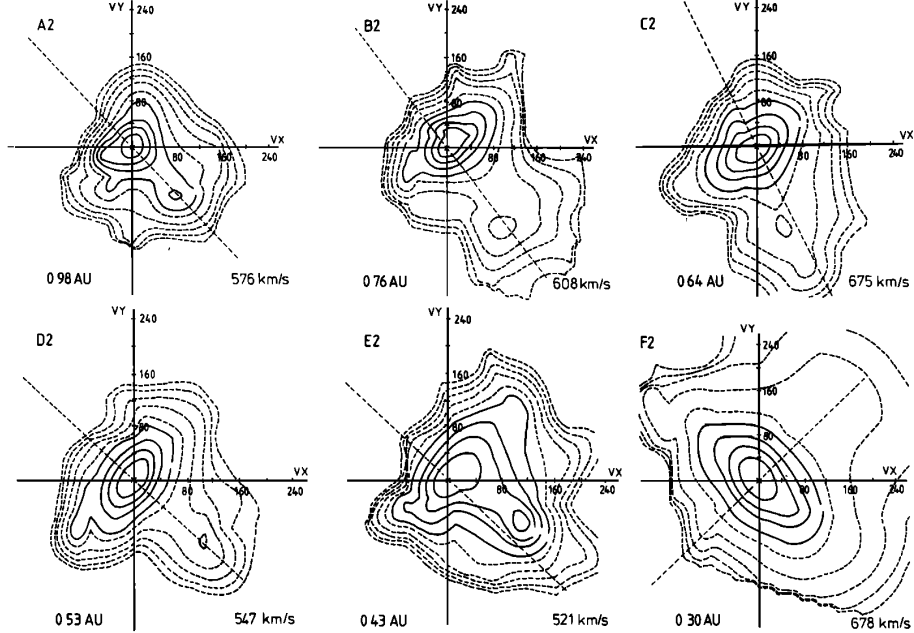


Figure 5.2: Proton velocity distributions measured by Helios 2 for different radial distances and velocities are shown. The cuts through the three-dimensional distributions are provided in a plane defined by the bulk velocity vector (VX-axis) and the magnetic field vector (dashed line). Contour lines correspond to fractions 0.8, 0.6, 0.4, 0.2 of the maximum phase space density (continuous lines) and logarithmically spaced to fractions 0.1, 0.032, 0.01, 0.0032, 0.001 (dashed lines), respectively. The origin of velocity space is defined by the velocity of the maximum phase space density and scales are given in $\text{km}^1 \text{s}^{-1}$. From Marsch et al. [1982b]

from Heuer and Marsch [2007], observed distributions are compared to derived diffusion plateaus. Although their calculations reproduce the observations well, they state that a drifting bi-Maxwellians can also reproduce the observations including the beam up to the same degree. Araneda et al. [2008] simulated the effect of parametrically unstable Alfvén-cyclotron waves on the VDFs. Figure 5.5, which is taken from Araneda et al. [2008], displays the temporal evolution of a VDF under the influence of these waves. The formation of a beam and reshaping of the core, retaining an initial temperature anisotropy can be seen. The drift velocity between beam and core is about the Alfvén-speed, in close agreement with observations.

Concluding the above-mentioned, we have modelled VDFs as drifting 3D bi-Maxwellians. Core and beam have the same temperature anisotropy $\frac{T_{\perp}}{T_{\parallel}} \neq 1$. Drift velocity between both is v_{drift} . The position of the core is taken as \vec{v}_{core} . In magnetic field coordinates

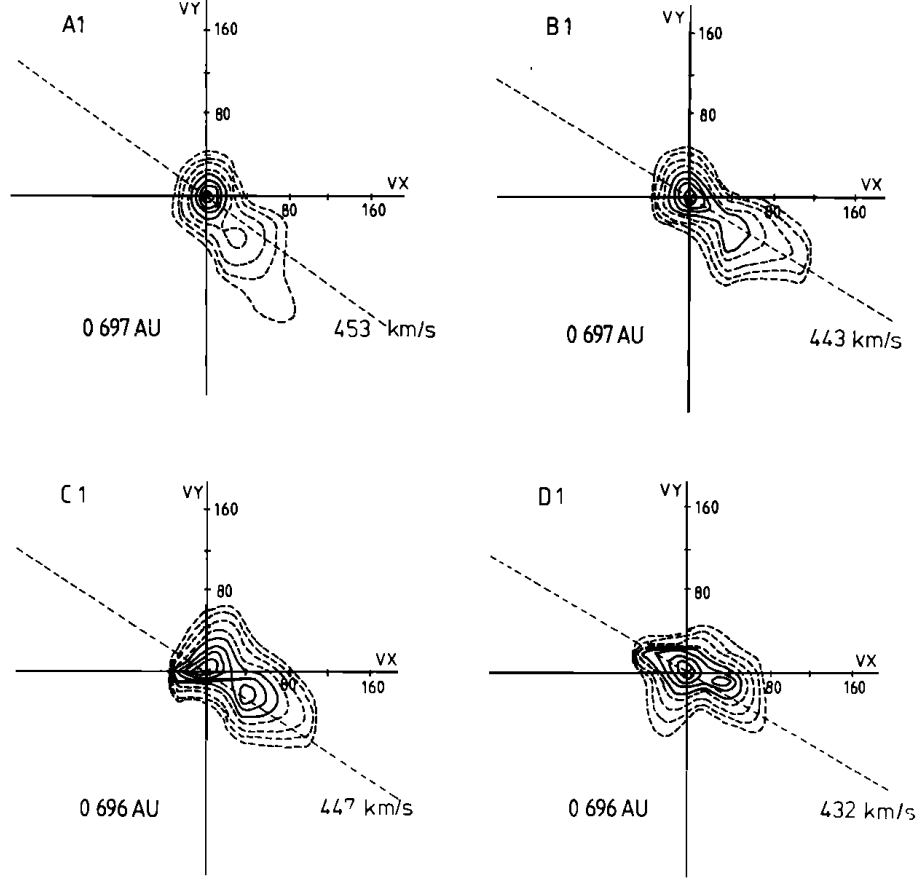
MARSCH ET AL.: SOLAR WIND HELIUM IONS

Figure 5.3: Helium velocity distributions at roughly the same radial distance and velocity are shown.

Arrangement of the plots as in fig. 5.2. From Marsch et al. [1982a].

(X-axis is defined by the magnetic field vector) the phase space density is given by

$$\rho(v_x, v_y, v_z) = \sum_{j \in \{core, beam\}} A_j \prod_{i \in \{x, y, z\}} g(v_i)_j \quad (5.1)$$

with

$$g(v_i)_j = e^{\frac{(v_i - v_{i,core})^2}{2v_{th,i}^2}} \quad (5.2)$$

for all but the X-component of the beam, which is given by

$$g(v_x)_{beam} = e^{\frac{(v_x - (v_{x,core} + v_{drift}))^2}{2v_{th,i}^2}}. \quad (5.3)$$

5 Velocity Distribution Functions

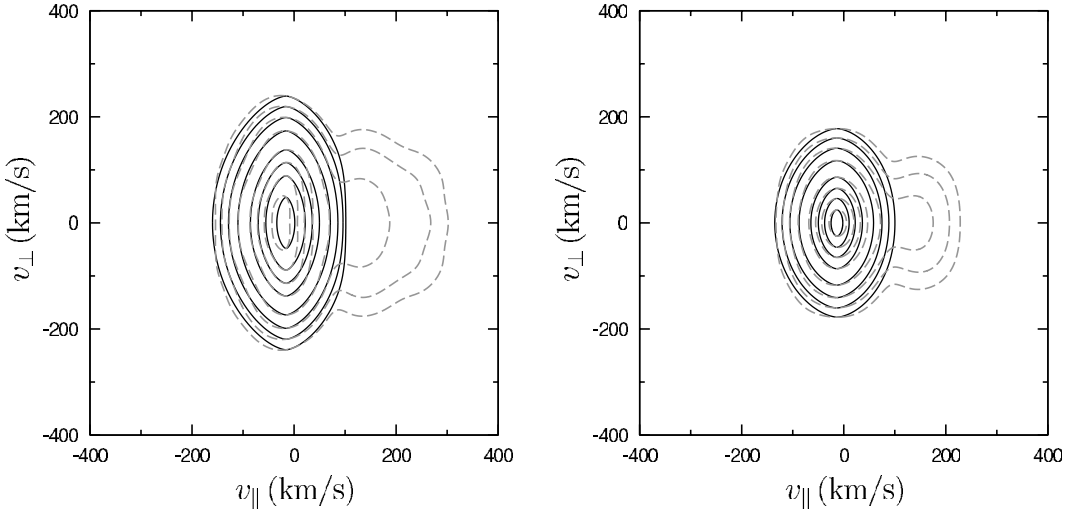


Figure 5.4: Contours of the gyrotropic part of two proton VDF are shown: (left) VDF of 14 April 1976 and (right) VDF of 16 March 1976. Theoretically predicted diffusion plateaus are superimposed which have the same v_{\perp} intercepts at the center of the core. The contours correspond to fractions 0.9, 0.7, 0.5, 0.3, 0.1, 0.03, 0.01, and 0.003 of the maximum of each distribution function. From *Heuer and Marsch [2007]*.

A_j scales the intensity of core and beam, respectively. The thermal velocity vth_i is given by the Temperature T_i and the mass of the ion m_{ion} by

$$vth_i = \sqrt{\frac{k_b T_i}{m_{ion}}}. \quad (5.4)$$

From equation 5.1 follows that the velocity vectors (first moment of the distribution) of two different ions may show differential streaming that is aligned with the magnetic field, e.g. if they have the same v_{core} but different ratios $\frac{A_{beam}}{A_{core}}$.

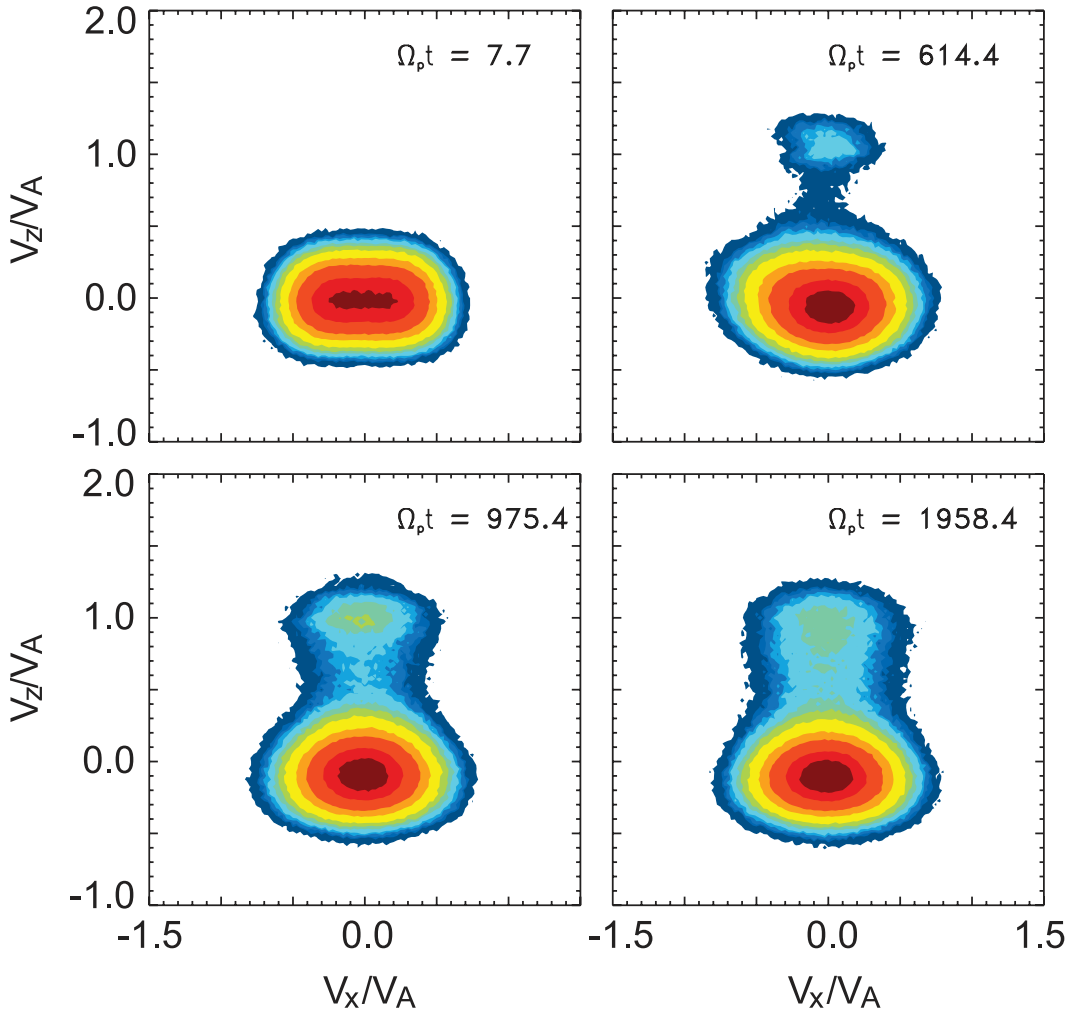


Figure 5.5: Contour plots of the proton VDF in the (v_x, v_z) plane for the dispersive-wave case at four instants of time. The color coding of the contour lines corresponds, respectively, to 75 (dark red), 50 (red), 10 (yellow) percent of the maximum, with a final beam density of about 7%. From Araneda *et al.* [2008].

5.2 Virtual Detector

The shape of observed VDFs depends on the design of SWICS and on the shape of the real 3D velocity distributions. In 3.4 the standard assumption of a thermal distribution and its consequences for data analysis has been outlined. This assumption does not hold true, as has been pointed out in the previous section. Originally some information about the entrance direction of incoming ions was to be included in the PHA data. One revolution was divided into eight sectors so that together with the identification of the SSD, that was triggered for the energy measurement, the direction of arrival would have been known, at least in a coarse grid. Unfortunately, for reasons unknown to us, both pieces of information are incorrect in the Level zero data. Therefore, we are given no information about the distribution from the data itself.

Hence, we have taken distributions as given by equation 5.1 and analysed them with a virtual detector. In section 3.4 we described how the instrumental count rates translate into phase space density. Thus, we built the virtual detector based on equation 3.29, and replaced the standard duty-cycle by a new one that takes the shape of the model VDF into account. Figure 5.6 demonstrates how the virtual detector scans velocity phase space. In contrast to the situation that is shown in figure 3.9, we have to deal with three coordinate systems. The main frame of reference for the phase space is marked by the grey arrows. It is given by Geocentric Solar Ecliptic (GSE) coordinates, with inverted X-axis pointing from Sun to Earth. We will refer to it as Solar centric Earth Ecliptic (SEE) coordinates. The second system are Space Craft (SC) coordinates marked by the black arrows. The magenta arrows mark the third system, given by Magnetic Field (MF) coordinates. According to SEE coordinates, SC and MF coordinates can be rotated independent of each other in the Ecliptic plane and additionally out of the Ecliptic. For reasons of presentability only the rotation in the ecliptic is shown in figure 5.6. Because of the alignment of the beam with the magnetic field the distribution reaches further away from the X-axis. Therefore, the approximation that planes of constant v_x are scanned has been discarded and the actual distribution along spherical segments is used for calculations. These segments are indicated in figure 5.6 by the grey segments of a circle with $r = v(E/q)$. The projection of the red segment onto the Y-Z plane is shown in figure 5.7. As in figure 3.10 the scan performed by the rotating collimator is indicated. It is obvious that the duty-cycle in contrast to the standard duty-cycle (s. 3.4) is no longer uniquely defined by the Aspect- and the Mach-Angle. Additionally we have taken into account the new detector efficiencies from *Köten* [2008]. The efficiencies used in this

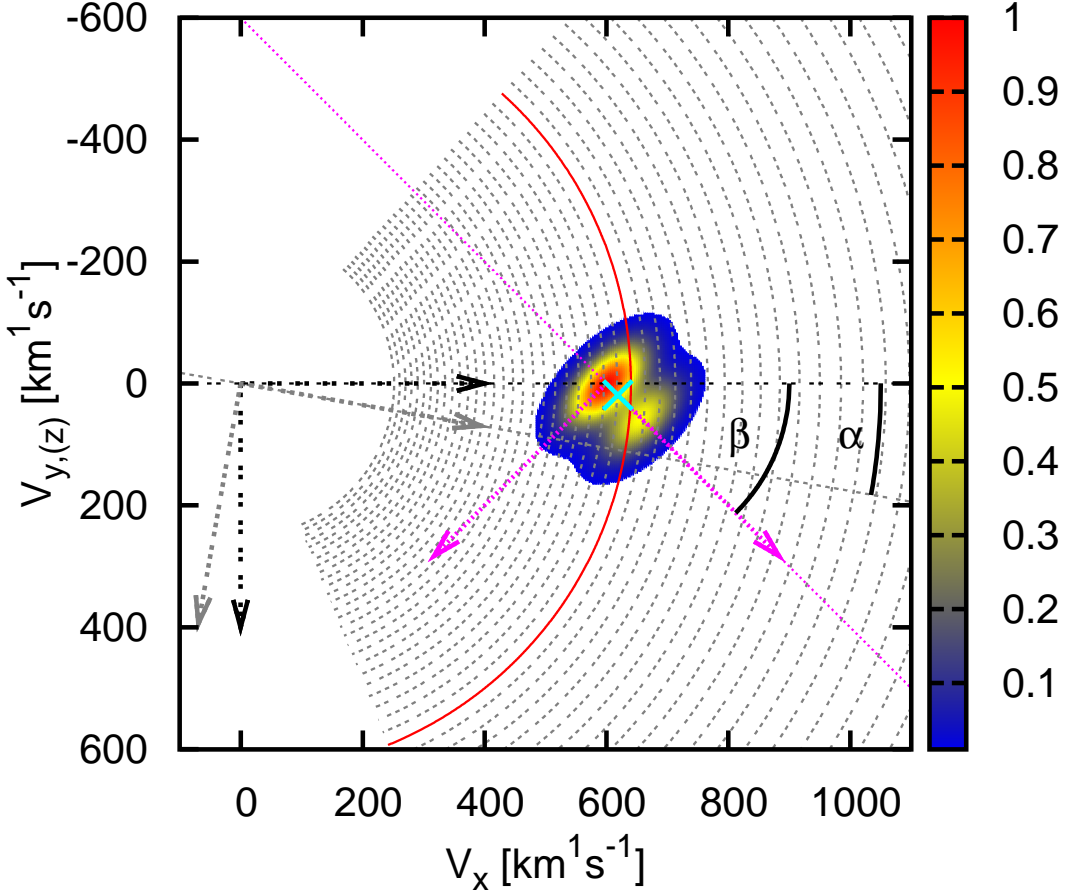


Figure 5.6: A 2D cut through the 3D velocity phase space of a velocity distribution with $v_{core} = 600 \text{ km}^{-1}\text{s}^{-1}$, $v_{drift} = 80 \text{ km}^{-1}\text{s}^{-1}$, $vth_{\parallel} = 25 \text{ km}^{-1}\text{s}^{-1}$, $vth_{\perp} = 50 \text{ km}^{-1}\text{s}^{-1}$, and $A_{Beam}/A_{Core} = 0.5$ is shown. Relative intensities are colour coded. The centre of mass of the distribution is identified by the light blue cross. The arrows mark the orientation of X- and Y-axis of different coordinate systems (black=SEE, grey=SC, magenta=MF). $\alpha = 5^\circ$ is the angle between SC and SEE coordinates. $\beta = 45^\circ$ is the angle between MF and SEE coordinates. The dashed grey segments of a circle show the acceptance of the collimator of SWICS. A cut along the spherical segment indicated by the solid red line is shown in figure 5.7.

work do not only depend on ion species and energy but also on the angle of incidence. We get for the duty-cycle

$$D_{adv}(m, q, E/q, \alpha_{EP}, \alpha_{\perp EP}, \beta_{EP}, \beta_{\perp EP}, v_{sw}, v_{alf}, vth_{\perp}, vth_{\parallel}, A_{Core}, A_{Beam}). \quad (5.5)$$

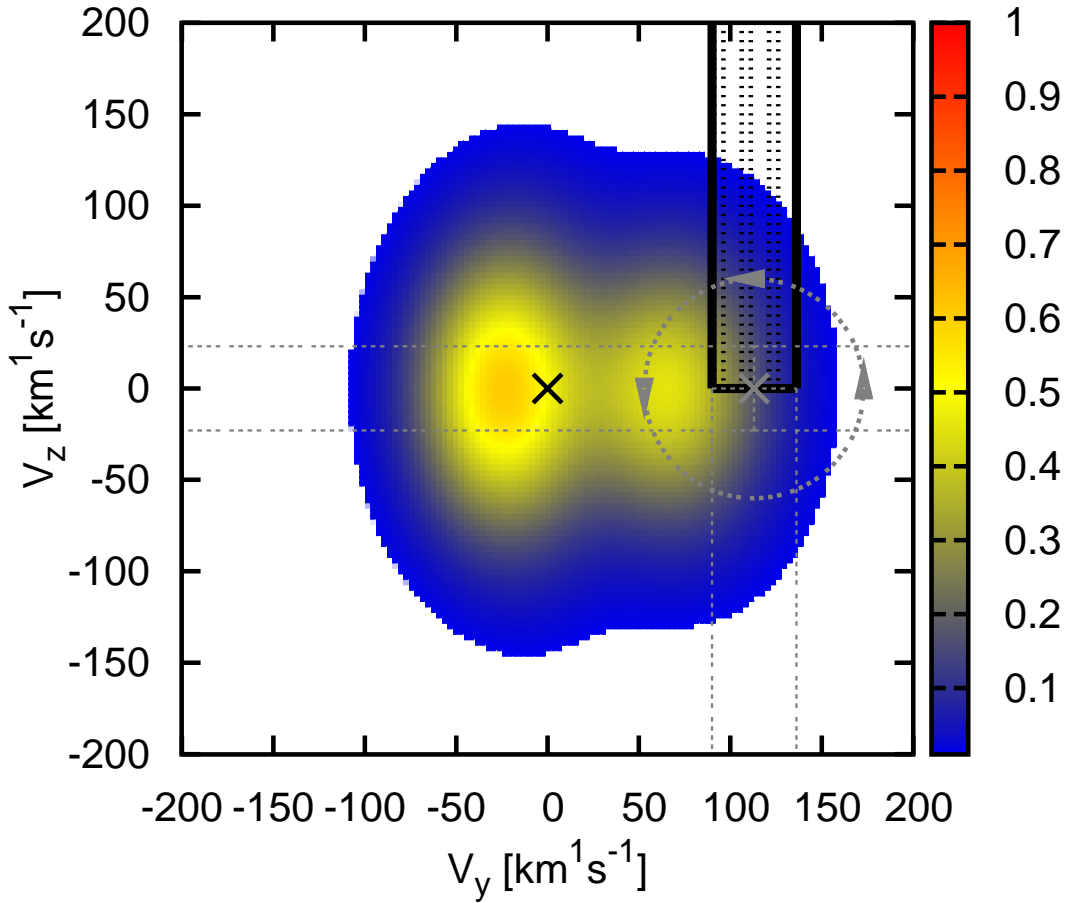


Figure 5.7: A 2D Y-Z projection of the spherical segment that is indicated by the red line in figure 5.6 is shown. The parameters of the velocity distribution as the colour code are the same as in figure 5.6. The filled black box marks the acceptance of the collimator. The rotation of the spacecraft is indicated by the grey circle and boxes. The black and grey crosses mark the intersection of the X-axis of SEE and SC coordinates.

The parameters are :

1. m, q : Defines the ion species
2. E/q : The deflection voltage. Together with m/q the velocity that defines the spherical segment and the efficiencies are defined.
3. $\alpha_{EP}, \alpha_{\perp EP}$: Two angles that give the orientation of the spacecraft spin-axis in, and out of the Ecliptic respectively. Together with $v(E/q, m/q)$ they define the tracing point of the collimator and are needed for coordinate transformation.

4. $\beta_{EP}, \beta_{\perp EP}$: Two angles that give the orientation of the magnetic field vector in, and out of the Ecliptic respectively. They define the axis of symmetry of the velocity distribution and are needed for coordinate transformation.
5. v_{Core} : The velocity that defines the position of the origin of MF coordinates in SEE coordinates. It also defines the position of the centre of the core of the VDF
6. v_{Beam} : The drift velocity of the Beam in respect to the Bulk in MF coordinates.
7. $vth_{\perp}, vth_{\parallel}$: The two velocities that define the thermal widths of the distribution parallel, and perpendicular to the magnetic field in MF coordinates.
8. A_{Core}, A_{Beam} : The values that scale the intensity of the Core, and the Beam respectively.

For purposes of clarity, we will denote the VDF specific parameters $v_{Core}, v_{Beam}, vth_{\perp}, vth_{\parallel}$, A_{Core} , and A_{Beam} as \vec{p} . $\alpha_{EP}, \alpha_{\perp EP}$ and $\beta_{EP}, \beta_{\perp EP}$, are summarised as $\vec{\alpha}$, and as $\vec{\beta}$ respectively. As before, the ion specific parameters and the deflection step are denoted by the indices i and s , respectively. Thus we get from equation 3.29,

$$N_{si}(\vec{\alpha}, \vec{\beta}, \vec{p}) = v_{si}\tau g \Delta v_{si} D_{adv, si}(\vec{\alpha}, \rho_{si}(\vec{\beta}, \vec{p})) \int_{|\vec{v}|=v_{si}} \rho_{si}(\vec{v}, \vec{\beta}, \vec{p}) d\vec{v}. \quad (5.6)$$

Using the above equation, we are able to calculate virtual spectra. Figures 5.8 and 5.9 illustrate the influence of $\vec{\beta}$ on the virtual spectra, while $\vec{\alpha}$ and \vec{p} are held constant. The thermal anisotropy is $T_{\perp}/T_{\parallel} = 2$, the ratio $A_{Core}/A_{Beam} = 2$, and $\alpha_{EP} = 5^{\circ}$. The VDF in the Ecliptic Plane is shown together with the virtual spectrum. The spectra are 1D projections of the 3D VDFs. One can see that the shape of the spectra strongly depends on β_{EP} . A comparison of the cases $\beta_{EP} = 30^{\circ}$ and $\beta_{EP} = -30^{\circ}$ makes clear the influence of α_{EP} . In the first case the beam is even more pronounced than the core. In the second case the beam is mostly hidden by the slope of the core. This can be understood by the fact that in the first case, the rotation axis lies close to the centre of the beam and thus the collimator covers a great fraction of the distribution all the time. In contrast, in the second case, the centre of the beam lies far away from the rotation axis, so that the mean coverage of the distribution is much smaller. From a comparison of the cases $\beta_{EP} = 0^{\circ}$ and $\beta_{EP} = 180^{\circ}$ it can be clearly seen that the count rates are biased towards higher velocities. One reason for this is the instrumental efficiency that generally increases towards higher velocities. Another reason is the acceptance of the collimator. It is given by a fixed solid angle, thus, the covered area increases with v^2 . This bias causes the general

5 Velocity Distribution Functions

trend that the centre of mass of the 1D VDFs is shifted towards higher v_x related to the 3D VDFs.

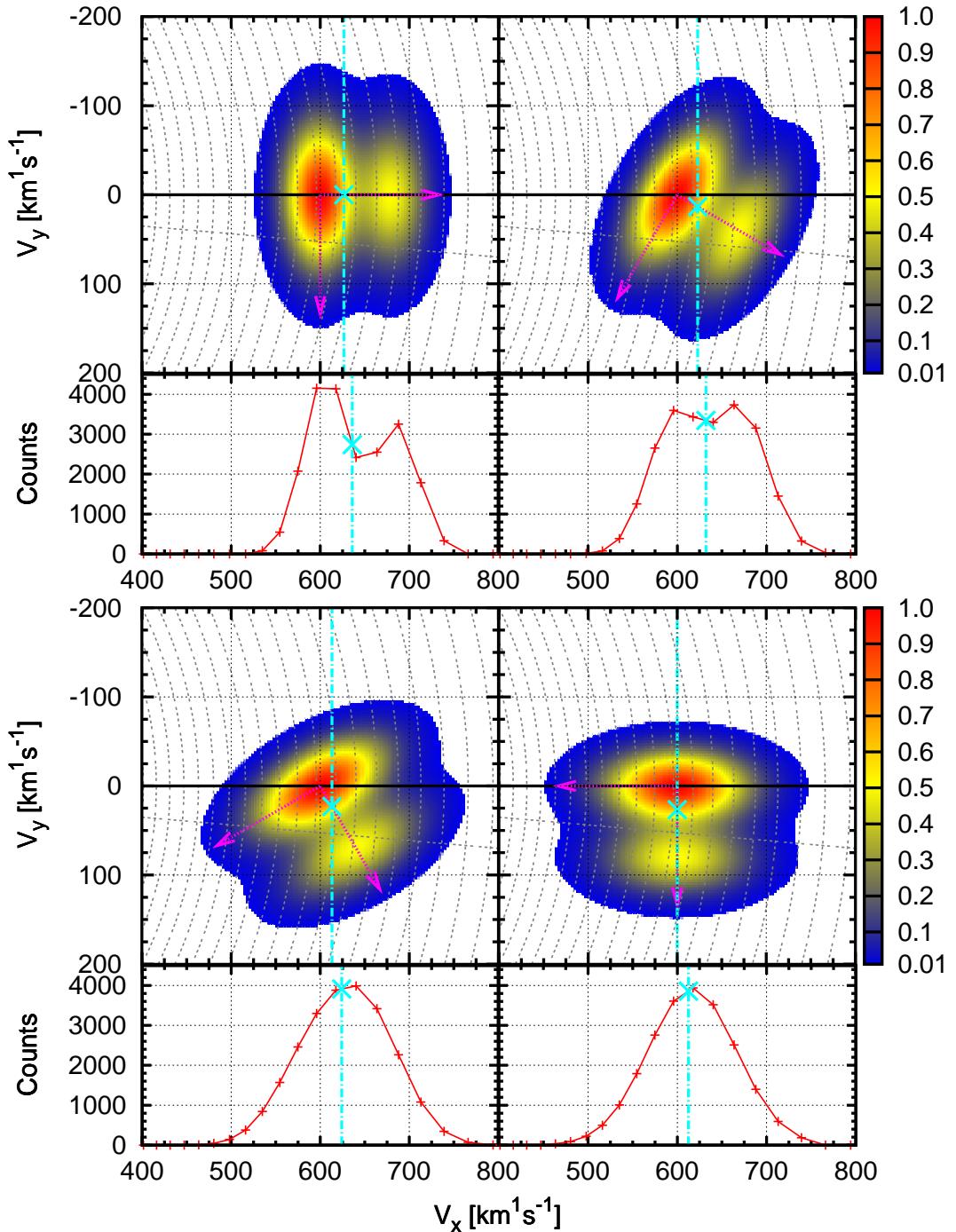


Figure 5.8: The influence of the orientation of the magnetic field on the shape of the virtual spectrum is shown. The 2D cuts through velocity phase space are arranged as in figure 5.6. The same parameters for the VDF have been used. In the panels beneath the 2D plots, the corresponding 1D virtual spectra are shown. The vertical light blue lines illustrate the shift between the centres of mass of the 2D distribution and its 1D projection. From upper left to lower right the angle between SEE and MF coordinates are 0° , 30° , 60° , and 90° .

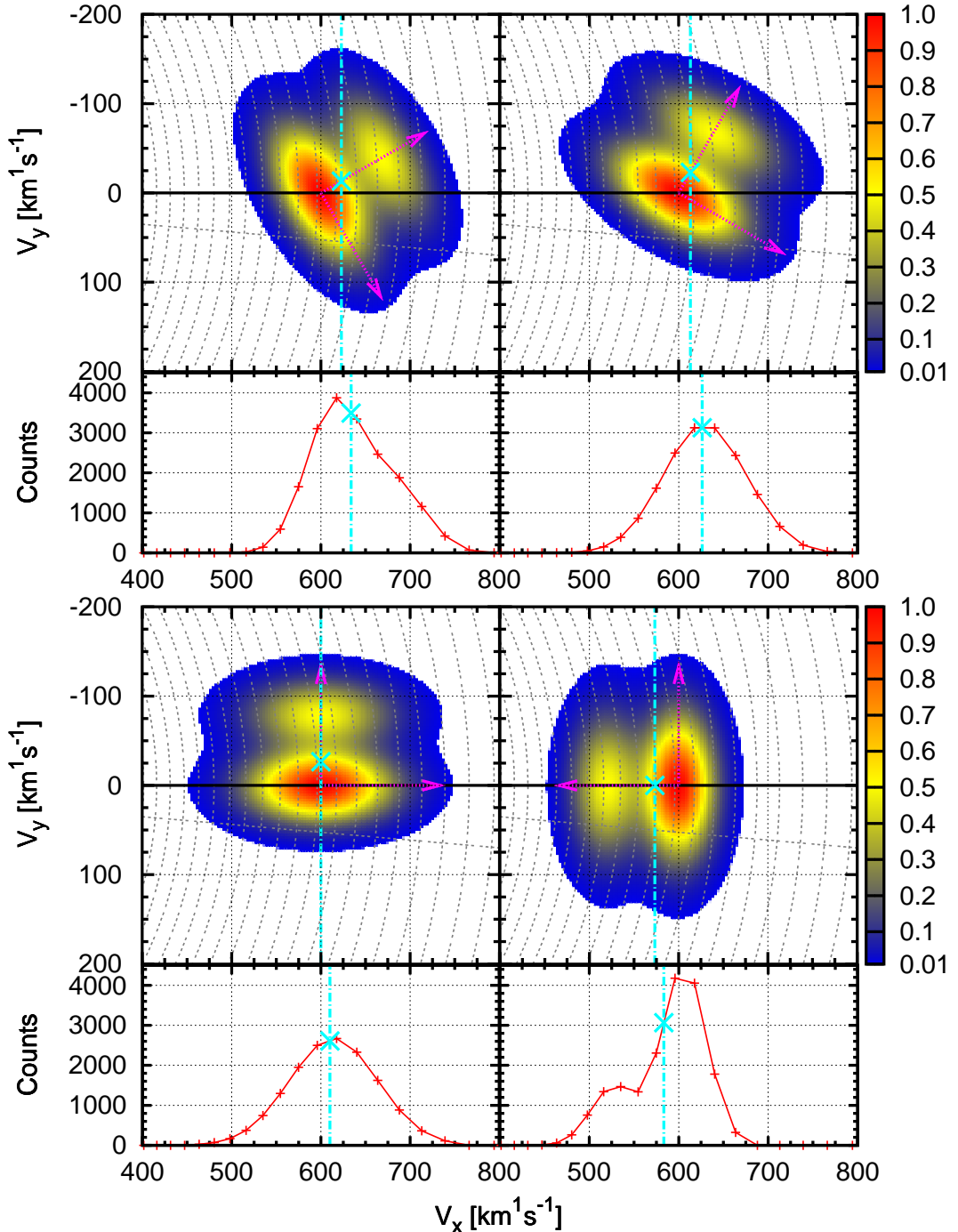


Figure 5.9: The arrangement of the plot is as in figure 5.8. From upper left to lower right the angle between SEE and MF coordinates are -30° , -60° , -90° , and 180° .

6 Differential Streaming and Temperature

In the previous chapter a model for the VDFs of solar wind ions and a virtual detector has been presented. By applying the virtual detector to model VDFs, virtual spectra can be derived. Here, we will investigate the significance of our model VDFs. From the model some general consequences for the interpretation of observations arise, they are outlined in section 6.1. A survey of the data that has been used for our studies is given in 6.2. In section 6.3 it is shown that the virtual spectra can reproduce the observations. Unfortunately the facts that the virtual spectra depend on many parameters and deserve great computing time, complicate a general application in data analysis. However, even if we are not able to determine the parameters of the model VDFs for longer time series of individual sets of data, we can make some assumptions that allow a statistical approach to interpret averaged features of observations. These features are a strong dependence of the observed differential streaming, Δv , on the magnetic field direction, $\vec{\beta}$, and if any a weak dependence of the observed temperatures on $\vec{\beta}$. The strong dependence of Δv on $\vec{\beta}$ that is also predicted by the model (s. section 6.1) is illustrated in section 6.4. The assumptions we have made and the statistical studies are presented in section 6.5. Finally, the question for the influence of wave-particle interaction is addressed in section 6.6.

Due to the strong dependency on the magnetic field direction it is obvious that the application of the model is bound to time frames of constant $\vec{\beta}$. If ever this condition is normally fulfilled only for highest time resolutions.

6.1 Interpretation of Observations

We have seen in the previous chapter that if all other parameters of the model are held fixed the virtual spectra depend critically on $\vec{\beta}$, as is shown in Figures 5.8 and 5.9. Figure 6.1 shows an example for $\beta_{EP} = 0^\circ$ (left) and $\beta_{EP} = 90^\circ$ (right) how the moments of the virtual spectra depend on $\vec{\beta}$ and the ratio of the intensities A_{Beam}/A_{Core} . The upper two panels show Ecliptic Plane cuts through the 3D distributions. In the upper panel

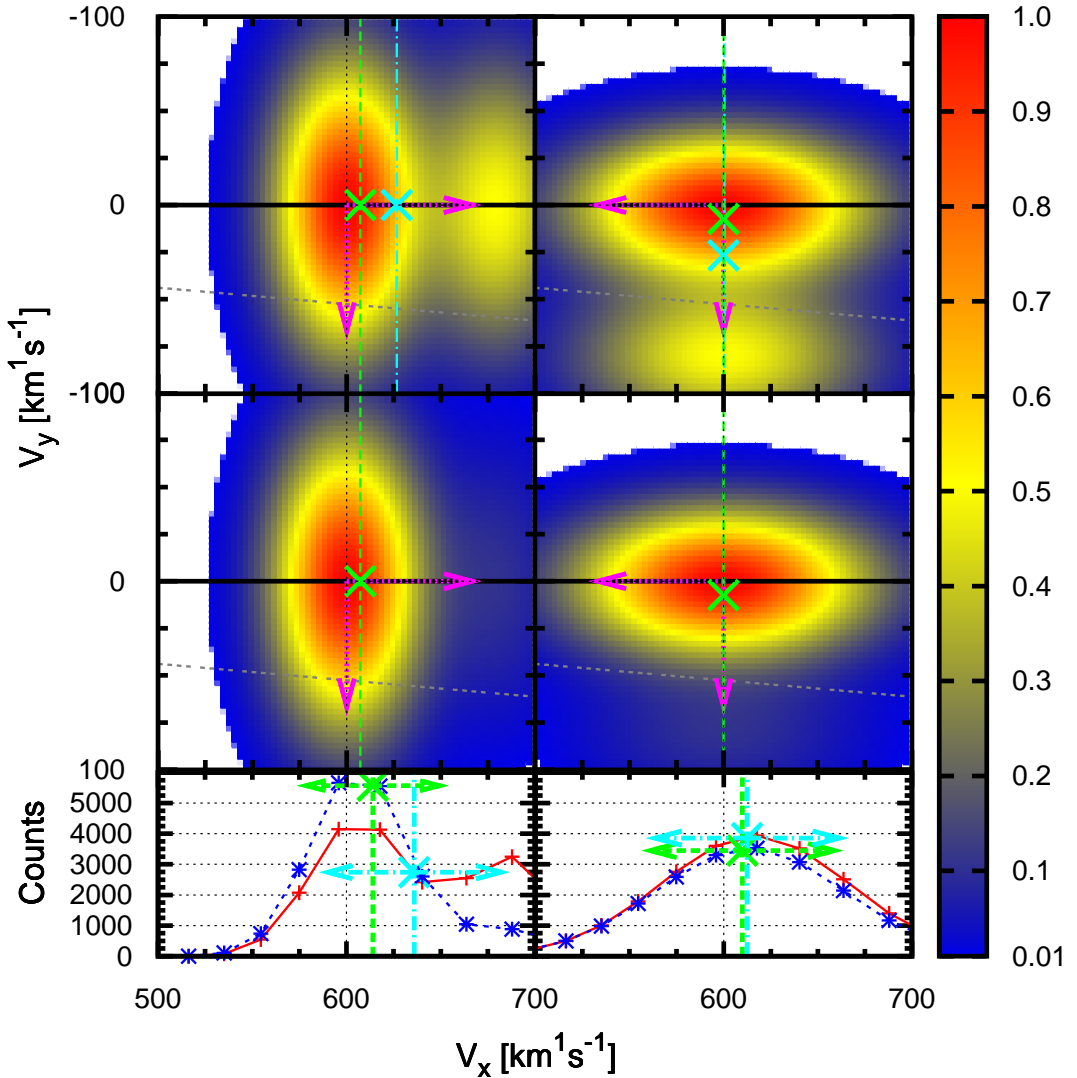


Figure 6.1: The dependency of the differential streaming on the direction of the magnetic field is illustrated (left $\beta_{EP} = 0^\circ$, right $\beta_{EP} = 90^\circ$). The plot is arranged as in figure 5.8. The additional panel in the middle shows a second velocity distribution with the same set of parameters except for a dilute beam $A_{Beam}/A_{Core} = 0.1$, that is hardly visible ($A_{Beam}/A_{Core} = 0.5$ in the upper panel). In the bottom panel the virtual spectra for the upper (red) and the middle (dashed blue) distributions are shown. The centre of mass of the VDF with the pronounced beam is marked by the light blue crosses. The green crosses mark the case of the dilute beam. The arrows in the bottom panel indicate the thermal velocities of the virtual spectra.

$A_{Beam}/A_{Core} = 0.5$, in the central panel $A_{Beam}/A_{Core} = 0.1$. The thermal widths as well as the positions of core and beam are held fixed. In the bottom panel, the corresponding virtual spectra are plotted (red=upper, blue=central). The light blue (upper) and green

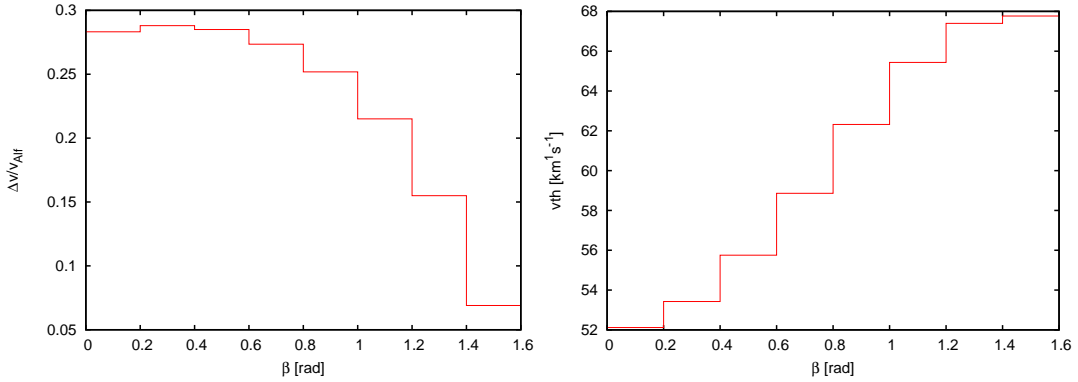


Figure 6.2: The distribution of the differential streaming (left) and the temperature (right) depending on the direction of the magnetic field is shown. For the calculation the same distributions as in figure

(central) crosses mark the positions of the centre of masses of the 3D distributions, and the virtual spectra respectively. The vertical lines mark the length of the corresponding position vectors $|\vec{v}_{com}| = v_{sw}$, they give us the absolute velocities in the frame of the virtual spectra. The widths of the virtual spectra that are proportional to \sqrt{T} are indicated by the coloured arrows in the bottom panel.

In the case $\beta_{EP} = 90^\circ$, the widths of the 1D spectra are $v_{th_{red}} = 48.9 \text{ km s}^{-1}$ and $v_{th_{blue}} = 49.0 \text{ km s}^{-1}$, they nearly match $v_{th_\perp} = 50.0 \text{ km s}^{-1}$ of the 3D model VDFs. The speeds of the centre of masses are $v_{red} = 612.5 \text{ km s}^{-1}$, and $v_{blue} = 609.9 \text{ km s}^{-1}$ nearly equal each other while they are shifted towards the corresponding $|\vec{v}_{com}^{red}| = 600.6 \text{ km s}^{-1}$, and $|\vec{v}_{com}^{blue}| = 600.0 \text{ km s}^{-1}$ respectively. This shift is due to instrumental properties as has been discussed in section 5.2.

The results are different in the case $\beta_{EP} = 0^\circ$. The widths of the 1D spectra are $v_{th_{red}} = 46.0 \text{ km s}^{-1}$ and $v_{th_{blue}} = 35.3 \text{ km s}^{-1}$, they are in between $v_{th_\parallel} = 25.0 \text{ km s}^{-1}$ and $v_{th_\perp} = 50.0 \text{ km s}^{-1}$ of the 3D model VDFs. The speeds of the centre of masses are $v_{red} = 636.0 \text{ km s}^{-1}$, and $v_{blue} = 614.0 \text{ km s}^{-1}$ again they are shifted towards the corresponding $|\vec{v}_{com}^{red}| = 626.6 \text{ km s}^{-1}$, and $|\vec{v}_{com}^{blue}| = 607.3 \text{ km s}^{-1}$ respectively.

Though the actual parameters of the VDFs may vary strongly and thus also the moments of the observations, the following conclusions drawn from the example above hold true in general. For magnetic field directions that are approximately perpendicular to the Sun-Earth line, SWICS measures $T \approx T_\perp$ and $v_{sw} \approx v_{core}$ with a certain shift caused by the instrument. The influence of A_{Beam}/A_{Core} on T and v_{sw} is very small. From the example we get $\Delta v_{th} = |v_{th_{red}} - v_{th_{blue}}| = 0.1 \text{ km s}^{-1}$, and $\Delta v_{sw} = |v_{red} - v_{blue}| = 2.6 \text{ km s}^{-1}$

6 Differential Streaming and Temperature

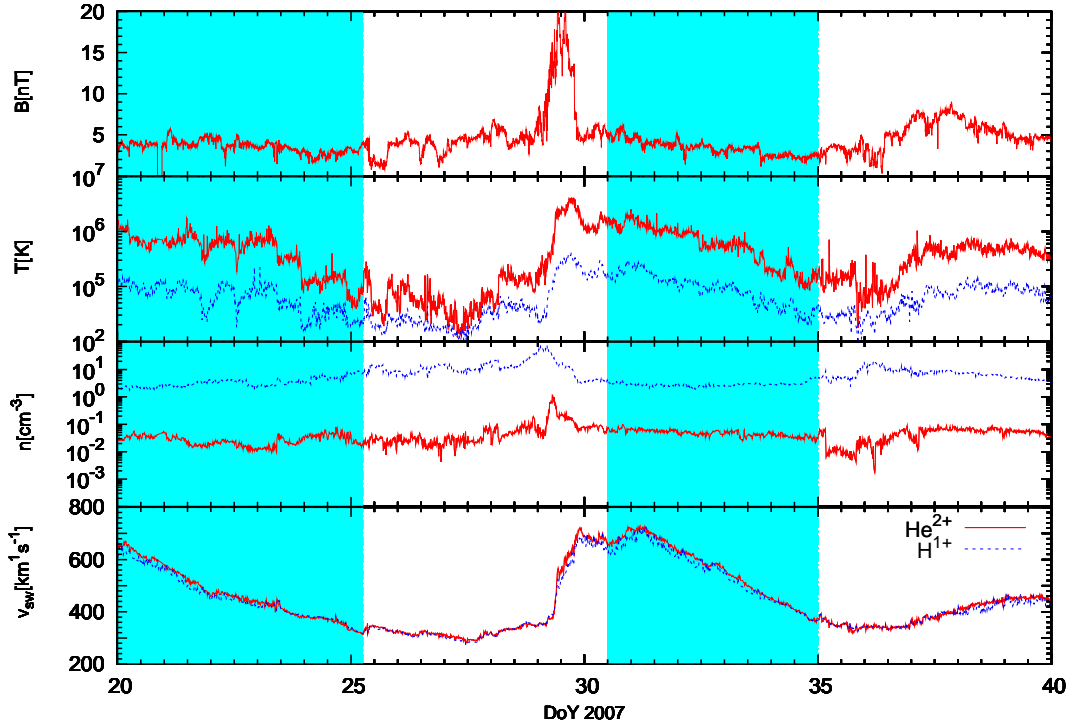


Figure 6.3: A time series of the plasma parameters that have been used for our selection of quiet time solar wind is shown. From bottom to top the speed, density, and temperature of H^{1+} and He^{2+} and the magnetic field strength are shown. Selected time frames are highlighted blue.

respectively. If the magnetic field direction is approximately parallel to Sun-Earth line we would get in the case that no beams are present, $T \approx T_{\parallel}$ and $v_{sw} \approx v_{core}$. With the presence of beams we would get a velocity together with a temperature that provide information about the intensity and the position of the beams. From the example we get $\Delta v_{th} = |v_{th,red} - v_{th,blue}| = 10.7 \text{ km}^1 \text{s}^{-1}$, and a differential streaming $\Delta v_{sw} = |v_{red} - v_{blue}| = 22.0 \text{ km}^1 \text{s}^{-1}$ respectively. For the fainter beam the width is closer to the initial $v_{th,\parallel} = 25.0 \text{ km}^1 \text{s}^{-1}$. The difference in the beam intensities manifest itself as a drift velocity which would be interpreted as differential streaming.

If the magnetic field direction lies between the two extreme values that have been discussed the differential streaming will get smaller with larger angles, while the width will tend towards $v_{th,\perp} = 2v_{th,\parallel}$. Figure 6.2 illustrates this behaviour.

from	-	to	from	-	to	from	-	to
4.00	-	9.00	60.00	-	63.00	103.00	-	107.00
17.40	-	25.25	65.50	-	70.00	119.00	-	126.50
30.50	-	35.00	73.25	-	80.50	129.00	-	135.00
45.50	-	55.00	93.00	-	97.50	145.25	-	151.10

Table 6.1: Selected time frames of quiet time solar wind are listed (DoY).

6.2 Data

Solar activity minimum in 2007 makes it an ideal year to study the solar wind under quiet time conditions. Due to the high computational effort DoY 1 to 152 of SWICS data have been analysed in 12 minutes and 1 hour resolution using our maximum likelihood analysis technique (s. chapter 4). Proton data is crucial to our studies, to calculate required plasma parameters and to derive differential streaming and heating rates. Unfortunately H^{1+} is not fully covered in SWICS PHA data and consequently not included in our SWICS analysis. Hence, it has been taken from a combined SWEPPAM/SWICS database from the ACE Science Center¹. The sometimes large gaps in the SWEPPAM data have been filled by SWICS auxiliary channel data. Additionally MAG data from the ACE Science Center is used.

The only deviation from quiet time condition should come from Corotating Interaction Regions (CIRs). The term Quiet Time Solar Wind (QTSW) refers to solar wind originating from the inactive sun, but there is no general definition based on actual plasma parameters. Thus it is not possible to select periods of QTSW automatically. Consequently we have made a selection by eye, considering the speed, density and temperature of H^{1+} , and He^{2+} , and the magnetic field strength. Periods showing abnormal signatures like increased or strongly fluctuating magnetic field strength, or discontinuities indicated by rapid changes in the parameters of H^{1+} , and He^{2+} were rejected. Figure 6.3 shows the considered parameters and the selected time frames from the first thirty days of year 2007. All selected periods are given in table 6.1.

¹www.srl.caltech.edu/ACE/ASC/

6 Differential Streaming and Temperature

DoY	ion	v_{core}	v_{drift}	vth_{\perp}	vth_{\parallel}	n	A_{Beam}/A_{Core}	β_{EP}	$\beta_{EP\perp}$	v_{Alf}	v_{com}
30.77	H ¹⁺	670	300	43	27	$1.1 \cdot 10^0$	0.18	0.68	1.42	71	679
	He ²⁺	670	300	40	20	$6.4 \cdot 10^{-2}$	0.70				684
	O ⁶⁺	670	300	40	16	$3.7 \cdot 10^{-4}$	0.45				680
120.53	H ¹⁺	595	75	40	25	$1.5 \cdot 10^0$	0.23	0.09	0.1	58	615
	He ²⁺	610	60	45	26	$9.3 \cdot 10^{-2}$	0.72				642
	O ⁶⁺	615	50	40	20	$6.3 \cdot 10^{-4}$	1.10				646

Table 6.2: The parameters used for the calculated spectra that are displayed in figure 6.4 are shown. Velocities are in km s^{-1} , angles in rad. The density, n , is in cm^{-3} . v_{com} in the last column is the resulting velocity of the centres of mass.

6.3 Comparison of Virtual and Measured Spectra

The virtual spectra we calculate from our model can be compared with observations. Figure 6.4 shows two examples for 12 minutes observations of H¹⁺, He²⁺ and O⁶⁺ (red symbols). Additionally virtual spectra for the cases of a VDF consisting of a bi-Maxwellian core and beam (blue symbols), as described in the previous chapter, and a symmetric thermalised VDF (magenta lines), as is used in standard data analysis are shown. The parameters that have been used for the calculations are listed in table 6.2. We found them in agreement with the range of observed parameters by *Marsch et al.* [1982b] and *Marsch et al.* [1982a]. The H¹⁺ observations are analysed via a box-rate method from double coincidence PHA data. Because we don't have the needed H¹⁺ efficiencies for the virtual detector, the efficiencies of He²⁺ have been used for the calculations. Thus, the H¹⁺ densities are not realistic, but the shape of the distributions should be represented properly. He²⁺ and O⁶⁺ have been analysed using the maximum likelihood analysis described in chapter 4. It can be clearly seen that the new model VDFs reproduce the observations to a higher degree than the standard VDFs. Especially the features in the centre of the distributions are reproduced better. In the outer slopes both models tend to deviate from the observations towards smaller values. This behaviour is very likely caused by the use of Gaussians, we will shortly refer to this topic in section 7.1.

From the velocities of the centres of mass, v_{com} , we can see that differential streaming in respect to H¹⁺ occurs. For DoY 30.77 the magnetic field is nearly perpendicular to the Sun-Earth line, and we see very small differential streaming. This is in agreement with the predictions we have shown in section 6.1. Also in agreement with the predictions for the case of magnetic field directions that are aligned with the Sun-Earth line the differential

6.3 Comparison of Virtual and Measured Spectra

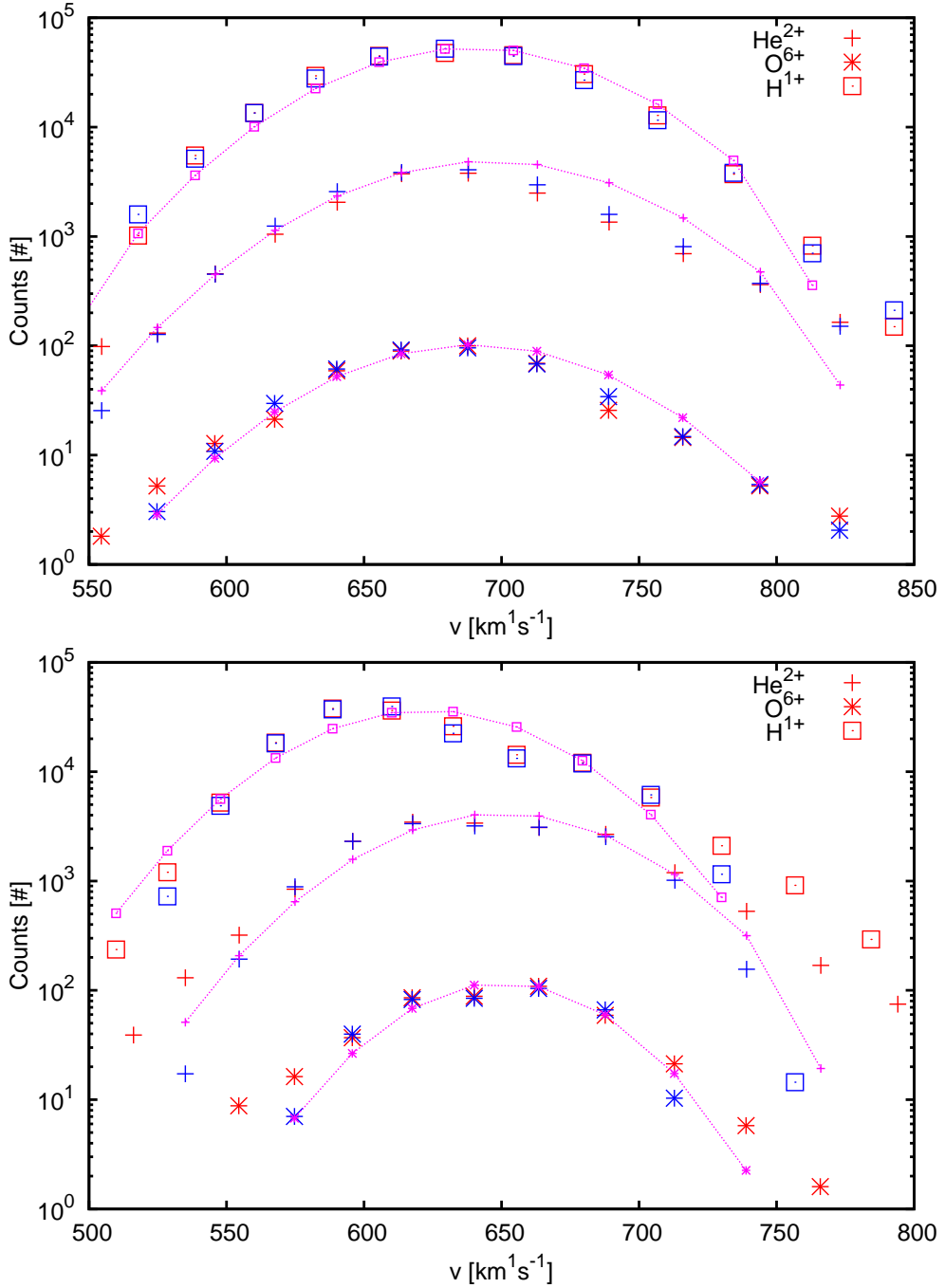


Figure 6.4: Velocity distributions of H^{1+} , He^{2+} , and O^{6+} from DoY 30.77 (upper panel) and 120.77 (lower panel) are shown. Big red symbols mark SWICS measurements. Big blue symbols mark virtual spectra for the case of a core-beam bi-Maxwellian VDF. Magenta small symbols and lines mark virtual spectra for the case of a standard Maxwellian VDF.

6 Differential Streaming and Temperature

streaming at DoY 120.77 is strong. From figure 6.4 and table 6.2 we can see that the differential streaming is composed of two contributions. One contribution is a small drift velocity of the cores of He^{2+} and O^{6+} with respect to H^{1+} . Another contribution is caused by the projection of the beams as discussed in section 6.1. It has also to be mentioned that the thermal velocities and the beam intensities in both cases are similar.

6.4 Observed Differential Streaming

Here, the dependency of the observed differential streaming, Δv , with respect to H^{1+} on the direction of the magnetic field is investigated. For the virtual spectra the two angles β_{EP} and $\beta_{EP\perp}$ are needed, in real data we get them from the magnetic field data. They are needed because of the influence of the spacecraft orientation that is given by α_{EP} and $\alpha_{EP\perp}$. But if we make the assumption that we expect both directions to be stochastically independent, we have only one angle β left that is needed to describe orientation of the magnetic field. It is the angle between the magnetic field vector and the X-axis of SEE coordinates in the plane that is spanned by the vector and the axis. It is essential

$$\beta = \arccos(\cos \beta_{EP} \cos \beta_{EP\perp}). \quad (6.1)$$

Figure 6.5 illustrates how the angles translate into β . Dealing with magnetic field data, often only β_{EP} is used to describe the direction according to the usage of the Parker Angle that describes the expected angle in the Ecliptic Plane that depends on solar wind speed. The stepped curves in the upper panel of figure 6.6 show the differential streaming depending on β , and β_{EP} respectively. At a first look the shape is similar and it is hard to decide on which angle the streaming depends. To emphasise that β is the right angle to use we have compared the two cases where either angle is held fixed while the other may vary. The lower panel illustrates what is meant by this. The lines in the upper panel show the distributions for both cases. On the left β_{EP} has been held constant and it can be clearly seen that the shape depending on β is preserved. In contrast on the right side the lines do not follow the trend of the stepped curves. Thus we conclude that using β_{EP} the trend of Δv is flattened due to mixing of different values of β .

The dependence on β sets stringent limits for the analysis. Within the time resolution of the data β must not vary too strong, as demonstrated in figure 6.7. The results from 12 minutes and 1 hour data are compared. $\Delta\beta$ is the variation of β within the time resolution, it is set to $\Delta\beta = 0.2$ rad for our analysis. It can be seen that in 1 hour time resolution without filtering the trend with β is nearly gone while with filtering the sample

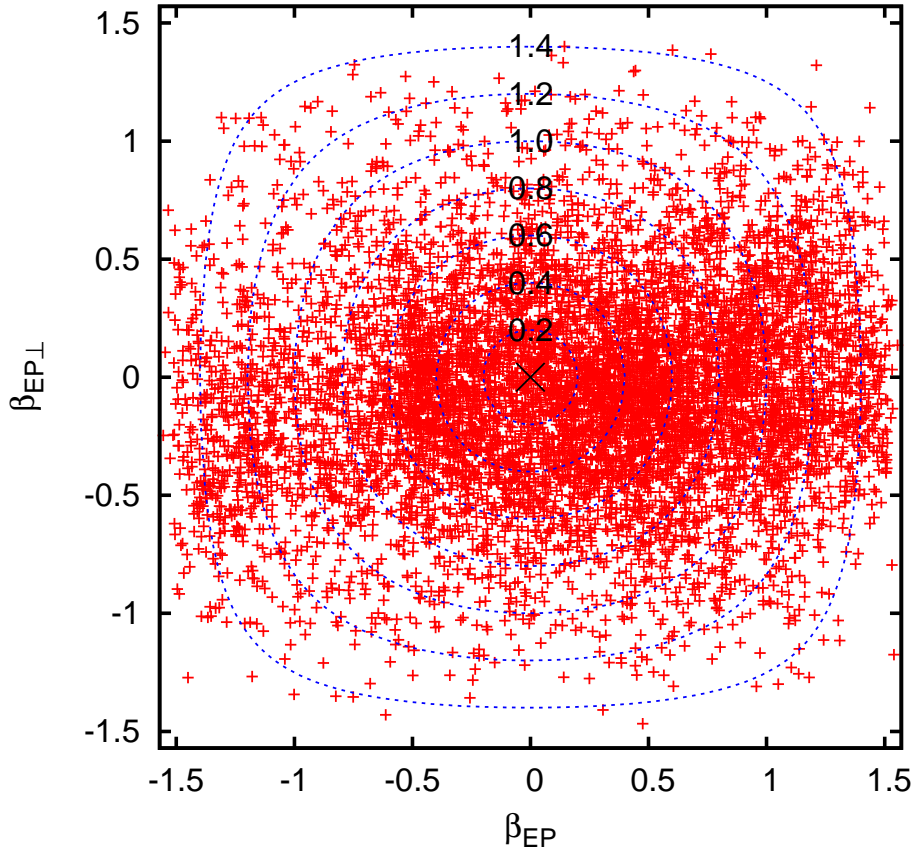


Figure 6.5: The measured magnetic field directions for the time frames given in table 6.1 are displayed. The X- and Y-axis are the in- and out-Ecliptic angles β_{EP} and $\beta_{EP\perp}$. Lines of constant β , the angle between Sun-Earth line and magnetic field direction, are indicated by dashed blue lines.

gets very small so that there are not even results for all values of β . In 12 minute data the trend also flattens if filtering is abandoned. Therefore we have taken 12 minute data, with the requirement that $\Delta\beta < 0.2$ rad., for our studies.

Finally figure 6.8 shows the observed differential streaming of He^{2+} for different solar wind types. It can be seen that it is most pronounced in the fast solar wind. Therefore, we have restricted our studies to the fast solar wind.

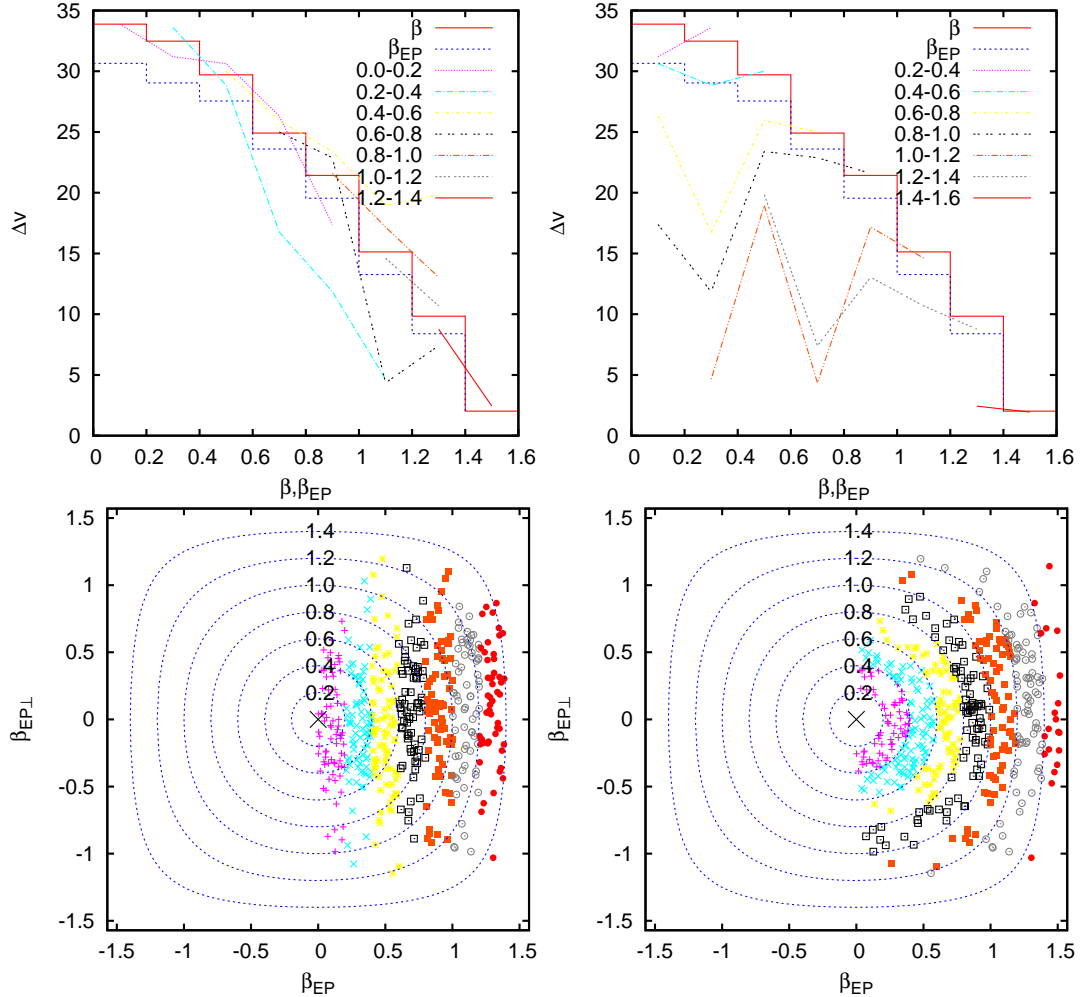


Figure 6.6: In the upper panel the differential streaming Δv between He^{2+} and H^{1+} dependent on β and β_{EP} is shown (stepped curves). In the lower panel the magnetic field directions of the data sample are shown, the arrangement is the same as in figure 6.5. The coloured lines in the upper panel show the dependency of Δv on β (left) and β_{EP} (right) if the other angle is held fixed. The corresponding data samples are indicated by the colour of the points in the lower panel.

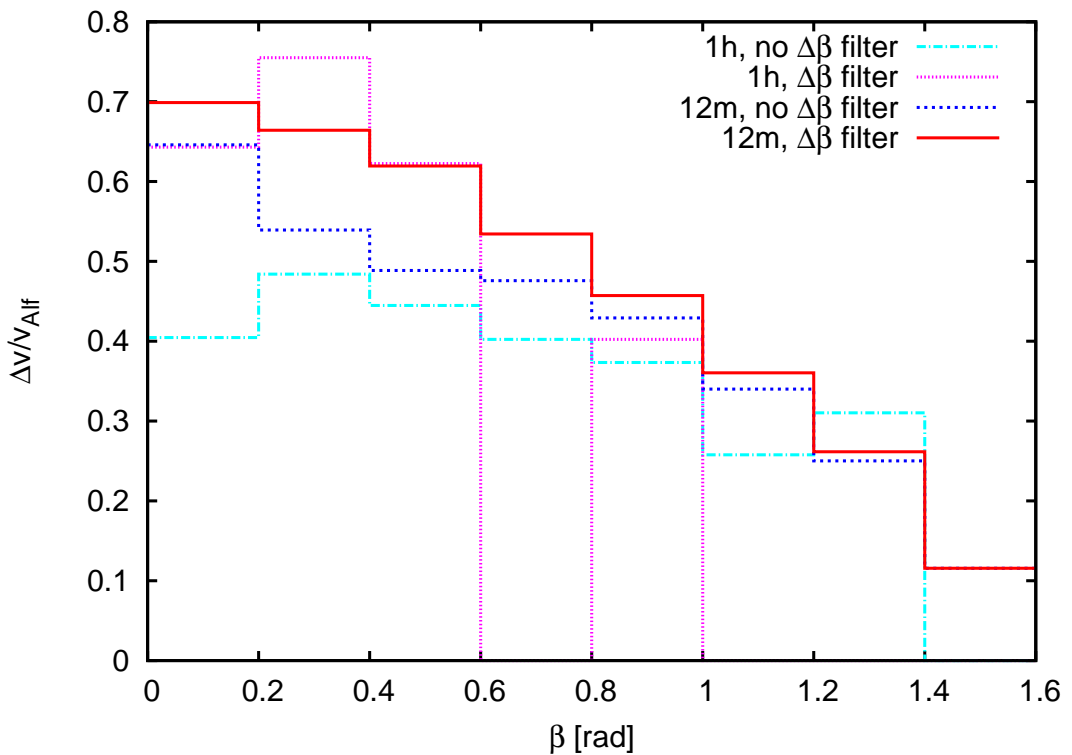


Figure 6.7: The mean ratio differential streaming of He^{2+} to Alfvén speed is plotted versus the direction of the magnetic field β . 12 minute and 1 hour data with and without a filter for $\Delta\beta$ is shown.

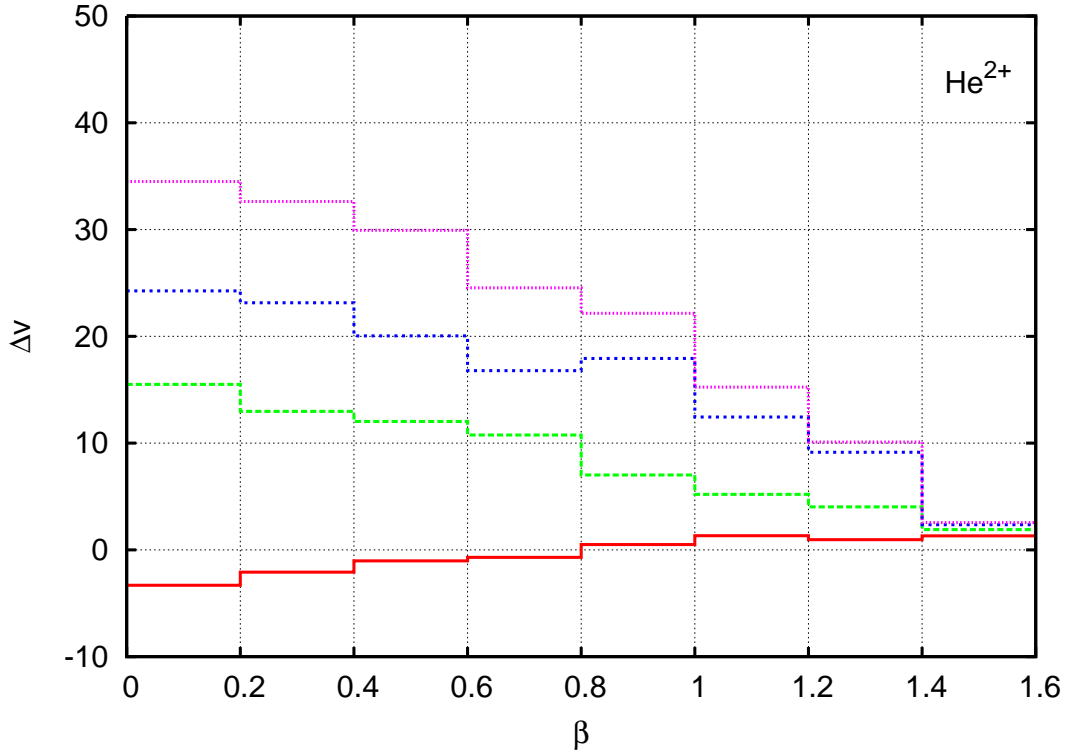


Figure 6.8: The dependency of observed differential streaming of He^{2+} for different solar wind speeds is shown. Red : $300\text{km s}^{-1} < v_{\text{sw}} < 400\text{km s}^{-1}$. Green : $400\text{km s}^{-1} < v_{\text{sw}} < 500\text{km s}^{-1}$. Blue : $500\text{km s}^{-1} < v_{\text{sw}} < 600\text{km s}^{-1}$. Magenta : $600\text{km s}^{-1} < v_{\text{sw}} < 700\text{km s}^{-1}$.

6.5 Statistical Analysis of Differential Streaming and Temperature

As pointed out in the previous sections, the observability of the features of the VDFs depend strongly on β . If we want to compare the results from our virtual detector with averaged results from observations some assumptions have to be made. Beside β , the virtual spectra depend on several parameters that might also vary strongly in time. But if we assume that they are stochastically independent of β , long-term averaged results from observations should be comparable with simulations using mean values as parameters. The data sample has been ordered by β in 0.2 deg intervals. For each interval the mean values of β , $\vec{\alpha}$, $v_{H^{1+}}$, and v_{Alf} have been determined. The mean values have been taken as parameters for the calculation of the theoretical differential streaming and thermal velocity. Where v_{core} has been set to the mean value of $v_{H^{1+}}$. For v_{drift} a fixed fraction, f_{drift} of the mean value of v_{Alf} has been taken. Making the assumption that vth_{\perp} and vth_{\parallel} of the core and the beam and the ratio A_{Beam}/A_{Core} are stochastically independent of β they have been held fixed for all intervals.

Concluding we have four free parameters vth_{\parallel} , vth_{\perp} , f_{drift} , and A_{Beam}/A_{Core} left to adjust the calculated distributions to the observations. From our analysis we found the observed distributions can be represented by the model calculations. Two examples for He²⁺ and O⁶⁺ are shown in figures 6.9 and 6.10. The used parameters for He²⁺ are $vth_{\parallel} = 34 \text{ km}^1 \text{s}^{-1}$, $vth_{\perp} = 45 \text{ km}^1 \text{s}^{-1}$, $f_{drift} = 1.3$, and $A_{Beam}/A_{Core} = 1.0$. For O⁶⁺ the used parameters are $vth_{\parallel} = 29 \text{ km}^1 \text{s}^{-1}$, $vth_{\perp} = 40 \text{ km}^1 \text{s}^{-1}$, $f_{drift} = 1.2$, and $A_{Beam}/A_{Core} = 0.65$. But we also found that the choice of vth_{\parallel} , vth_{\perp} , f_{drift} , and A_{Beam}/A_{Core} is not unique.

However, all results that have been presented in the sections 6.1-6.5 show that our model is capable to explain the non-thermal features that are ubiquitous in the observations of heavy ions in the solar wind.

6 Differential Streaming and Temperature

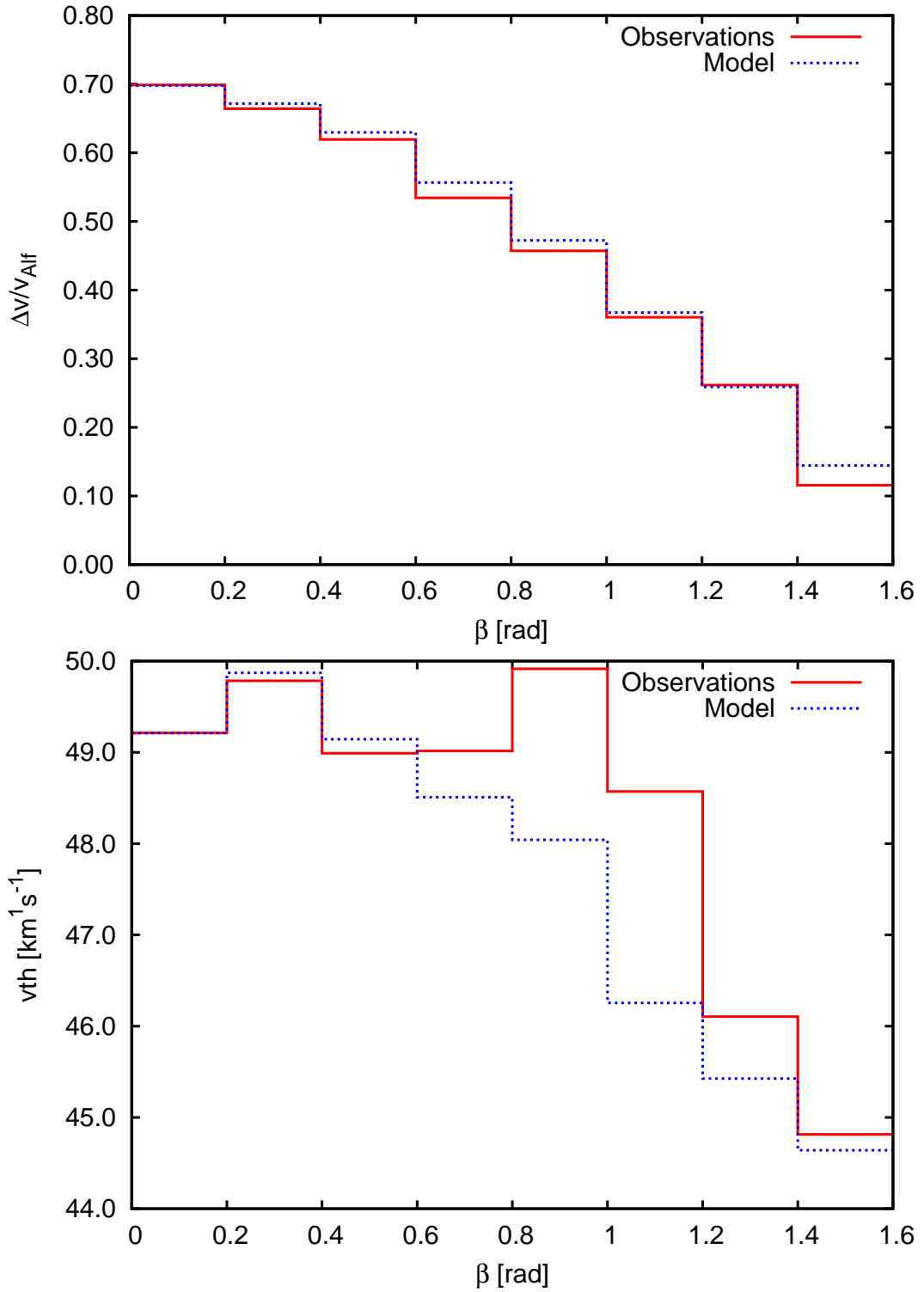


Figure 6.9: Upper panel : The observed differential streaming of He^{2+} together with model calculations are shown.

Lower panel : The observed thermal velocities of He^{2+} together with model calculations are shown.

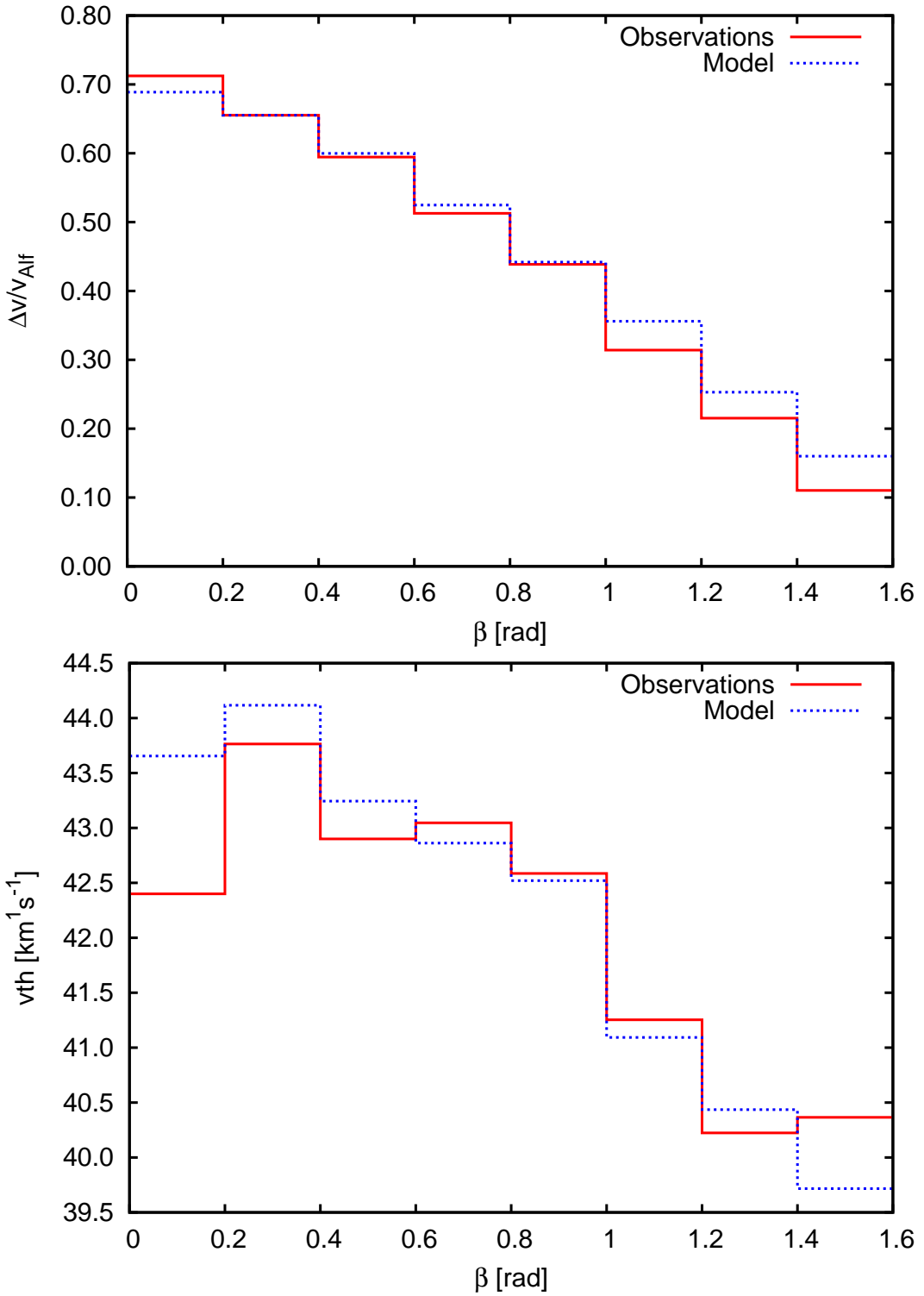


Figure 6.10: Upper panel : The observed differential streaming of O^{6+} together with model calculations are shown.

Lower panel : The observed thermal velocities of O^{6+} together with model calculations are shown.

6.6 Wave particle interaction / Turbulent heating

In chapter 5 we mentioned that recent theories claim wave-particle interaction is the most likely candidate to explain the kinetic properties of solar wind H¹⁺ and He²⁺. The studies described in the previous section strongly indicate that the VDFs of heavy ions show the same features and, thus, are very likely shaped by the same mechanism(s). Therefore we have looked for signatures of resonant wave-particle interaction in the observations. In general wave-particle interaction is a wide field of studies and simulations are complicated, see e.g. *Heuer and Marsch* [2007] and *Araneda et al.* [2008]. For this work we have set up a simple model which simulates the influence of ion cyclotron resonance. In the following we will briefly describe the concept of resonant wave-particle interaction. Particles can interact with waves if the resonance condition

$$\omega_{k\parallel} - k_{\parallel}v_{\parallel} = n\Omega_c \quad (6.2)$$

is fulfilled *Tsurutani and Lakhina* [1997]. k_{\parallel} , and $\omega_{k\parallel}$ are the wave vector, and the frequency of the wave respectively. Ω_c is the gyro frequency of the particle. With the particles charge q and mass m and the magnetic field strength B , it is given by

$$\Omega_c = \frac{qB}{m}. \quad (6.3)$$

The natural number n on the right side of equation 6.2 tells us that resonance can occur for multiples of the gyro frequency. The cases $n = 0$ and $n = 1$ are briefly explained in the following, for they are principally capable of generating differential streaming, and heating perpendicular to the magnetic field.

The first case of $n = 0$ is called Landau resonance. Particles that are slightly below the resonance frequency on average gain energy while particles that are slightly above the resonance frequency on average loose energy. If there are more particles below than above resonance, on average power is drained from the wave, thus, accelerating the centre of mass. In the opposite case power is transferred from the particles to the wave, decelerating the centre of mass. Equation 6.2 in this case is independent of Ω_c and thus is a possible candidate for the formation of beams.

The case $n = 1$ is called ion cyclotron resonance. In the rest frame co-moving with gyro centre of the particle it gyrates with the same frequency as the electric field vector of the wave. In the ideal case the particle is accelerated until its gyro radius exceeds the spatial scale of the wave. The gyro radius is given by

$$\rho_c = \frac{mv_{\perp}}{qB}. \quad (6.4)$$

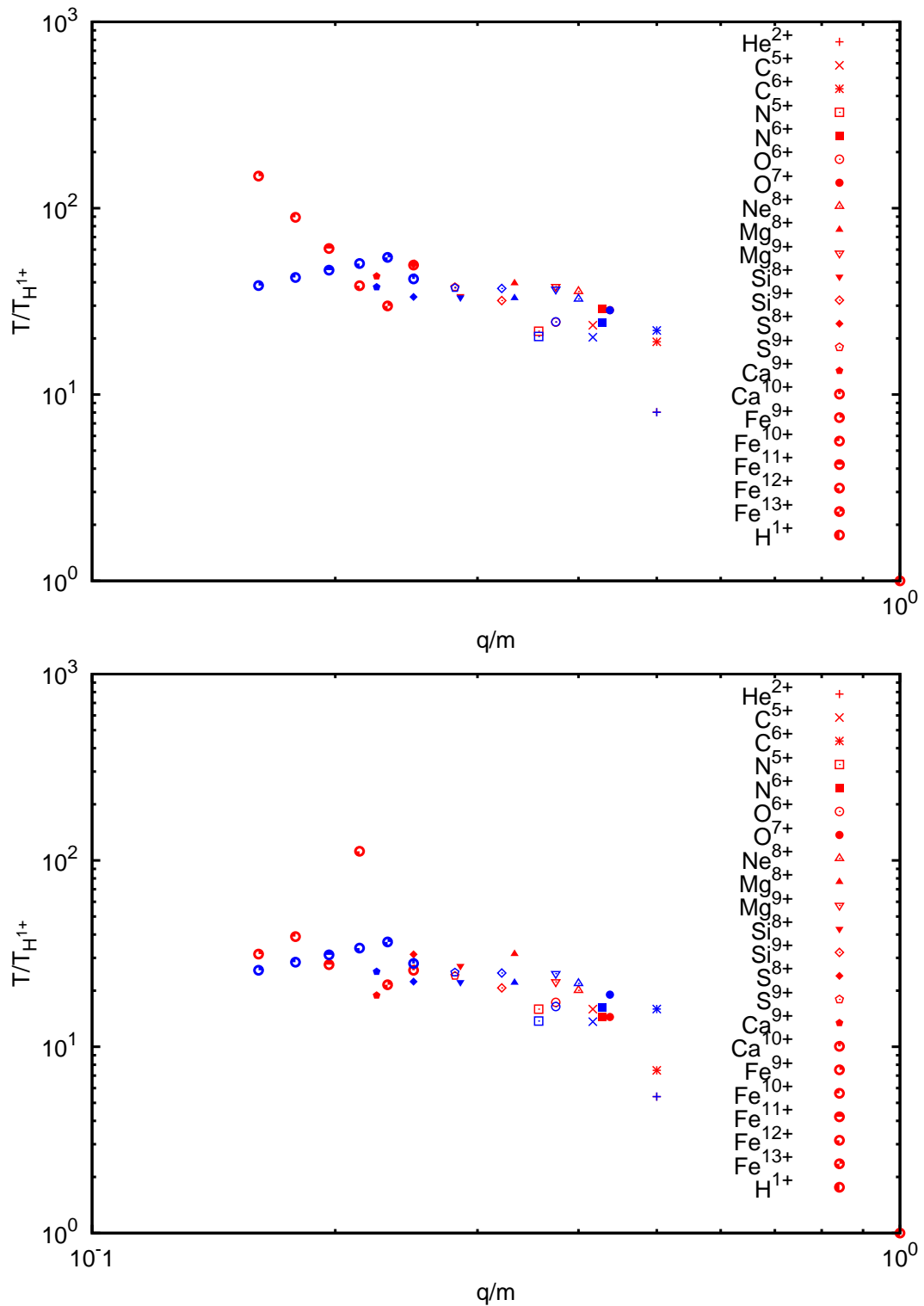


Figure 6.11: The relative heating rates $T/T_{H^{1+}}$ of several ions are shown for fast (upper panel) and slow (lower panel) solar wind. Red symbols mark measured rates. Theoretical rates are indicated by blue symbols.

6 Differential Streaming and Temperature

The energy of a particle that drops out of resonance because its gyro radius has reached the scale of the wave is given by

$$E = \frac{m}{2} v_{\perp}^2. \quad (6.5)$$

Taking equations 6.4 and 6.5 together, we get

$$E = \frac{B \rho_{\omega} q^2}{2} \frac{q^2}{m}. \quad (6.6)$$

Using the relation between frequency and wave vector

$$k = \frac{\omega}{v_{wave}} \quad (6.7)$$

with $v_{wave} = v_{Alf}$ for Alfvén waves and the velocity of the particle equal to the solar wind speed v_{sw} , equations 6.2 and 6.3 give us the resonance frequency for a given ion by

$$\omega = \frac{qB}{m} \left(1 - \frac{v_{sw}}{v_{Alf}} \right)^{-1}. \quad (6.8)$$

Now we assume that wave power cascades down from low to high frequencies, and from large to small spatial scales in the form

$$P(\omega) = P_0 \omega^{-\gamma} \quad (6.9)$$

with the spectral index γ . Furthermore we assume a spatial scale, $\rho(\omega)$,

$$\rho(\omega) = c_{scale} P(\omega), \quad (6.10)$$

whit a scaling factor c_{scale} . The energy of an ion that drops out of resonance with this assumptions becomes

$$E = c P(\omega) \frac{q^2}{m} \quad (6.11)$$

where c is a scaling factor that is except for a factor $\frac{B}{2} c_{scale}$ from equation 6.10. With the number density $n(q, m)$ the total amount of energy that is drained from the wave by an ion species is

$$\Delta P = c P(\omega) \frac{q^2}{m} n(q, m). \quad (6.12)$$

If we consider equation 6.8 the total drain at a given ω can be written as

$$\Delta P(\omega) = c P(\omega) \sum_{ions \frac{q}{m}(\omega)} \frac{q^2}{m} n(q, m). \quad (6.13)$$

With the assumption that the wave power spectrum arises from a turbulent cascade, which means that wave power is transferred from low to high frequencies via turbulence,

we can finally write equation 6.9 as

$$P(\omega) = P_0 \omega^{-\gamma} - \sum_{\omega' < \omega} \Delta P(\omega'). \quad (6.14)$$

This means that wave power that has been drained from the cascade at a given frequency is not available for higher frequencies. Taking equations 6.11 and 6.14 we can calculate the energy that any ion has in the solar wind frame of reference. If we reconsider equation 3.37 on page 21 we can compare this energy as a mean energy with the observed temperatures. We have used the results of our standard analysis (s. section 4.6) and SWEPAM results for protons to calculate the heating rates $T/T_{H^{1+}}$ and compared them with the observations. In figure 6.11 the rates of the model and the observations for fast and slow solar wind are plotted versus the ratio q/m . γ and c of the model have been adjusted by eye. The main criteria for this adjustment have been the positions of He^{2+} and O^{6+} , because their temperatures should be most reliable due to their high abundance. In both cases a spectral index $\gamma = 1.05$ has been found. The parameter c that gives the scale of the wave is $c_{\text{fast}} = 3.18$, and $c_{\text{slow}} = 2.52$ respectively. v_{sw} , v_{Alf} and B needed for equation 6.8 have been chosen to the mean values of the observations, while P_0 for equation 6.14 has been chosen arbitrarily because we are only interested in ratios. Because of the energy drain by different ion species it is of some importance that the most abundant charge states are taken into account. We have made our selection based on the mean charge states from *Wang et al.* [2008]. Though the model is based on many simplifications, the trend of the observed temperatures is well represented (s. figure 6.11). The relative positions of several ions in respect to each other are reproduced very well, while some others deviate in parts strongly. We do not claim that the model represents the actual situation to a high degree. But the fact that the trend and the relative positions are reproduced, strongly indicates that wave-particle interaction is responsible for the observed temperatures in the fast but also in the slow solar wind. The smaller scaling factor c for the slow wind indicates together with much lower absolute temperatures that in the slow wind altogether less wave power is present, in agreement with results from *Belcher and Davis Jr.* [1971]. The ubiquitous lower temperature ratios in the slow wind might also be an indicator that the slower wind that has a longer travel time out to 1 AU has already started to thermalise via Coulomb collisions while the fast wind has not yet. However from our studies we can not decide whether the above stated is true or not but the fingerprints of wave-particle interaction heating the solar wind are clearly visible. We have also looked for a dependency on the direction of the magnetic field β (s. previous section) but no significant trends have been found.

6 Differential Streaming and Temperature

By calculating the heating rates also the wave power spectrum including the energy drain of the ions is derived. Figure 6.12 shows power spectra observed by Helios (upper panel) and a power spectrum we get from our model (lower panel). The observations show that at some point a spectral break occurs. *Markovskii et al.* [2008] found that the frequency of the spectral break is correlated with the proton gyro frequency. From our model we achieve a similar behaviour. From the point where He^{2+} is in resonance wave power significantly decreases to become zero at the resonance of H^{1+} . As mentioned before the model is not realistic at all and we do not claim that the observed spectral break is solely caused by an energy drain of the ions. But there is strong indication that the effect of wave-particle interaction can't be neglected if dealing with solar wind turbulence.

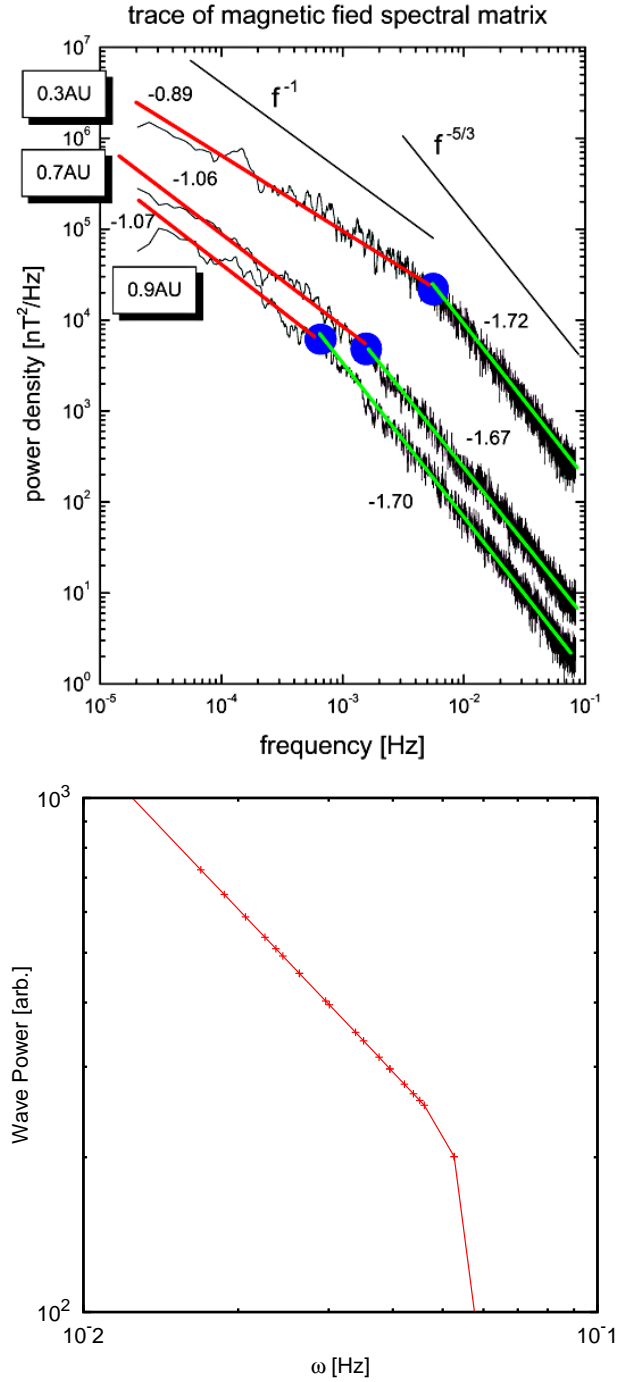


Figure 6.12: upper panel : Power density spectra of magnetic field fluctuations observed by Helios 2 between 0.3 and 1 AU within the trailing edge of the same corotating stream, during the first mission to the Sun in 1976, are shown. The spectral break (blue dot) shown by each spectrum, moves to lower and lower frequency as the heliocentric distance increases. From <http://solarphysics.livingreviews.org/Articles/lrsp-2005-4/>
lower panel : Wave power spectrum calculated from our model. The general trend of the observations is reproduced by the model. However, no direct comparison can be made.

7 Summary and Conclusions

In this thesis the kinetic properties of heavy solar wind ions have been investigated using PHA data from SWICS/ACE. Because heavy ions in general are rare and existing analysis techniques have disadvantages dealing with low count rates, a new maximum-likelihood analysis technique has been developed. The instrumental response functions that are essential for any kind of data analysis have been re-determined analysing long-term data together with an advanced efficiency model. The usage of long-term data also assures that there are no instrumental drifts in time. The results of our technique have been compared with the state-of-the-art analysis technique applied at the University of Michigan and the maximum likelihood technique has been found to be better adapted to low count situations. Additionally, there is strong evidence that the new re-determined instrumental response functions are in better agreement with the true instrumental response.

Up to now observations of heavy ions have been solely 1D. The interpretation of these 1D spectra that are projections of the 3D distributions is a challenging task. To explain the non-thermal features that are ubiquitous in the observations, a model for the 3D VDFs of heavy ions has been developed which is based on 3D observations of protons and alpha particles. The model consists of a core and a beam component that are separated by a drift velocity aligned with the direction of the magnetic field. Both components are represented by bi-Maxwellians that allow the simulation of expected anisotropies of the temperatures perpendicular, and parallel to the magnetic field. Also different intensities of core and beam can be simulated. Additionally a virtual detector simulating SWICS has been developed. The virtual detector has been built simulating many instrumental specific properties up to a very high degree, e.g. entrance angle dependent efficiencies. A lot of simplifications that are normally done for the standard data analysis have been abandoned and replaced by the best we know about the instrument. The instrumental orientation in respect to the magnetic field and to Sun-Earth line is also taken into account. The 3D model VDFs were analysed with the virtual detector and the results were compared with the observations.

For our studies we have selected periods of quiet time solar wind in the first half of 2007. The data has been analysed in 12 minutes and 1 hour resolution using our maximum likelihood analysis. Though all kinds of solar wind were present in our sample we restricted our analysis to the fast solar wind, because the non thermal features are most pronounced there. We found that the model is capable to reproduce the observed non thermal features. The differential streaming of heavy ions in respect to protons depends on the magnetic field direction, as is predicted by our model as a consequence of different beam intensities. We have shown that the observed trend flattens if the direction of the magnetic field varies too strongly within the time resolution of the data. Thus it is a requirement for a reasonable analysis of the kinetic properties to use data from time frames of more or less constant magnetic field direction. For SWICS this is normally only the case for 12 minute data.

Finally, we used a simple model for turbulent heating via ion cyclotron resonant wave-particle interaction to derive ion temperatures. The trend of the calculated temperatures is in good agreement with the observation of slow and fast solar wind. The obtained spectral index of the wave power spectrum is in good agreement with observations. Also the observed spectral break that is correlated with the gyro frequency of protons is reproduced by the model. Despite the simple character of the model the obtained results are in good agreement with observations of wave power spectra and ion heating rates. Thus, the results strongly indicate that wave-particle interaction is responsible for the heating of the ions in both solar wind regimes.

7.1 Outlook

Due to the high computing times of our maximum-likelihood analysis the data sample used for our studies has been small. The restriction to times of small variations in the magnetic field direction additionally reduced the sample. Therefore further studies based on a larger empirical basis have to be done. Though, the cores of the observed 1D spectra can be reproduced to a high degree the outer flanks are still poorly reproduced. Because wave-particle interaction tends to produce kappa distributions *Collier* [1993], we will try to replace the bi-Maxwellians of our model by corresponding kappa distributions. Due to their smooth slopes they might be able to reproduce the slopes of the distributions to a higher degree.

The maximum-likelihood analysis presented in this thesis in principal can be applied to other instruments. It is planned to apply the method to data from STEREO/PLASTIC.

7 Summary and Conclusions

PLASTIC provides the opportunity to obtain 3D spectra of heavy ions.

As we have stated the model we have used for our studies of wave-particle interaction is very simple. Crucial mechanisms like pitch angle scattering have been neglected. We will continue our studies and set up a more sophisticated model, that might bring further insights.

Finally, we will investigate suprathermal particles. The advantage of the presented maximum-likelihood analysis dealing with low count rates has been pointed out. Additionally the virtual spectra can be used to determine the onset of the suprathermal tails.

Bibliography

- Araneda, J. A., E. Marsch, and A. F. Viñas, Proton core heating and beam formation via parametrically unstable alfvén-cyclotron waves, *PRL*, 100(12), doi: 10.1103/PhyRevLett.100.125003, 2008.
- Belcher, J. W., and L. Davis Jr., Large-amplitude Alfvén waves in the interplanetary medium, 2., *JGR*, 76(16), 3534–3563, 1971.
- Collier, M. R., On generating kappa-like distribution functions using velocity space lévy flights, *GRL*, 20(15), 1531–1534, 1993.
- Gloeckler, G., et al., Investigation of the composition of solar and interstellar matter using solar wind and pickup ion measurements with SWICS and SWIMS on the ACE spacecraft, *Space Science Reviews*, 86(1-4), 497–539, doi:10.1023/A:1005036131689, 1998.
- Gold, R. E., S. M. Krimigis, S. E. Hawkins, D. K. Haggerty, D. A. Lohr, E. Fiore, T. P. Armstrong, G. Holland, and L. J. Lanzerotti, Electron, Proton, and Alpha Mointor on the Advanced Composition Explorer spacecraft, *Space Science Reviews*, 86(1-4), 541–562, doi:10.1023/A:1005088115759, 1998.
- Heuer, M., and E. Marsch, Diffusion plateaus in the velocity distributions of fast solar wind protons, *Journal of Geophysical Research*, 112, doi:10.1029/2006JA01979, 2007.
- Hollweg, J. V., Driver of the solar wind: then and now, *Philosophical Transactions of The Royal Society A*, 364(1839), 505–527, doi:10.1098/rsta.2005.1713, 2006.
- Klarmann, J., J. J. Beatty, W. R. Bins, P. Dowkontt, J. W. Epstein, and P. L. Hink, The ace-cris scintillating optical fiber trajectory (soft) detector, *International Cosmic Ray Conference*, 3(24), 673, 1995.
- Köten, M., Work in progress, Ph.D. thesis, Christian Albrechts Universität, Kiel, 2008.
- Markovskii, S. A., J. Vasquez, and C. W. Smith, Statistical analysis of the high-frequency spectral break of the solar wind turbulence at 1 au, *ApJ*, 675(2), 1576–1583, 2008.

Bibliography

- Marsch, E., K.-H. Mühlhäuser, H. Rosenbauer, R. Schwenn, and F. M. Neubauer, Solar wind helium ions: Observations of the helios solar probes between 0.3 and 1 au, *Journal of Geophysical Research*, 87(A1), 35–51, 1982a.
- Marsch, E., R. Schwenn, H. Rosenbauer, K.-H. Mühlhäuser, W. Pilipp, and F. M. Neubauer, Solar wind protons - three-dimensional velocity distributions and derived plasma parameters measured between 0.3 and 1 au, *Journal of Geophysical Research*, 87, 52–72, 1982b.
- Mason, G. M., et al., The ultra-low-energy isotope spectrometer (uleis) for the ace space-craft, *Space Science Review*, 86(1-4), 409–448, doi:10.1023/A:1005079930780, 1998.
- McComas, D. J., S. J. Bame, P. Barker, W. C. Feldman, J. L. Phillips, P. Riley, and J. W. Griffee, Solar Wind Electron Proton Alpha Monitor (SWEPAM) for the Advanced Composition Explorer, *Space Science Reviews*, 86(1-4), 563–612, doi: 10.1023/A:1005040232597, 1998.
- Möbius, E., et al., The solar energetic particle ionic charge analyzer (sepica) and the processing unit (s3dpu) for swics; swims and sepica, *SSR*, 86(1-4), 449–495, doi: 10.1023/A:1005084014850, 1998.
- Press, W. H., S. A. Teukolsky, W. T. Vetterling, and B. P. Flannery, *Numerical Recipes in C - The Art of Scientific Computing*, second ed., Cambridge University Press, 1992.
- Smith, C. W., J. L'Heureux, N. F. Ness, M. H. Acuña, L. F. Burlaga, and J. Scheifele, The ACE Magnetic Fields Experiment, *Space Science Reviews*, 86(1-4), 613–632, doi: 10.1023/A:1005092216668, 1998.
- Stone, E. C., A. M. Frandsen, R. A. Mewaldt, E. R. Christian, D. Margolies, J. F. Ormes, and F. Snow, The Advanced Composition Explorer, *SSR*, 86(1), 1–22, 1998a.
- Stone, E. C., et al., The solar isotope spectrometer for the advanced composition explorer, *SSR*, 86(1-4), 357–408, doi:10.1023/A:1005027929871, 1998b.
- Tsurutani, B. T., and G. S. Lakhina, Some basic concepts of wave-particle interactions in collisionless plasmas, *Rev. Geophys.*, 35(4), 491–501, 1997.
- von Steiger, R., N. A. Schwadron, L. A. Fisk, J. Geiss, G. Gloeckler, S. Hefti, B. Wilken, R. F. Wimmer-Schweingruber, and T. H. Zurbuchen, Composition of quasi-stationary solar wind flows from Ulysses/Solar Wind Ion Composition Spectrometer, *JGR*, 105(A12), 27,217–27,238, 2000.

Bibliography

Wang, X., B. Klecker, and P. Wurz, Effects of solar magnetic activity on the charge states of minor ions of solar wind, *ApJ*, 678(2), L145–L148, 2008.

List of Acronyms

ACE	Advanced Composition Explorer
ADC	Analog Digital Converter
CRIS	Cosmic Ray Isotope Spectrometer
DoY	Day of Year
EM	Efficiency Model
EPAM	Electron, Proton and Alpha Monitor
FM	Forward Model
IRF	Instrumental Response Function
MAG	Magnetometer
MF	Magnetic Field coordinates
MLE	Maximum Likelihood Estimator
MLF	Maximum Likelihood Fitting
PHA	Pulse Height Analysis
SC	Space Craft coordinates
SEE	Solar Centric Earth Ecliptic coordinates
SEPICA	Solar Energetic Particle Ionic Charge Analyser
SIS	Solar Isotope Spectrometer
SSD	Solid State Detector
STEREO	Solar TERrestrial RElations Observatory
SVD	Singular Value Decomposition

List of Acronyms

SWEPAM	Solar Wind Electron Proton Alpha Monitor
SWICS	Solar Wind Ion Composition Spectrometer
SWIMS	Solar Wind Ion Mass Spectrometer
ToF	Time of Flight
ULEIS	Ultra Low Energy Isotope Spectrometer

Danksagung

Herrn Prof. Dr. R. F. Wimmer-Schweingruber danke ich für die Vergabe des Themas und die stets gute Betreuung dieser Arbeit.

Für die zahllosen wissenschaftlichen und nichtwissenschaftlichen Diskussionen während der letzten vier Jahre möchte ich Herrn Dipl.-Phys. R. Rodde, Herrn Dipl.-Phys. M. Köten, Herrn Dipl.-Phys. B. Ehresmann und Herrn Dipl.-Phys O. Kortmann danken. Letzterem gilt mein ganz besonderer Dank, da ohne seine tatkräftige Hilfe bei zahllosen Problemen rund um den Computer, diese Arbeit sicherlich niemals fertig geworden wäre.

Den übrigen Mitarbeitern der Arbeitsgruppe “Extraterrestrik” möchte ich für das allgemein sehr positive Arbeitsklima danken.

Der Deutschen Forschungsgemeinschaft die diese Arbeit im Rahmen des Projektes WI2139/2 gefördert hat

Meiner Frau, Susanne Garbrecht und meiner Tochter, Liv Margaretha, deren Nerven ich sicherlich über die Gebühr beansprucht habe, gilt mein Dank ganz besonders. Auch für die Geduld die sie bewiesen haben, wenn Papa mal wieder länger in der Uni bleiben musste.

Lebenslauf

Name:	Lars Berger	
Wohnort:	Franckestraße 15, 24118 Kiel	
Geboren:	15.10.1977 in Kiel	
Familienstand:	verheiratet, eine Tochter	
Staatsangehörigkeit:	Deutsch	
Schulbildung :	1984 - 1988 1988 - 1997	Grundschule in Flintbek Humboldtschule in Kiel mit Abschluss der allgemeinen Hochschulreife Prüfungsfächer: Mathematik, Physik, Geschichte und Englisch
Wehrdienst :	1997 - 1998	Wehrdienst bei der Luftwaffe
Studium :	1998 - 2004	Studium der Physik an der Christian-Albrechts Universität zu Kiel, Diplomnote : mit Auszeichnung Diplomarbeit mit dem Titel “Bestimmung der Rotationsgeschwindigkeit Weißer Zwerge anhand der Verbreiterung der CaII-K Linie”, Betreuer: Prof. Dr. D. Koester
Berufstätigkeit :	Seit November 2004 12.08.-12.10.2007	Wissenschaftlicher Mitarbeiter der Arbeitsgruppe Wimmer am Institut für Experimentelle und Angewandte Physik der Christian-Albrechts Universität zu Kiel Elternzeit

Eidesstattliche Versicherung

Hiermit versichere ich an Eides Statt, dass ich die vorliegende Arbeit abgesehen vom Rat meiner akademischen Lehrer ohne fremde Hilfe und lediglich unter der Verwendung der angegebenen Literatur sowie den bekannten Nachschlagewerken der Naturwissenschaften angefertigt habe, und sie nach Inhalt und Form meine eigene ist. Diese Arbeit ist unter Einhaltung der Regeln guter wissenschaftlicher Praxis entstanden.

Des weiteren versichere ich, dass diese Arbeit weder ganz noch teilweise an anderer Stelle zur Prüfung vorlag. Frühere Promotionsversuche wurden von mir nicht vorgenommen.

Kiel, den

Lars Berger